Atmospheric Heat Transport: Variability, Trends, and the Role of Orography

Tyler Cox

A dissertation
submitted in partial fulfillment of the
requirements for the degree of

Doctor of Philosophy

University of Washington

2023

Reading Committee:
Kyle Armour, Chair
Gerard Roe, Chair
Aaron Donohoe

Program Authorized to Offer Degree:
Atmospheric Sciences

University of Washington

Abstract

Atmospheric Heat Transport: Variability, Trends, and the Role of Orography

Tyler Cox

Co-Chairs of the Supervisory Committee:
Associate Professor Kyle Armour
School of Oceanography and Department of Atmospheric Sciences

Professor Gerard Roe
Department of Earth and Space Sciences

Atmospheric heat transport (AHT) plays a key role role in Earth's climate. It helps moderate the equator to pole temperature gradient and is instrumental in Earth's hydrologic cycle. Despite this importance, there are numerous outstanding questions about AHT including what sets its magnitude in today's climate, its variability over time, and its recent and future trends under global warming. In this dissertation I first show that total AHT is relatively invariant to the addition of large mid-latitude orography due to strong compensation between different components of AHT. I then analyze the temporal variability of AHT. I find that zonally-integrated AHT distributions are nearly Gaussian, with a limited role for extreme events. Lastly, I look at trends in AHT since 1980. I find a strengthening of climatological AHT in the Southern Ocean and less clear hemispheric-scale signals in the Northern Hemisphere. Issues with reanalysis precipitation in the tropics creates unreasonable tropical AHT trends in atmospheric reanalysis datasets, with climate models doing a better job of accurately simulating the last 40 years of AHT changes. A principle of compensation emerges in all chapters of this work, where individual AHT components often vary in opposite-signed ways, such that total AHT varies less than individual AHT components.

TABLE OF CONTENTS

LIST OF FIGURES

Figure Number Page

LIST OF TABLES

Chapter 1

INTRODUCTION

Poleward atmospheric heat transport (AHT) is a critical element of the climate system. AHT moves energy from the equator, where it is warm and there is a surplus of energy, to the poles where it is cold and there is a deficit of energy. By transporting heat in this manner, AHT works to moderate the equator-to-pole temperature gradient, greatly expanding the habitable latitudes of Earth. Additionally, AHT is closely connected to the hydrologic cycle (e.g., Pierrehumbert (2010); Held and Soden (2006); Siler et al. (2018)) through its transport of moisture. In this way, AHT into or out of a region is often closely connected to how wet or arid a region is. Changes in AHT can cause hydrologic shifts, which in some cases can be hugely impactful for society (e.g., Burls et al., 2019). In light of the important role AHT plays in our climate, this dissertation works to improve our understanding of several aspects of AHT.

In this dissertation, AHT is referring to the meridional transport of heat in the atmosphere. A useful starting point is to consider why AHT exists in the first place. The most straightforward way to understand AHT is through diagnosing the amount of radiation coming into and out of the climate system at each latitude. Figure 1.1a shows the zonally-averaged incoming (shortwave) and outgoing (longwave) radiation. This radiation distribution creates a surplus of energy in the tropics and a deficit towards the poles. To balance this, energy (heat) must be transported from the equator towards the poles. This transport can take place in both the ocean and the atmosphere. Figure 1.1b shows that outside of the deep tropics, most of this heat is transported in the atmosphere.

While the explanation of AHT focusing on radiative surpluses and deficits is straightforward, it is also misleadingly simple. The amount of radiation entering or leaving Earth's climate is not independent of the amount of AHT (Cox et al., 2021). An increase in AHT could flatten the equator to pole temperature gradient, which would alter the distribution of outgoing longwave radiation.

AHT can also impact the incoming or outgoing radiation through cloud or albedo changes. Thus, a *radiative* perspective can provide us with a useful framework for diagnosing the magnitude of AHT, but it fails to provide a prediction for the magnitude of AHT.

A second way to understand AHT is through a *dynamic* perspective. In this perspective AHT is typically separated into three dynamical components (e.g., Holton and Hakim (2013)). We provide a more thorough mathematical breakdown of these components in each subsequent chapter, but briefly introduce them here. The three dynamic components of AHT are: the mean-meridional circulation AHT (MMC) calculated from zonal-mean fields; the stationary eddy AHT (SE) calculated from time mean and zonal-anomaly fields; and the transient eddy AHT (TE) calculated from time and zonal-anomaly fields. Each of these components can be connected to known dynamical features within Earth's atmosphere: the MMC is made up of the Hadley, Ferrel, and Polar cells; the SE is made up of stationary meanders in the storm track and monsoonal features; and the TE is made up of synoptic-scale storm systems. In this perspective, AHT can be thought of as the amount of heat transported poleward by movement of air parcels in the atmosphere. This perspective is useful in its close connections to observable atmospheric dynamics, but is not able to explain the overarching structure of total AHT.

A third way to understand AHT is through a *diffusive* perspective. In this perspective, the atmosphere is working to move moist-static energy (MSE, the sum of sensible, latent, and geopotential energy and defined more thoroughly in later chapters) down-gradient. The atmosphere has more MSE near the equator than the poles, and thus moves MSE down-gradient towards the poles. While this perspective does offer an intuitive reason for why AHT acts the way it does, the efficiency of the AHT (typically called the diffusivity (e.g., Armour et al., 2019)) is a free parameter that must be specified. As a result, the diffusive perspective does not by itself offer a prognostic prediction of AHT magnitude.

Altogether, each of these perspectives on AHT offer a different way to understand AHT. While a succinct answer for what sets the magnitude of total AHT or why AHT varies so smoothly with latitude (Fig. 1.1b and Trenberth and Stepaniak, 2003a) are beyond the scope of this dissertation, we do examine several aspects of AHT, which yield useful insights that may be able to guide future work in trying to determine what sets the magnitude of total AHT.

This work aims to address the following questions:

- Chapter 2: How does orography impact AHT?

  We use an idealized general circulation model (GCM) to examine the role that large mid-latitude mountains have on AHT. Given the discrepancy in substantial mountain ranges between hemispheres in our current geography (more mountains in the Northern Hemisphere) and strong evidence of large orographic features in the recent past (large ice sheets during the Last Glacial Maximum) it is important to try and accurately establish the role that orography has on total AHT and its components. We use each of the three perspectives on AHT highlighted and focus holistically on the AHT system, rather than focusing on individual pieces separately. This allows us to see that AHT is relatively invariant to the addition of orography.

- Chapter 3: How does AHT vary in time?

  We use the latest state-of-the-art high-resolution atmospheric reanalysis (ERA5, Hersbach et al., 2018a) to investigate how AHT varies on 6-hourly time scales. This type of work is increasingly possible to do as reanalysis datasets improve to have higher temporal and spatial resolution. Establishing how AHT varies in time is valuable given the important role that AHT plays in Earth's energy budget and hydrologic cycle. If individual extreme events are important for AHT, then this may have ramifications for the study of AHT-related fields like hydrology. We find that extreme events are not exceptionally important for zonally-integrated AHT, giving us confidence that focusing on mean AHT, rather than individual AHT events, is warranted.

- Chapter 4: How was AHT changed since 1980?

  We use climate models and reanalysis datasets to investigate how AHT has changed since 1980. Past work has predicted that AHT is projected to increase with global warming. We examine if these predictions are evident in reanalysis datasets and evaluate how well the most up-to-date climate models predict the observed changes. We find a strengthening of climatological AHT in the Southern Ocean that is generally captured by all models and reanalysis. In the tropics reanalysis datasets predict unreasonable AHT trends. The Northern Hemisphere AHT trends are generally smaller, with less agreement between models and reanalysis.

A common theme that emerges throughout these chapters is AHT compensation, in which total AHT often changes, or varies in time, with smaller magnitude than the individual AHT components across a range of time scales (from 6-hourly to multi-decadal trends). This occurs because the AHT components are changing or varying in compensatory ways (i.e., with opposite signs). One clear consequence of this is that focusing on only one AHT component can make it difficult to understand how AHT as a whole is changing. Additionally, previous work has pointed out that AHT varies remarkably smoothly with latitude (Trenberth and Stepaniak, 2003b). A strong tendency towards compensation helps prevent total AHT from varying too far from this smoothly varying state, as any change in one AHT component is at least partially compensated by a change in another component. If compensatory principles are strong enough it likely becomes difficult for AHT to change much at all (Donohoe et al., 2020). We revisit this idea of compensation, and its implications, in Chapter 5.

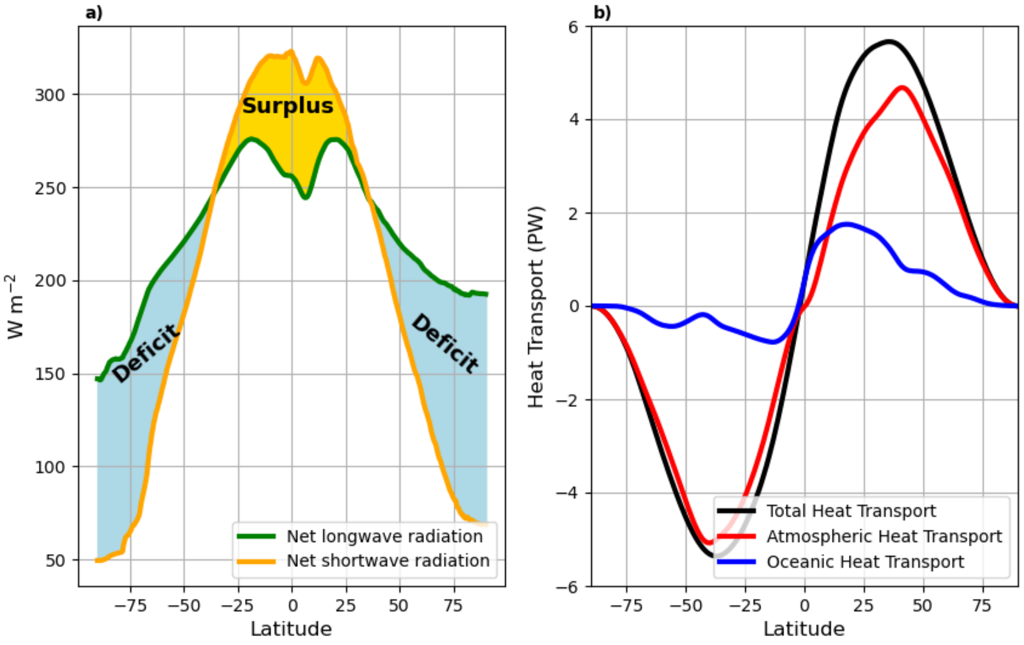

Figure 1.1: a) Zonal-mean net top-of-atmosphere longwave and shortwave radiation. b) Meridional atmospheric heat transport (red line), ocean heat transport (blue line), and total heat transport (black line). Radiation data is from CERES (NASA/LARC/SD/ASDC, 2019) and heat transport data is from Donohoe et al. (2020).

Chapter 2

NEAR INVARIANCE OF POLEWARD ATMOSPHERIC HEAT TRANSPORT IN RESPONSE TO MID-LATITUDE OROGRAPHY

This work was published as Cox, T., A. Donohoe, G. H. Roe, K. C. Armour, and D. M. Frierson, 2022: Near invariance of poleward atmospheric heat transport in response to midlatitude orography. Journal of Climate, 35 (13), 4099–4113, https://doi.org/10.1175/JCLI-D-21-0888.1. Cox et al. (2022)

2.1 *Introduction*

Poleward atmospheric heat transport (AHT) is a critical element of the climate system, moderating the equator-to-pole temperature gradient and carrying the water vapor of the hydrologic cycle (e.g., Pierrehumbert, 2010, Held and Soden, 2006, Siler et al., 2018). The observed annual-mean total AHT is similar between hemispheres (Figs. 2.1a,e), despite there being more land and more substantial mountain ranges in the Northern Hemisphere. The distribution of mountains and land create stationary Rossby waves, which enhance zonal asymmetries in temperature and precipitation and contribute to AHT (e.g., Manabe and Terpstra, 1974, Hoskins and Karoly, 1981, Broccoli and Manabe, 1992, Held et al., 2002).

It is useful to deconstruct AHT into three dynamical components (e.g., Holton and Hakim, 2013). We deconstruct and define AHT as

$$\mathrm{AHT}(\phi) = \frac{2\pi a\ cos(\phi)}{g} \int_0^{P_s} \underbrace{\left[\overline{\mathrm{V}}\right]\left[\overline{\mathrm{MSE}}\right]}_{\mathrm{MMC}} + \underbrace{[\mathrm{V}^*\ \mathrm{MSE}^*]}_{\mathrm{SE}} + \underbrace{\overline{\left[\mathrm{V}^{*\prime}\ \mathrm{MSE}^{*\prime}\right]} + \overline{[\mathrm{V}]^\prime\,[\mathrm{MSE}]^\prime}}_{\mathrm{TE}}\ dp, \tag{2.1}$$

where the integral is over pressure, p, from the top-of-atmosphere (TOA) to the surface, square brackets [] denote zonal averages, overbars $\overline{()}$ denote time averages, asterisks (*) are departures from the zonal average, and primes ($'$) are departures from the time average. ϕ is latitude, V is the meridional velocity, and MSE is the moist static energy, defined as

$$\mathrm{MSE} = c_p T + L_v q + gZ, \tag{2.2}$$

where c_p is the specific heat of air, T is the atmospheric temperature, L_v is the latent heat of vaporization of water, q is the specific humidity, g is the acceleration of gravity, and Z is the geopotential height.

The first term in Eqn. 2.1 is the component due to the mean meridional circulation (MMC), which is calculated from the time-mean and zonal-mean fields. We account for conservation of mass by removing the vertically averaged MSE (Marshall et al., 2014, Donohoe et al., 2020). The second term is the stationary-eddy (SE) component, which is calculated from the time-mean zonal anomalies. The third and fourth terms are collectively called the transient-eddy (TE) component, although we note that the fourth term is much smaller than the third (Marshall et al., 2014).

The contrasting land and mountain distributions between Northern and Southern hemispheres give rise to differences in these dynamic components. Specifically, the AHT carried by SEs is much larger in the mid-latitudes of the Northern Hemisphere than at equivalent latitudes of the Southern Hemisphere (Figs. 2.1c,e). The difference in poleward AHT by SEs between the Northern Hemisphere and Southern Hemisphere at each latitude peaks at 1.1 PW (Fig. 2.1e). In contrast, the hemispheric difference in total AHT (solid lines, Figs. 2.1a,e) is relatively smaller, peaking at only 0.6 PW. That is, the hemispheric asymmetry in SE AHT is compensated by hemispheric asymmetries in the AHT associated with the MMC and TEs. Moreover, the total AHT varies smoothly with latitude with a shape that is similar between hemispheres, despite both the strong latitudinal structure and the hemispheric asymmetries of the individual dynamic components (Trenberth and Stepaniak, 2003b). For these reasons, we refer to total AHT as relatively invariant between the Northern and Southern Hemispheres. We note the hemispheric asymmetry of total heat transport by the ocean and atmosphere combined is smaller than that in AHT alone (Donohoe et al., 2020), but we will focus exclusively on AHT in this chapter.

Perhaps even more striking is that both the hemispheric symmetry and the smoothness of total AHT seen in the modern climate persist in general circulation model (GCM) simulations of the Last Glacial Maximum (LGM). Although large Northern Hemisphere ice sheets disrupt the circulation patterns in the mid-to-high latitudes of the Northern Hemisphere, creating additional SE AHT (e.g., Cook and Held, 1988, Donohoe et al., 2020), total AHT remains relatively invariant (Figs. 2.1b,f) due to compensating decreases in TE AHT (Li and Battisti, 2008). These examples motivate the primary question this work addresses: how is total AHT so nearly invariant and smoothly-varying with latitude in response to mid-latitude orography even while SE AHT changes so substantially? Although land distribution, ocean heat transport, and orography impact AHT, this work will focus on the effect of orography.

Previous research has characterized AHT through three different perspectives (e.g., Armour et al., 2019). The first perspective characterizes AHT through the atmosphere's dynamic motions, as defined in Eqn. 2.1. Total AHT is dominated by the MMC and SEs in the tropics and then gradually becomes dominated by eddies poleward of 25° latitude (Fig. 2.1c). This perspective on AHT will be referred to as the *dynamic* perspective. Although the dynamic perspective is necessary in order to characterize how atmospheric circulations supply the observed AHT, it has not traditionally offered an obvious way to understand why total AHT is invariant and smoothly varying with latitude (e.g., Armour et al., 2019).

A second perspective is that AHT can be characterized through the energetic requirements implied by the TOA radiation and surface energy budgets. The imbalance between incoming and outgoing radiation must be balanced by meridional heat transport within the earth system (e.g., Stone, 1978). This meridional transport can be accomplished by both the atmosphere and the ocean, but we focus on the atmospheric part in this work, in part because it dominates outside of the deep tropics (e.g., Farneti and Vallis, 2013). From this perspective, the smoothness of AHT with latitude is mandated by the smoothness of net TOA radiation (Trenberth and Stepaniak, 2003b). Moreover, AHT changes must be accompanied by changes in net TOA radiation (absent changes in ocean heat transport). However, due to the coupling between radiation and circulation, it can be difficult to determine which, if either, is more fundamental in driving AHT changes (Cox et al., 2021). We refer to this perspective on AHT as the *energetic* perspective.

A third perspective on AHT comes from the Earth's tendency to move energy down-gradient. Previous work has shown that a general principle of down-gradient diffusion of near-surface MSE accurately captures AHT and its changes (Flannery, 1984, Hwang et al., 2011, Roe et al., 2015, Bonan et al., 2018, Merlis and Henry, 2018, Siler et al., 2018, Armour et al., 2019). From this perspective, AHT is smoothly varying because the MSE gradient varies smoothly with latitude. Theory suggests that TEs in the mid-latitudes efficiently mix MSE (Held, 1999), supporting the idea that a diffusive perspective may work in the mid-latitudes. Recent research has shown down-gradient transport works surprisingly well at all latitudes, even those not dominated by TE AHT (Armour et al., 2019). This down-gradient diffusion principle is referred to as the *diffusive* perspective.

Previous work about AHT invariance involves compensation between the atmospheric circulations that contribute to AHT. This work does not try to present a comprehensive summary of all mechanisms responsible for AHT invariance, but highlights those we find most important in our work. From the dynamic perspective, orography induces a stationary atmospheric circulation with associated SE AHT anomalies (e.g., Manabe and Terpstra, 1974, Broccoli and Manabe, 1992, Held et al., 2002). These changes in SE AHT are often accompanied by opposite-signed changes in TE AHT, such that total AHT changes by a smaller magnitude than the SE AHT changes alone (Manabe and Terpstra, 1974, Kaspi and Schneider, 2013). This SE and TE compensation principle has theoretical justification, as SEs can modify the baroclincity that TEs rely on while TEs and the heating associated with them can help drive SEs (e.g., Branstator, 1995, Chang et al., 2002, Held et al., 2002, Inatsu et al., 2003, Kaspi and Schneider, 2013), and has been found to be important in current and past climates (Donohoe et al., 2020). Additional dynamic connections exist between eddy AHT convergence and Ferrel cell AHT (e.g., Sasamori and Melgarejo, 1978, Salustri and Stone, 1983), and eddy momentum fluxes and Hadley Cell strength (e.g., Walker and Schneider, 2006).

From the energetic perspective, AHT will remain relatively invariant if orography does not induce substantial changes in TOA or surface energy fluxes. However, orography can change both shortwave and longwave radiation fluxes through its effects on cloud cover and temperature patterns.

Kiehl (1994) found that compensation often occurs between cloud shortwave and longwave radiation effects in the tropics. In general, cloud longwave and shortwave effects do not cancel out. This is indicated by the substantial inter-model spread of mean state cloud radiative effects, which lead to inter-model differences in AHT of order 20 percent (Donohoe and Battisti, 2012).

From the diffusive perspective, anomalies created by the addition of orography will be smoothed through down-gradient energy transport. Specifically, the anomalous SE AHT associated with orography will (in the absence of other changes) reduce the equator-to-pole MSE gradient thereby reducing the diffusive AHT by TEs. The extent to which these SE AHT anomalies are smoothed, and the extent to which total AHT remains invariant, are dependent on the size of the anomalies and the diffusivity of the atmosphere.

This work explores the ways in which AHT compensation occurs, from each of these three AHT perspectives, and the extent to which total AHT can remain invariant with the addition of mid-latitude orography. To do so, we study the AHT response to the addition of idealized mountain ridges to the mid-latitudes of each hemisphere in two aquaplanet atmospheric GCMs. This idealized modeling setup (explained in more detail in Section 2.2) allows us to study the mechanisms of AHT changes without the full complexity found in comprehensive GCMs or nature. We then test the sensitivity of our results, and reintroduce some complexity, by adding a seasonal cycle.

2.2 *Model Setup*

One mechanism that might contribute to AHT invariance is compensation between changes in absorbed shortwave radiation (ASR) and outgoing longwave radiation (OLR). Therefore we use two models of different radiative complexity. The first model is a gray radiation model with no clouds or water-vapor feedback; temperature anomalies are radiatively damped only by the Planck response. The specific model we use is GRaM from Frierson et al. (2006) adapted to use the convection scheme from Frierson (2007). Shortwave radiation is not absorbed in the atmosphere, and longwave radiation is absorbed and emitted per a prescribed optical depth. The insolation in GRaM is adjusted to mimic the effect of clouds and surface albedo in order to give a more realistic value for total AHT (see Frierson et al. (2006) for full details). The second model we use is the Geophysical Fluid Dynamics Laboratory's AM2 (GFDL Global Atmospheric Model Development Team, 2004), which has a more complex radiation scheme including atmospheric shortwave absorption, and cloud and water-vapor feedbacks. Both models are initially run as aquaplanets at perpetual equinox conditions with no land or sea ice and a shallow mixed layer depth of 2.4 m to enable rapid model spin up. AM2 simulations are run for 20 years, with the last 18 years used for analysis, while GRaM simulations are run for 10 years, with the last 8 used for analysis. The shorter simulation time in GRaM is sufficient to capture an accurate climatology due to its simpler radiation scheme than AM2. Climatological AHT is realistic in both models (Figs. 2.2a,b), but is higher than observations due to the absence of ocean heat transport.

Using these two models, we test the impact of large-scale mountain ranges (referred to here as ridges), similar in style to those used by Wills and Schneider (2016). These lozenge-shaped ridges are described by the formula:

$$z(\lambda, \phi) = h_0 \, exp \left[\frac{(\lambda - \lambda_0)^2}{2{\sigma_\lambda}^2} - \frac{max(0, |\phi - \phi_0| - R)^2}{2{\sigma_\phi}^2} \right], \tag{2.3}$$

where λ is the longitude in degrees, ϕ is the latitude in degrees, h_0 = 4000 m, ϕ_0 = 40°, R=4° , σ_λ=12.5°, and σ_ϕ=8°. When more than one ridge is included, λ_0 is chosen such that the ridges are equally spaced in each hemisphere. Meridional cross-sections of these ridges are plateaus, with flat sections of meridional extent $2R$, bounded by Gaussian-shaped slopes, while longitudinal cross sections are Gaussian in shape. The surface type remains a mixed-layer slab of water throughout, so these mountains can be described as ”water ridges”.

The size, shape, and location of orographic features all affect the SE response, and therefore may affect the degree of AHT compensation. We perform simulations with one, two, or three mountain ridges in each of the Northern and Southern Hemispheres (mirrored symmetrically across the equator) located between 20° and 60°. Different numbers of mountain ridges generally create different magnitudes of SE AHT (dashed lines, Figs. 2.2c,d). Therefore, by adding in one, two, or three mountain ridges we can test how the magnitude of disruption affects the ability of the atmosphere to maintain nearly invariant total AHT. We also tested a variety of other orographic configurations including ridges of different heights and at different latitudes (not shown), as previous work has suggested that tropically-forced stationary waves may lead to changes in total AHT (Baggett and Lee, 2017, Park and Lee, 2019). We found that the specific mountain configuration, even the addition of tropical mountains, did not substantially affect our main findings regarding the near-invariance of AHT in response to orography.

2.3 *Results*

Figure 2.2 summarizes the main results of our simulations from GRaM (left-hand panels) and AM2 (right-hand panels). The total AHT and its dynamic components are shown for the control (no ridges), and for the one-, two-, and three-ridge cases in the top panels. The anomalies from the control case are shown in the lower panels. Results are presented for only one hemisphere, as the hemispheres are symmetric by design. For all experiments, the addition of orography introduces substantial SE AHT (dashed lines), but there is a larger impact in GRaM than in AM2. For the 3-ridge case in GRAM, SEs contribute a maximum of about 3 PW to total AHT (Fig. 2.2c) near 30° latitude.

Despite the large SE AHT induced by the orography, total AHT remains nearly invariant in both GRaM and AM2 (solid lines in Figs. 2.2c,d). Total AHT changes never exceed 0.5 PW, and are under 0.25 PW at most latitudes. That is, substantial changes in individual AHT dynamic components are compensated such that total AHT changes by less than any of the individual dynamic components. This compensation between AHT dynamic components is further explored in Section 2.3.1. The changes in total AHT are smaller in GRaM than in AM2, suggesting compensation is better in GRaM. In both models, compensation of SE AHT changes occurs through changes in both TE and MMC AHT, with the relative importance of each depending on latitude and model.

Total AHT changes are smaller in our simulations compared to previous work that introduced SEs intro GCMs. Manabe and Terpstra (1974) split the total AHT into dry and moist components. They found little change in the poleward moist AHT and relatively large changes in poleward dry AHT after the introduction of orography, while this work finds little change in both dry and moist AHT in the mid-latitudes (not shown). This may be due in part to the fixed surface temperatures used in Manabe and Terpstra (1974). Using a modeling setup similar to GRaM, Kaspi and Schneider (2013) also found larger changes in total AHT when they induced SEs through the use of zonal-anomalies in surface heating. This suggests that the degree of AHT compensation may be influenced by the method of inducing SEs.

We first characterize the effects that the mountains have on atmospheric circulations, and then evaluate how the AHT compensation occurs through the dynamic, energetic, and diffusive perspectives. In order to reduce the results presented to a manageable amount, we will focus on the two-ridge case. The main aspects of the circulation response do not depend on the number of ridges, although in the three-ridge case there is some interference between the responses to individual ridges. We will describe the circulation changes from a Northern Hemisphere perspective (although the hemispheres are symmetric).

In general, the circulation response of the atmosphere is similar to that seen in other modeling simulations that introduce idealized orography (e.g., Manabe and Terpstra, 1974, Broccoli and Manabe, 1992, Held et al., 2002). We focus here on elements of the atmospheric response that are most relevant to AHT or differ from previous work.

The circulation of the lower troposphere is strongly disrupted by the addition of the orography as is seen in the climatological stream functions at 700 hPa in Figs. 2.3a,e (streamfunctions calculated using windspharm Python package, Dawson (2016)). The main circulation response can be characterized as flow splitting ahead of the orography: streamlines impinging on the southwestern side of the ridges bow southwards, and streamlines impinging on the northwestern side bow polewards. The flow splitting upwind of the ridges is also evident in the quadrupole structure of the meridional wind anomalies (Figs. 2.3b,f). Flow can also be deflected over the top of the mountains, but the ridges' size and latitudinal position make flow splitting more favorable (e.g., Trenberth and Chen, 1988, Ringler and Cook, 1997, Rodwell and Hoskins, 1996). In fact, the low-level westerly flow impinging on the southwest portion of the mountains is so strongly deflected that it turns back to join the easterly trade winds (Figs. 2.3a,e). This is likely because the equatorward-dipping isentropes make it particularly hard for the flow to move over the southern end of the mountains (e.g., Valdes and Hoskins, 1991, Takahashi and Battisti, 2007a, Brayshaw et al., 2009), and so helps build the anticyclonic flow that is evident in the streamfunctions between the ridges in subtropical latitudes. To the lee of each ridge there is convergence where the flow enters the region of locally enhanced streamfunction gradients (Figs. 2.3a,e). This results in a storm track that begins in the lee of the topography and tracks into the northeastward-tilting region of stronger flow, although the specific patterns and amplitudes differ between the models. This storm-track response has been seen in previous work (e.g., Hoskins and Valdes, 1990, Brayshaw et al., 2009, Cash et al., 2005, Inatsu et al., 2002), and is reminiscent of the Atlantic and Pacific storm tracks in the lee of the Rockies and Tibetan plateau, respectively.

The flow splitting ahead of the orography induces anomalous meridional winds, which generally bring associated anomalies in temperature via advection of the mean-state meridional temperature gradients. In regions of anomalous southerly flow on the northwest and southeast sides of the mountains, warm-air advection causes positive temperature anomalies, while in regions of anomalous northerly flow on the northeast and southwest sides of the mountains, cold-air advection causes negative temperature anomalies (Figs. 2.3d,h). Cloud changes in AM2 also modify the magnitude of the temperature anomalies, particularly to the northeast of each mountain. The combination of wind anomalies (Figs. 2.3b,f) and temperature anomalies (Figs. 2.3d,h) gives rise to anomalous SE AHT, which will be further explored in section 2.3.1.

The orography creates some dramatic impacts on the precipitation patterns (Figs. 2.3c,g). Strikingly, neither model displays the classic west-to-east orographic rain shadow that might be expected for westerly impinging flow. Instead, there is drying to the west, and particularly the southwest, of the mountains. This drying is due to subsidence from both the divergence of the zonal wind, as the flow is divided into northern and southern routes around the mountains, and the equatorward velocity anomaly (Fig. 2.3b,f), which is balanced by subsidence to maintain Sverdrup balance (Rodwell and Hoskins, 2001, Takahashi and Battisti, 2007b). This drying is also seen, albeit to a weaker and smaller spatial extent, in Brayshaw et al. (2009). Enhanced precipitation occurs on the eastern side of the mountains where the diverted flow converges and poleward velocity anomalies induce rising motion. Maps of anomalous vertical velocity (not shown) appear similar to those of precipitation. There is no substantial upward vertical velocity on the western side of the mountains suggesting that most of the flow is deflected around the mountains rather than over them. A more typical, albeit weak, west-to-east orographic rain shadow does occur in our simulations with smaller (h_0 = 2500 m) ridges where westerly flow is more able to move over rather than around the ridges (not shown).

2.3.1 Dynamic Perspective on AHT Response to Orography

In this section we evaluate the impact of the orography on AHT from a dynamical perspective. There are large changes in the individual dynamic components of AHT (Figs. 2.2c,d): up to 3 PW in GRaM and 2 PW in AM2 even though, as already noted, changes in total AHT are less than 0.25 PW at most latitudes. How do the individual dynamical components adjust to achieve this overall near-invariance of total AHT?

In most of our simulations, the AHT associated with the SEs induced by the orography forms a two-peaked structure with peaks at approximately 25° and 55°, and a local minimum near the center of the prescribed orography at 40°. The equatorward peak in SE AHT is generally larger than the poleward peak, although the magnitude of each peak is dependent on the model and number of ridges (dashed lines in Figs. 2.2c,d). In GRaM, SE AHT increases with the number of ridges for both the 25° and 55° peaks, albeit nonlinearly; while in AM2, SE AHT increases at the peak at 25° but decreases for the peak at 55°, which nearly disappears for the 3-ridge case. This decrease in AM2 is due to weaker fluxes of temperature and moisture around the northern side of each ridge (not shown).

The adjustment of the other two dynamic components of AHT to the introduction of orography differs between the two models. The TE AHT decreases at most latitudes in both models (dotted lines in Figs. 2.2c,d). However, in GRaM the pattern of TE AHT decrease closely matches the double peaked pattern of SE AHT increases, but with the opposite sign; whereas in AM2 the pattern of TE AHT decrease has one peak at about 35° latitude. The patterns of the changes in MMC AHT are similar in both models (dots in Figs. 2.2c,d), although the magnitude of the changes is larger in AM2. There is a decrease in MMC AHT in the subtropics and an increase in mid-latitudes; and a negative anomaly of MMC AHT in the high latitudes in AM2, but not in

GRaM. Overall, from Figure 2.2 we see that, in GRaM, the primary compensation occurs between the SE and TE transports; while in AM2 it is a 3-way balance, with compensation from the MMC being particularly important in the subtropics.

Changes to individual dynamic components of AHT do not happen in isolation from one another. As mentioned previously, there are established mechanisms for how the dynamic components interact, and those mechanisms tend to produce compensation. Kaspi and Schneider (2013) show how SEs modify the baroclinicity by altering moist-static energy gradients. At latitudes where ridges drive SE AHT, the zonal-mean MSE gradient is decreased, reducing the TE AHT that relies on these gradients. Moreover, the Ferrel Cell is partially driven by changes in the convergence of AHT by both SEs and TEs (e.g., Sasamori and Melgarejo, 1978, Salustri and Stone, 1983) such that increases to eddy AHT convergence will strengthen the Ferrel Cell. The climatological Ferrel Cell AHT is equatorward, so a strengthened Ferrel Cell transports more heat equatorward, compensating for the increased AHT convergence by the eddies. Decreased eddy AHT convergence has the opposite effect, resulting in a weakened Ferrel Cell, and less equatorward AHT to compensate for decreased AHT convergence by the eddies. A final major connection between dynamic components is the influence that eddy momentum fluxes have on Hadley Cell strength (e.g., Walker and Schneider, 2006). Increases in eddy momentum flux divergence in the Hadley Cell region strengthen the Hadley Cell, while the opposite is also true. In this way, changes to extratropical circulation can influence tropical circulation patterns. A hallmark of all these mechanisms is that they tend to be compensatory: a change in one dynamic component is typically mitigated by an opposite-signed change in another dynamic component. Together, they create an interacting system of dynamic components that, in aggregate, resist changes in total AHT.

We can better understand some features of the dynamic AHT components in our simulations, and see some of the compensatory mechanisms at work, by looking at plan-view maps. We again show just the two-ridge case and describe features from a Northern Hemisphere perspective. The left-hand panels of Figure 2.4 show maps of the vertically-integrated local anomalies of SE and TE AHT. These values are calculated identically to the zonal-mean values, except zonal-integration is not performed, and are referred to as local AHT. The cause of the double-peaked zonal-mean SE

AHT structure is clearest in GRaM (Fig. 2.4a), where poleward local AHT is evident at the four corners of each mountain, with the smallest local SE AHT anomaly in the NW quadrant. This four-corner pattern is caused by the westerly flow splitting ahead of the mountains and causing anomalous northerly flow to advect warmer, moister air, while anomalous southerly flow advects colder, dryer air, as was previously described in Section 2.3. Similar features can be discerned in AM2 (Fig. 2.4d), although the pattern is less defined, and strung out more around a latitude belt. The local TE anomalies are harder to make sense of: there is a tendency for reduced local TE AHT upwind of the ridges and increased local TE AHT in the lee of the ridge (consistent with the inferred storm tracks from Fig. 2.3), but it is hard to discern the zonal-mean structure, or the differences between models. There is no clear anti-phase local relationship between SE and TE AHT changes suggesting that compensation between the two AHT components occurs nonlocally.

To better understand how nonlocal compensation between SE and TE AHT occurs, we look at plan-view plots of near-surface MSE gradient anomalies and local TE AHT anomalies (Figs. 2.4b,e). Changes to near-surface MSE gradients are created by zonally anomalous meridional winds (SE winds) advecting the mean-state temperatures (Figs. 2.3b,f,d,h). In GRAM the picture is particularly clear. In the lee of each ridge, there is a region of stronger MSE gradients, caused by circulations connected to SEs to the north and south advecting cold and warm air, respectively, which enhances the MSE gradient between these regions (colors, Figs. 2.4b,e). Local TE AHT is enhanced in this region due to the increased MSE gradient. However, in the zonal mean, MSE gradients are weakened at latitudes centered on 25°N and 55°N; and associated with this is a reduction in zonal mean TE AHT. In general this shows how SEs can influence the MSE gradient that is important for TE AHT. This alteration is one mechanism for how non-local compensation between TE and SE AHT can occur. This picture is more difficult to discern in AM2, in part because the MMC is also an important piece of the compensation. This idea of connections between zonal mean TE AHT and zonal mean MSE gradients is explored further in Section 2.3.3. We note that changes in local TE AHT are better explained by local MSE gradient changes than by local eddy kinetic energy changes (not shown).

We further investigated compensation between the MMC AHT and eddy AHT in both the

Hadley and Ferrel Cells. Eddy AHT convergence in the mid-latitudes is proportional to the strength of both the mass and heat transport of the Ferrel Cell (not shown). Eddy momentum fluxes in the tropics and subtropics scale with the strength of both the mass and heat transport of the Hadley cell (not shown). The Hadley Cell undergoes larger changes in AM2 than in GRaM (dots in Fig. 2.2d vs 2.2c), and the eddy momentum fluxes also weaken more in AM2. Changes in the Hadley Cell are also influenced by the climatology of the two models, as AM2 has a particularly narrow region of tropical convection, while GRaM has a broader area of tropical convection. Both the connections between eddies and the Ferrel Cell and eddies and the Hadley Cell are compensatory with stronger eddies reducing the polewards AHT of the MMC.

The local details of plan-view plots and the magnitude of SE AHT differ between simulations and models, but the general principle of AHT compensation and total AHT invariance is found throughout. The dynamic perspective is useful for understanding how atmospheric circulation changes affect AHT, and provides intuition for how these circulation changes give rise to compensation between different AHT components. However, the dynamic perspective does not provide much insight into the degree of compensation. In the next section, we turn to the energetic perspective to provide a more quantitative understanding of why AHT is so nearly invariant.

2.3.2 Energetic Perspective on AHT Response to Orography

An alternative way to think about AHT is through the energetic requirements implied by the TOA zonal-mean radiation budget. The differences between incoming and outgoing radiation must be balanced by meridional AHT as there is no ocean heat transport (and thus no net surface heat flux) in our model setups. Figure 2.5 shows the zonal-mean anomalies in TOA radiation caused by the orography for the one- two- and three-ridge cases, and for both models. We define downwards radiation as positive, and upwards radiation as negative, so the climatological ASR is positive and OLR is negative. It is important to note that AHT can alter temperature and cloud-cover patterns, which in turn can alter net TOA radiation. Therefore, ASR and OLR changes do not unidirectionally cause AHT changes, but they do provide useful information to help understand why total AHT is invariant in our simulations.

In GRaM, ASR is constant by construction, so only changes in OLR can contribute to changes in net TOA radiation. Moreover, due to the gray-radiation scheme, changes in OLR arise only from surface and atmospheric-temperature anomalies. As the number of ridges increases in GRaM, the pattern of net TOA radiation anomalies remains similar, but the amplitude increases (Fig. 2.5, top panels). Within the tropics, anomalies in net TOA radiation are generally less than 3 W m^{-2}. These anomalies are small compared to the overall climatological surplus of net TOA radiation (ASR minus OLR) within the tropics of 41 W m^{-2} in GRaM, and so the anomalies in maximum poleward AHT (i.e., the integral of the tropical net TOA radiation anomalies) are also small. From this perspective, introducing the orography in GRaM has not changed tropical temperatures enough to substantially affect tropical OLR. Therefore, while orography can cause a repartitioning of AHT among its dynamic components, total AHT must be nearly invariant. In the mid- and high-latitudes, changes of OLR in GRaM are consistent with the zonal-mean cooling in the latitude band where the ridges lie, and the zonal-mean warming poleward of them (Fig. 2.3d). Again, the mid- and high-latitude radiation changes are small compared to the climatological deficit of net TOA radiation outside the tropics of -65 W m^{-2} in GRaM, so total AHT is relatively invariant.

The inclusion of clouds in AM2 means that both OLR and ASR can and do change by large amounts (Figs. 2.5d-f). Changes in zonal-mean net TOA radiation anomalies approach 10 W m^{-2} in the two-ridge case (with even larger values seen in the three-ridge case). However, there is a strong spatial variability, with generally small net TOA radiation changes in the tropics as a whole (tropical-average values range from 0.1 W m^{-2} in the three-ridge case to 3.1 W m^{-2} in the two-ridge case). Therefore, like the results for GRaM, these changes are small compared to the climatological tropical surplus of net TOA radiation of 39 W m^{-2} in AM2, and so changes in AHT are also correspondingly small. In the mid- and high-latitudes, mean changes for both ASR and OLR in AM2 are also small compared to the climatological differences in ASR and OLR (the climatological deficit of net TOA radiation outside of the tropics is -68 W m^{-2} in AM2). There is more variation in the latitudinal structure of radiation anomalies in AM2 than in GRaM, likely due to the sensitivity of cloud changes to temperatures and the complex patterns of interference between the responses to individual ridges.

To further explore changes of both ASR and OLR in AM2 we consider plan-view maps for the two-ridge case (Figs. 2.4c,f). OLR decreases over each ridge due to decreased surface-temperatures associated with the increased elevation of the ridges (Fig. 2.3h, colors). Away from each ridge, OLR changes (Fig. 2.4c, colors) are caused by high-cloud changes (Fig. 2.4c, contours). OLR decreases, and high clouds increase, in both the enhanced stormtrack downstream of each ridge, and equatorward of each ridge due to changes in precipitation and convection patterns. OLR increases to the SW of each ridge due to subsidence, and on the equator in regions between each ridge due to shifts in locations of deep convection. In general, the changes to high clouds and OLR also mirror the changes in precipitation patterns (Fig. 2.3g). ASR patterns are well-explained by changes to total clouds, with ASR decreasing in the previously mentioned areas of precipitation and deep convection changes, albeit with some additional tropical changes due to low cloud changes.

Changes to ASR and OLR in AM2 do not happen in isolation from each other, and compensation between the two helps keep TOA radiation anomalies small. ASR and OLR compensate particularly well near the equator where anomalies in ASR and OLR reach 15 W m^{-2}, but net TOA radiation anomalies are under 1 W m^{-2} (similar to that found in previous observational work of Kiehl (1994)). Similar compensation, where the anomalies in ASR or OLR are larger than the anomalies in net TOA radiation, can also be seen at other latitudes. However, this zonal-mean compensation does not occur locally in most regions (i.e. ASR and OLR anomalies are not typically collocated). The lack of local ASR and OLR compensation suggests that zonal circulations, such as the Walker Cell, are important for limiting zonal-mean net TOA radiation changes. The exception, where weak local compensation does occur, is in the region of enhanced storm activity downstream of each ridge, and equatorward of each ridge. A detailed exploration of the ways in which zonal-mean compensation between ASR and OLR occur, despite the lack of local compensation, is beyond the scope of this work, but could provide interesting avenues for future study.

The detailed patterns of ASR and OLR anomalies that emerge in AM2 are likely not universal. If these same experiments were repeated with different models, some parts of the patterns of radiative anomalies would likely change due to both different cloud responses and different parameterizations of cloud albedo. Even within AM2, the structure of the zonal-mean ASR and OLR changes differs depending on the number of ridges. However, the general principle of ASR and OLR compensation, and relative invariance of net TOA radiation, is more robust. Given these simulations and those of the LGM using comprehensive GCMs (Donohoe et al., 2020), it seems difficult to substantially alter zonal-mean ASR or OLR without altering both of them in compensatory ways, implying that total AHT is relatively invariant in response to orography.

Throughout all of these simulations there are only small changes in net TOA radiation, either because OLR changes are small (as in GRaM) and/or because ASR and OLR compensate each other (as in AM2). One possible reason why the changes in net TOA radiation are small in our simulations and past climates is that the atmosphere is efficient at smoothing temperature anomalies, causing zonal-mean radiation fields to exhibit small overall changes. This idea of smoothing anomalies can be explored through a diffusive perspective on AHT.

2.3.3 Diffusive Perspective on AHT Response to Orography

From the diffusive perspective, AHT can be characterized as down-gradient diffusion of MSE from the equator towards the poles, whose magnitude is set by both the meridional MSE-gradient and the atmospheric diffusivity. This perspective has been shown to be effective at explaining AHT and its changes in a range of climates (Flannery, 1984, Hwang et al., 2011, Roe et al., 2015, Bonan et al., 2018, Merlis and Henry, 2018, Siler et al., 2018, Armour et al., 2019). In this view, the smoothness of total AHT arises because atmospheric dynamics efficiently smooth out bumps or irregularities in MSE. Both dynamic and energetic perspectives are related to the diffusive perspective through the connection between TE AHT and MSE-gradients and the smoothly varying zonally-averaged TOA radiation climatologies, respectively.

We apply this down-gradient transport principle to see how well a diffusive approximation can recreate the AHT response of the GCMs. We use the same moist-energy-balance model (MEBM) as in previous work (Roe et al., 2015, Liu et al., 2017, Siler et al., 2018, Bonan et al., 2018, Armour et al., 2019)), and then make several alterations that are outlined below. In general, the MEBM allows us to test the how well both the TE AHT response and total AHT invariance can be explained through down-gradient diffusion. We perform an MEBM simulation for each of our mountainous simulations, three for GRaM and three for AM2. In each MEBM simulation we apply a ”forcing”, $R_f(x)$, that is equal to the divergence of SE and MMC AHT anomalies in response to mountains, as derived form each GCM simulation. In the MEBM, this forcing must be balanced by the combination of radiative feedbacks and down-gradient heat transport by TEs, with the balance between these two pieces determining how well the MEBM can compensate for the forcing anomalies and recreate the TE AHT response from the GCM. Mathematically this looks like:

$$\lambda\, T_s^{'}(x) \;+\; R_f(x) + \;=\; -\frac{p_s}{ga^2} D \frac{d}{dx}\left[(1-x^2)\frac{dh^{'}}{dx}\right], \tag{2.4}$$

where x is the sine of latitude, λ is the radiative feedback, $T_s^{'}$ is near-surface temperature anomaly, R_f is the forcing, p_s is the surface pressure, g is the acceleration due to gravity, a is the radius of earth, and D is the climatological diffusivity. $h^{'}$ is the near-surface MSE anomaly defined as:

$$h^{'}(x) = c_p\, T_s^{'}(x) + L_v\, q_s^{'}(x), \tag{2.5}$$

where c_p is the specific heat of air, L_v is the latent heat of vaporization, and $q_s^{'}$ is the near-surface specific humidity anomaly. The near-surface relative-humidity is assumed to be constant at 80 percent, so $h^{'}$ is a function of only $T_s^{'}$ and $\frac{p_s}{g}$ is approximated at 10^4 kg m^{-2}. We set λ = -1 W m^{-2} K^{-1} everywhere. We tested values for λ ranging from 0 to -2.5 W m^{-2} K^{-1}, and found that the specific value of feedback has some quantitative effects on the results, but that the general conclusions from this diffusive perspective are not dependent on the specific value chosen for λ. We diagnose values of the diffusivity for both GRaM and AM2 from their control GCM simulation, taking the same approach as Liu et al. (2017). We then spatially average the diffusivity values and use that single value in each of the respective MEBM simulations (1.3 x 10^6 m^2 s^{-1} for all GRaM simulations and 1.1 x 10^6 m^2 s^{-1} for all AM2 simulations).

First, the MEBM solves for the $T_s^{'}$ needed to balance the imposed ”forcing” subject to linear feedbacks and MSE diffusion. The MEBM’s prediction of the TE AHT anomaly ($TE^{'}$) can then be calculated by integrating the left-hand side of Equation 2.4:

$$TE' = 2\pi a^2 \int_{-1}^{x} \Big(\lambda\, T_s'(\hat{x}) + R_f(\hat{x}) \Big)\, d\hat{x}. \tag{2.6}$$

Note that this formulation does not account for the fact that changes in TE AHT will affect other dynamic AHT components in our climate system (Section 2.3.1). However, these calculations are a first-order approximation of how well down-gradient diffusion explains the TE AHT response and total AHT invariance in our GCM simulations. The total AHT anomaly in each MEBM simulation is the SE and MMC AHT anomalies that were used to force the MEBM, combined with the calculated MEBM TE AHT anomaly, TE'.

The design of these MEBM simulations guarantees that some degree of compensation will occur, as the diffusive, down-gradient nature of the MEBM will at least partially compensate the imposed forcing. The degree of compensation can be thought of as a ratio, where the numerator is the response of the system, in this case the absolute value of the TE AHT anomaly, and the denominator is the forcing on the system, in this case the absolute value of the sum of the anomalous SE and MMC AHT. A ratio of 1 would mean perfect compensation and no change in total AHT. A ratio of 0, would indicate no response by the TE AHT to the forcing and would require the forcing to be entirely balanced by the radiative response. Some intuition about the degree of compensation expected can be gained from the analytic solutions to a dry EBM, following, e.g., Held (1999). For a dry EBM, $\frac{dh}{dx}$ in Eqn. 2.4 is replaced with $\frac{dT}{dx}$, and a new D, D_{dry}, is chosen to match climatology. We calculate D_{dry} identically to how we calculate D, but use near-surface temperature and sensible AHT rather than near-surface MSE and total AHT, and find values of 4.2 x 10^6 m^2 s^{-1} for GRaM and 2.3 x 10^6 m^2 s^{-1} for AM2. Again, following Held (1999), we assume that scale of the forcing is governed by a second-oder Legendre polynomial. For such a system, the compensation ratio is

$$\frac{|TE'|}{|\int_{-1}^{x} (R_f)\, d\hat{x}|} = \frac{6\,\widetilde{D_{\text{dry}}}}{-\lambda + 6\,\widetilde{D_{\text{dry}}}}, \tag{2.7}$$

where $\widetilde{D_{\text{dry}}} = D_{\text{dry}} * (\frac{c_p * p_s}{a^2 g})$. The left-hand column in Table 2.1 shows that this dry theory would predict that a forcing coming from a 1 PW anomaly in SE and MMC AHT would generate a diffusive compensation of -0.86 PW TE AHT anomaly in GRaM and of -0.77 PW in AM2.

Table 2.1: The absolute value of the ratio of the TE AHT anomaly to the sum of the SE and MMC AHT anomalies for the two-mountain simulations. Results from the GCMs and MEBM are averaged from 20° to 60°.

	Dry theory	GCM Ratio	MEBM Ratio
AM2	0.77	0.72	0.72
GRaM	0.86	0.93	0.77

Figure 2.6 shows the comparison of TE AHT anomalies (top panels) and the total AHT anomalies (bottom panels) and Table 2.1 shows the compensation ratio for both the MEBM and GCMs. The top panels show how well the diffusive MEBM approximates the GCM response of the TE AHT to the orography. A perfectly diffusive response would require dashed and solid lines of the same color overlapping entirely. The bottom panels in Fig. 2.6 depict the degree of total AHT invariance in the MEBM (dashed lines) and GCMs (solid lines). Exact invariance would be zero AHT anomalies.

In both models, TE AHT changes from the GCM are well approximated with the MEBM. The magnitude of the TE AHT anomalies in the MEBM are less than those in the GCM at almost all latitudes, but total AHT is still relatively invariant in the MEBM. Table 2.1 shows the expected and actual compensation ratios for the two-mountain simulations, with values from the MEBM and GCMs averaged between 20° and 60° latitude. While the actual ratios are in the general range of the theoretical dry ratio, there are discrepancies. These discrepancies likely arise because the GCMs are not operating in a purely diffusive way, and that the GCMs and MEBM include moisture. In GRaM, the compensation is better in the GCM (ratio closer to 1) than in the MEBM, while the AM2 simulation shows similar compensation in both the GCM and MEBM. Despite the differences, both models exhibit compensation ratios close to the ratio from idealized dry theory. As a result, these calculations suggest that the TE part of the response can be understood as a largely diffusive response, and that carries with it a strong tendency towards AHT invariance.

2.3.4 Effect of Seasonality on AHT Compensation

We have shown that a high degree of AHT invariance exists even when substantial orography is introduced in two different GCMs. One way to evaluate the robustness of the result is to add a seasonal cycle to our AM2 experiments. Adding seasonality forces the AHT to adjust to both the previously added orography, and also to the large variations in the radiative gradients that drive AHT in the first place.

Seasonality is added by changing the obliquity from 0 to 23.439°. The mixed-layer depth is also increased from 2.4 to 12 m to yield a more Earth-like seasonal cycle of AHT (Donohoe et al., 2014). We only perform seasonal simulations in AM2, as the radiation in GRaM has been tuned to the annual mean. Figure 2.7 shows the annual-mean AHT and its dynamic components (Fig. 2.7a) and the AHT anomalies (Fig. 2.7b); these results should be compared to Figs. 2.2b,d.

Remarkably, the annual-mean AHT is even more invariant to the addition of mountains when the seasonal cycle is included (solid lines in Fig. 2.7b vs. solid lines in Fig. 2.2d). Even for the three-ridge case, anomalies in AHT never exceed 0.2 PW, and are mostly less than 0.1 PW. The mid-latitudes of the seasonal simulations have similar, but weakened, annual-mean circulation patterns to the perpetual-equinox simulations (not shown). The magnitude of the mid-latitude AHT anomalies for each of the dynamic components are roughly half that of the perpetual-equinox simulations (Fig. 2.7b vs Fig. 2.2d). The tropics have larger differences between seasonal and perpetual-equinox simulations. In the annual-mean, the anomalies in MMC AHT are much smaller in the seasonal simulations than in the perpetual-equinox simulations. However, this annual-mean picture obscures substantial monthly anomalies in MMC AHT. Figure 2.8 shows the anomalous total AHT and its dynamic components for each month for the two-ridge simulation (compare any given month in Fig. 2.8 to the annual-mean anomalies in Fig. 2.7b). In February, there is a nearly 2 PW positive total AHT anomaly just north of the equator in the seasonal two-ridge simulation, when compared to the seasonal control (no orography) simulation. This additional AHT represents a 55% increase in AHT over the February control climatology, and comes mostly from anomalous MMC AHT. Then, by June there is little total AHT anomaly near the equator, but come August there is a slightly over 1 PW negative total AHT anomaly. In these seasonal simulations, the tropical response is both time varying and substantially different from the perpetual equinox simulations. Despite these differences, both perpetual-equinox and seasonal simulations result in nearly invariant annual-mean total AHT in the tropics. These results suggest that including the seasonal cycle means that invariance is achieved with a different balance of compensating mechanisms, but that the tendency for invariance is, if anything, strengthened.

Within any single month, some degree of compensation can generally be identified among the dynamic components of the AHT, which can be seen where the different dynamic components have different signs in Figure 2.8. However, as mentioned earlier, the compensation within any given month is typically much worse than in the annual-mean, with monthly AHT anomalies reaching 2 PW, while annual-mean total AHT anomalies are under 0.25 PW (Figs. 2.7b and 2.8). Moreover, the combination of compensating dynamic components varies substantially in different months and latitudes. This requires that there is compensation occurring across time, and therefore that seasonal heat storage in the mixed layer is important in compensation between months. At annual time scales, the SE AHT divergence must be balanced by the sum of the radiative response and the TE and MMC AHT changes. However, on monthly time scales with a seasonal cycle, the SE AHT divergence can also be fluxed into the mixed-layer. Moreover, since the efficiency of energy exchange between the atmosphere and ocean is almost an order of magnitude greater than the radiative feedback (Barsugli and Battisti, 1998), we expect much less AHT compensation on monthly timescales. The heat that is added to, or removed from, the mixed-layer during one month is then used in AHT in later months, such that the annual mean shows excellent AHT compensation. When we analyzed the seasonal AM2 output fields, we were unable to draw any general lessons about the specific mechanisms of storage and dynamic compensation. The mechanisms appear complex and regionally variant; and, given the differences between AM2 and GRAM in the annual mean, they may well vary among models.

The strong AHT compensation in AM2 with a seasonal cycle points to the robustness of AHT invariance in response to mid-latitude orography. While the mechanisms of this compensation may change between seasons, between models, and between seasonal and perpetual-equinox simulations, the compensation in total AHT shows the fundamental flexibility of the atmospheric adjustment.

2.4 *Summary and Discussion*

Using idealized simulations with mid-latitude orography in two general circulation models we find little change in total AHT between our control and mountainous simulations, despite substantial changes in the partitioning of AHT between SEs, TEs and the MMC. This shows that there is AHT compensation occurring, where changes to the individual dynamic components offset one-another. Similar evidence for strong compensation is seen when comparing AHT differences between the Northern and Southern hemispheres in the modern climate, and when considering simulated AHT changes when LGM ice sheets are imposed. Additionally, total AHT remains smoothly varying, despite substantial latitudinal structure in the changes to individual dynamic components.

The invariance of total AHT is explored through three complementary perspectives. The dynamic perspective (Section 2.3.1) shows how changes to circulation and temperature patterns affect dynamic AHT components. Adding mid-latitude orography in our simulations creates substantial positive SE AHT anomalies, which are compensated by decreases in both TE and MMC AHT. The compensation between TE AHT and SE AHT dominates in GRaM, while compensation between all three dynamic AHT components plays a role in AM2. This dynamic compensation is similar to that seen between our current climate and the LGM (Donohoe et al., 2020).

The energetic perspective (Section 2.3.2) links AHT to the energy required by net TOA radiation. In our simulations without clouds (those using GRaM), the changes in net TOA radiation are entirely due to changes in OLR and are generally small at all latitudes. When a model with a more complex radiation scheme is used (AM2), the changes in net TOA radiation are once again small, even as ASR and OLR changes are larger. This is due to compensations between ASR and OLR as well as large spatial variability that becomes small when taking a spatial average, such that net zonal TOA radiation, and thus AHT, remain relatively invariant.

The diffusive perspective (Section 2.3.3) assumes that AHT arises due to the down-gradient transport of MSE. When the addition of orography is viewed through this perspective, the question becomes, how well can the atmosphere smooth MSE anomalies created by the addition of the orography? We use a MEBM to explore how well this diffusive perspective can explain the relatively invariant total AHT found in each GCM. We find that our MEBM simulations effectively smooth anomalies such that total AHT remains relatively invariant. The MEBM simulations also show that approximating the TE AHT as a diffusive response works well.

This work does not try to present a comprehensive list of all AHT compensation mechanisms, but instead aims to show the robustness of the principle of AHT compensation in a variety of idealized modeling setups. The addition of seasonality in our simulations provides a sensitivity test for the principle of AHT compensation in response to mid-latitude orography. The AHT compensation in the annual-mean of seasonal simulations is better than that in perpetual-equinox simulations, showing the impressive compensatory ability of the atmosphere.

On Earth, SEs are forced not only by orography, but also by land-sea contrasts and ocean heat transport. Work by Kaspi and Schneider (2013) suggest that total AHT may be less invariant if SEs are forced by zonal-anomalies in surface heating. While additional simulations that force SEs in a different manner are beyond the scope of this work, they would present an additional manner of testing the flexibility of Earth's AHT system.

Overall, this work points to Earth's AHT system as being robust and capable of compensating for changes in orography, such that total AHT is relatively invariant. Recent work that used a more complex GCM and probed a variety of SE magnitudes also found little change in total AHT (White et al., 2021). The robust degree of compensation seen in observations; in realistic simulations of the present and past; and in our idealized multi-model numerical experiments in this study, points to the possibility of an underlying dynamic or thermodynamic principle governing this behavior.

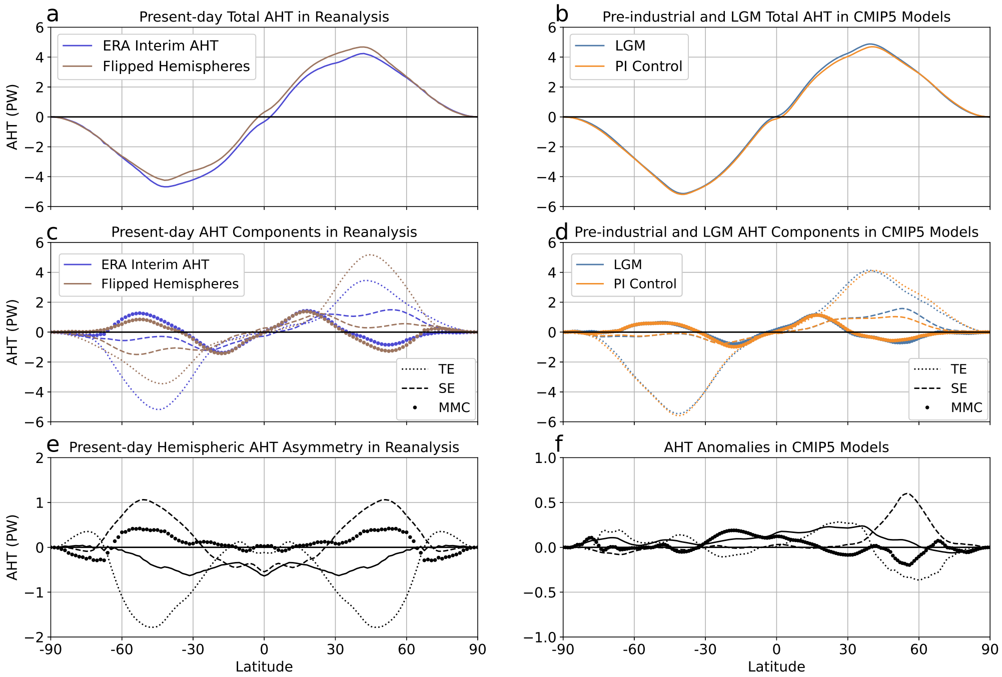

Figure 2.1: Total AHT a) and the dynamic AHT components c) for the climatological AHT from ERA-Interim (light purple) and the same values flipped across the equator (brown); total AHT b) and the dynamic AHT components d) for the climatological AHT from CMIP5 ensemble means for pre-industrial (black) and Last Glacial Maximum (blue) conditions; e) the anomalies, S. Hemisphere minus N. Hemisphere, in AHT between hemispheres from ERA Interim; and f) the anomalies, LGM minus PI control, in AHT between pre-industrial and the LGM from the CMIP5 ensemble (calculations from Donohoe et al. (2020)).

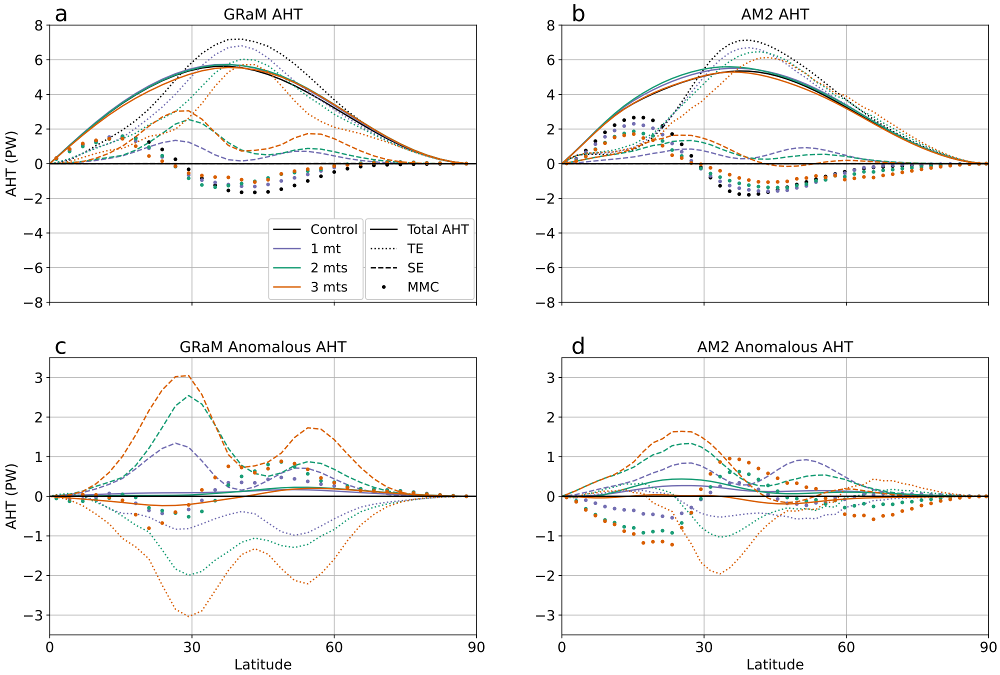

Figure 2.2: Total AHT and its dynamic components for a) GRaM and b) AM2 and the anomalous AHT for c) GRaM and d) AM2, where anomalies are calculated as mountain simulation minus control. Different colors denote ridge cases, and different line styles show the different dynamical components for each case. Results shown are the mean of the Northern and Southern Hemispheres (with the Southern Hemisphere sign flipped), which are symmetric by design.

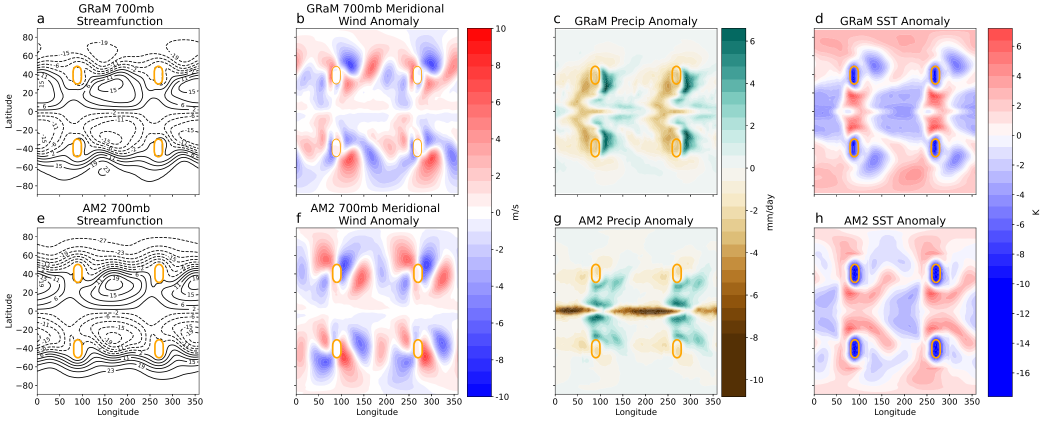

Figure 2.3: The top row shows results from GRaM and the bottom row shows results from AM2. a) and e) show 700 hPa streamfunctions with units of 10^6 m^2 s^{-1}; b) and f) show 700 hPa meridional wind anomalies; c) and g) show precipitation anomalies; and d) and h) show sea-surface temperature anomalies. Anomalies are calculated as two-mountain simulation minus control. Orange contours are the 700 hPa surface pressure contours to show the general position of the mountains.

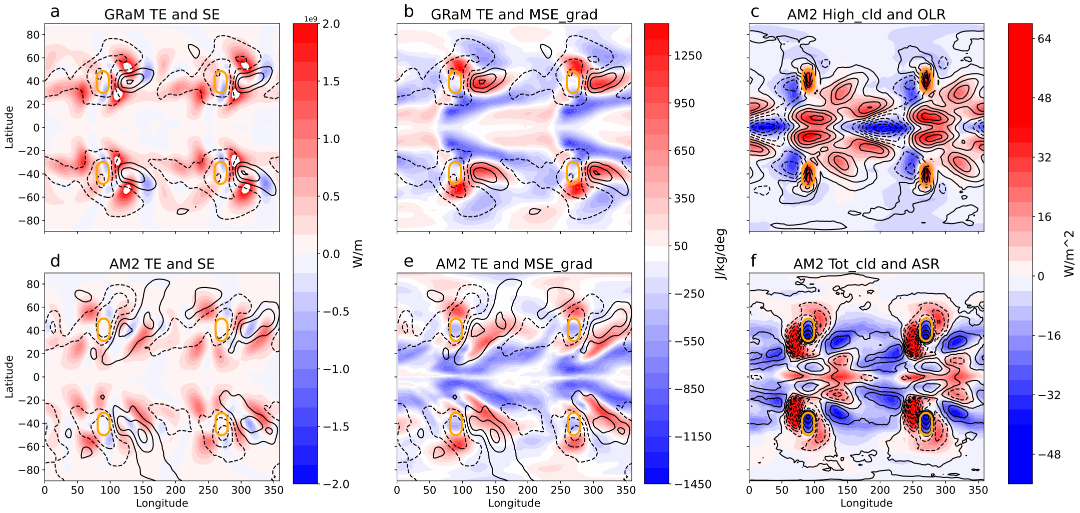

Figure 2.4: The two leftmost columns compare results from GRaM (top) and AM2 (bottom). a) and d) show anomalies in local SE AHT (colors) and local TE AHT (black contours, interval = 9x10^8 W m^{-1}); b) and e) show anomalies in near-surface MSE gradient (colors) and local TE AHT (black contours, interval = 9x10^8 W m^{-1}). The rightmost column shows cloud and radiation output fields from AM2. c) shows anomalies in OLR (colors) and high-cloud fraction (black contours, interval = 0.018); finally, f) shows anomalies in ASR (colors) and total cloud fraction (black contours, interval = 0.018). Anomalies are calculated as two-mountain simulation minus control. AHT is defined as positive poleward in both hemispheres and the climatological MSE gradient is defined as positive in both hemispheres. Orange contours are the 700 hPa surface pressure contours to show the general position of the mountains.

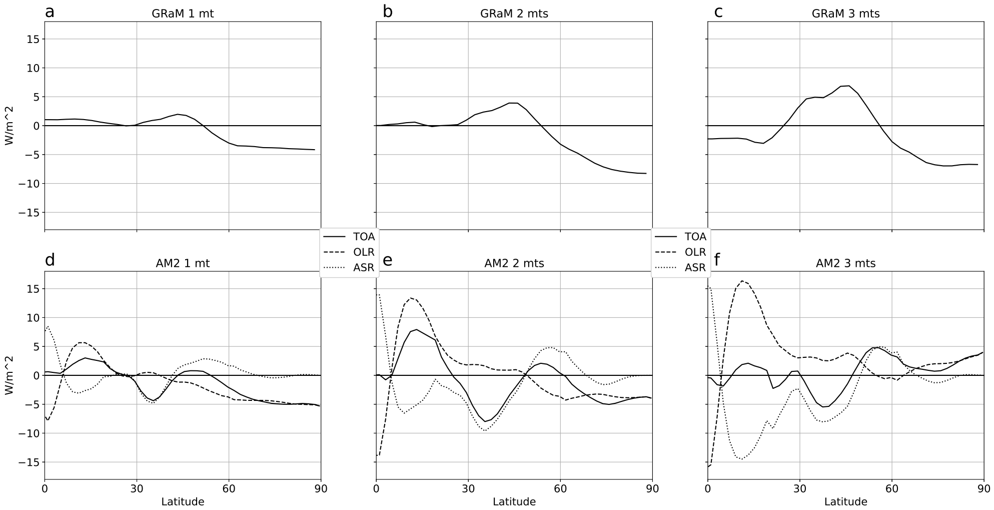

Figure 2.5: Anomalies in zonally-averaged net TOA radiation, ASR, and OLR for a-c) GRaM and d-f) AM2, where anomalies are calculated as mountain simulation minus control. Upwards radiation is defined as negative and downwards as positive. Results shown are the mean of the Northern and Southern Hemispheres, which are symmetric by design.

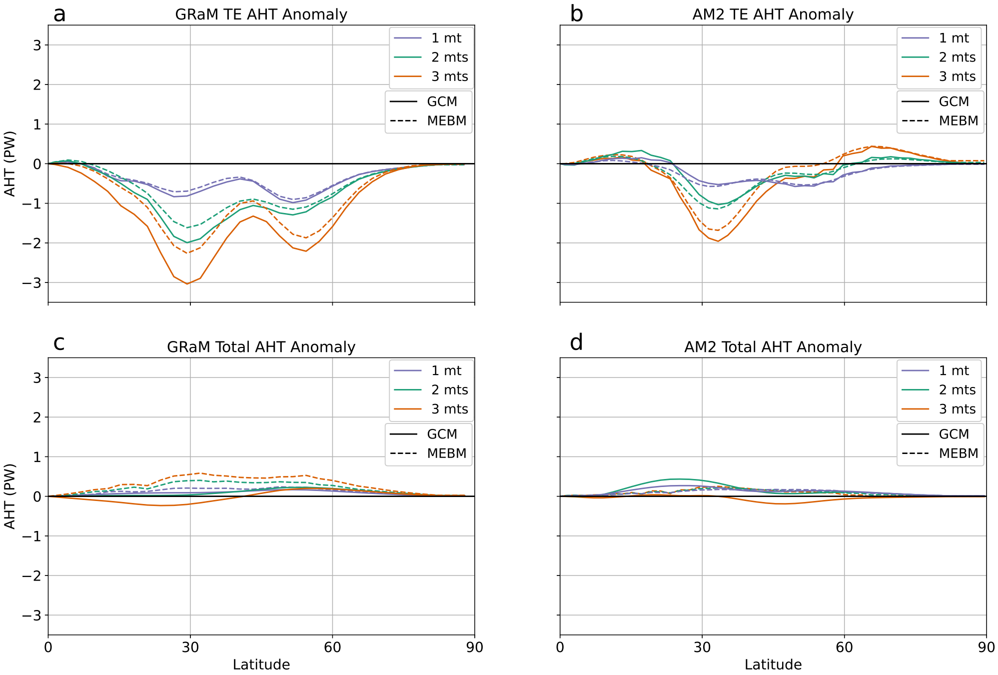

Figure 2.6: TE AHT anomalies from the GCM and the MEBM for a) GRaM and b) AM2 and total AHT anomalies for the GCM and MEBM for c) GRaM and d) AM2, where anomalies are calculated as mountain simulation minus control. Results shown are the mean of the Northern and Southern Hemispheres (with the Southern Hemisphere sign flipped), which are symmetric by design.

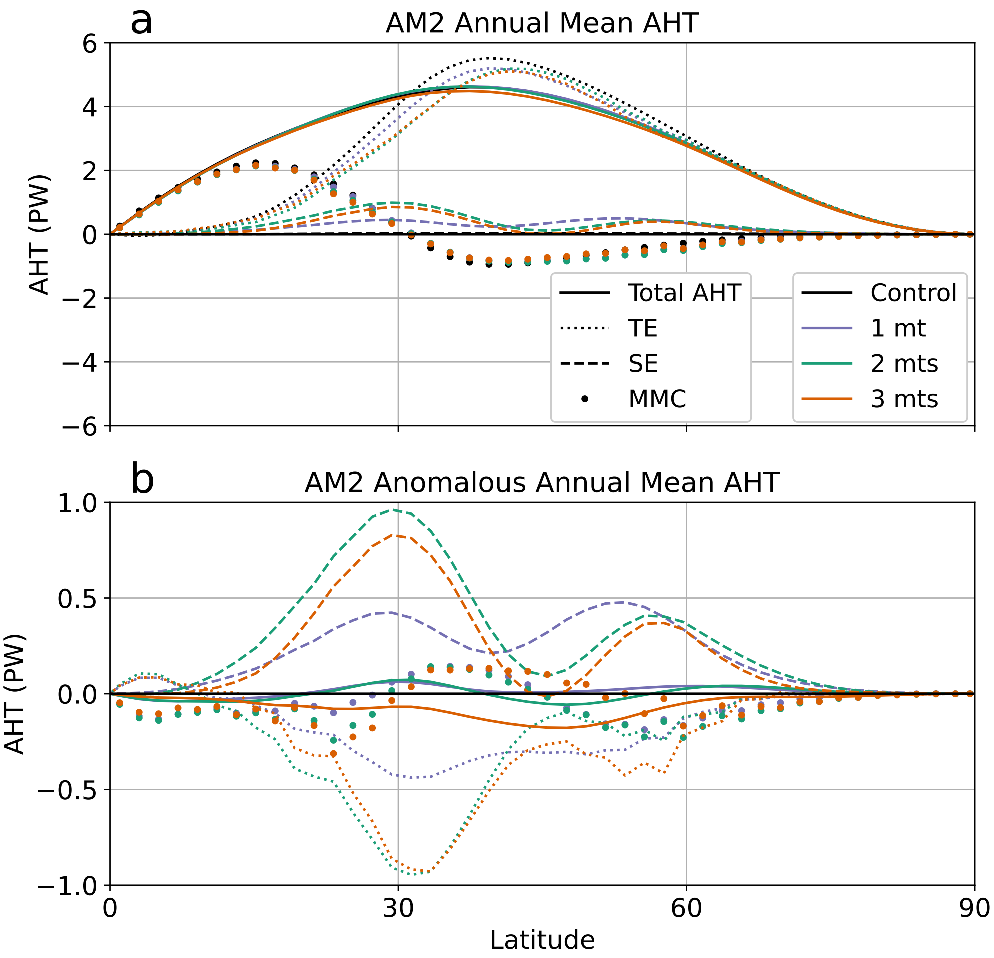

Figure 2.7: Total AHT and its dynamic components for a) the annual-mean of AM2 simulations with a seasonal cycle; and b) the anomalies in annual-mean AHT in the AM2 seasonal simulations, where anomalies are calculated as seasonal mountain simulation minus seasonal control. Results shown are the mean of the Northern and Southern Hemispheres (with the Southern Hemisphere sign flipped), which are symmetric by design.

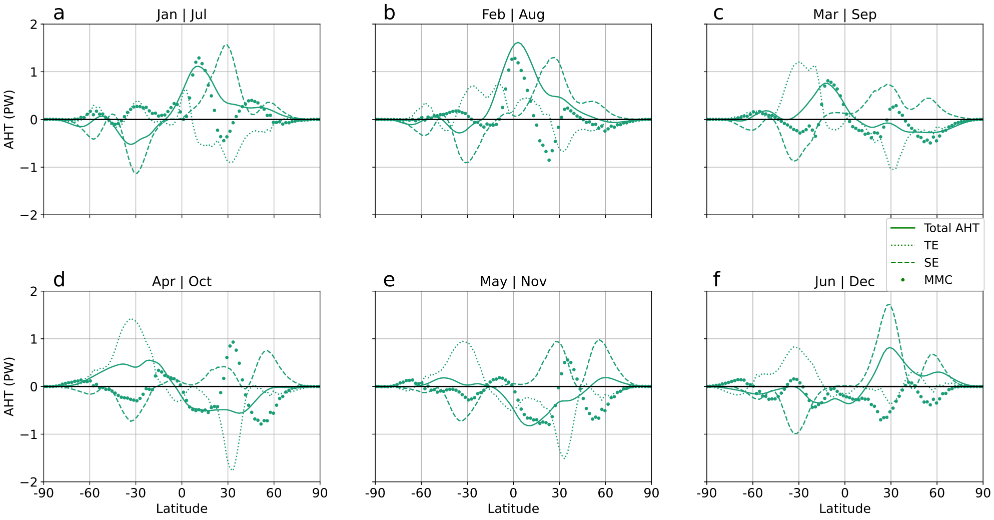

Figure 2.8: Monthly-averaged anomalies in total AHT and its dynamic components for the two-mountain AM2 seasonal simulation, where anomalies are calculated as seasonal two-mountain simulation minus seasonal control. The results are symmetric across the equator with a six-month lag, so to increase the sample size and decrease the number of plots we have combined months by taking months July through December, mirroring them across the equator, flipping the sign, and then averaging them with months January through June. For example, plot a) is the AHT anomalies in January and if mirrored across the equator with a sign change, is also the AHT anomalies for July.

Chapter 3

THE GAUSSIAN NATURE OF ZONALLY INTEGRATED ATMOSPHERIC HEAT TRANSPORT

3.1 *Introduction*

Meridional atmospheric heat transport (AHT) has long been recognized as important for understanding Earth's hydrologic and energetic balances (e.g., Pierrehumbert, 2010, Held and Soden, 2006, Siler et al., 2018). Recent research has analyzed high temporal resolution (often 6-hourly) AHT with a particular focus on the largest magnitude AHT events. This research has suggested that individual AHT events can play a large role in the amount of AHT in a season (Lembo et al., 2019, Messori and Czaja, 2013, 2014, 2015, Liu and Barnes, 2015). Additionally, individual AHT events have been shown to play an important part in driving the variability of Arctic sea ice and Arctic warming (Woods et al., 2013, Laliberté and Kushner, 2014, Woods and Caballero, 2016, Mortin et al., 2016, Doyle et al., 2011, Cardinale and Rose, 2022, Kapsch et al., 2013, Messori et al., 2018). Given the apparent importance of individual AHT events, much of the research into AHT has shifted towards trying to understand the unique drivers of extreme AHT events.

Most of this previous work has also focused on the role of local AHT events (i.e., AHT events at individual grid points) rather than zonally integrated AHT. For local AHT events, this work has found that extreme events contribute disproportionately (as compared to a Gaussian distribution) to the amount of local AHT over a season (Messori and Czaja, 2013, 2014, 2015, Liu and Barnes, 2015). The role of extreme events in zonally integrated AHT has received less attention, but existing research suggests that zonally integrated extreme events do not play as major a role in the amount of AHT in a season (Messori and Czaja, 2015, Messori et al., 2017, Lembo et al., 2019). However, research has still tended to focus on the most extreme events (Lembo et al., 2019). If extreme events play a disproportionate role for zonally integrated total AHT, then it becomes important to understand the unique drivers of the most extreme AHT events, as previous work has done. However, if extreme events do not play a disproportionate role for zonally integrated total AHT, then it may be more important to understand what sets the mean and variability of AHT, rather than mechanisms of individual events. Existing research has skewed heavily towards understanding the drivers of the most extreme zonally integrated AHT events (Messori and Czaja, 2015, Messori et al., 2017, Lembo et al., 2019), and in this work we aim to assess if this focus is justified. We focus on zonally integrated AHT in this work given its close connection to Earth's energy budget and hydrologic cycle.

The previous work on this topic has employed several different methodologies for calculating AHT at 6-hourly temporal resolution, adding to the ambiguity about the importance of extreme AHT events. This introduces questions about which methodology is the most physically relevant and whether results are dependent upon the choice of AHT methodology.

Our primary goal in this work is to better understand how AHT varies in time using high-resolution ERA5 data (Hersbach et al., 2018b). We develop a new method of calculating AHT (Section 3.2), that is more closely connected to heating of the atmospheric column than previous methodologies (Section 3.3). In addition, in the time-mean AHT calculated with our new methodology is nearly identical to the AHT derived from more standard AHT calculations based on monthly atmospheric fields (e.g., Trenberth and Stepaniak, 2003a, Donohoe et al., 2020). Using this new method of calculating AHT, we find that zonally integrated total AHT at any given latitude and season closely approximates a Gaussian distribution with a limited role for extreme events (Sections 3.4 and 3.5). We further consider zonally integrated total AHT by examining its two components (eddies and the mean-meridional circulation (MMC)) and connections between the two (Sections 3.6 and 3.7). Distributions of both zonally integrated eddy and MMC AHT are also nearly Gaussian (for purposes relating to the importance of extreme events), and they are negatively correlated on 6-hourly time scales, suggesting compensation between eddy and MMC AHT components. Lastly, we consider connections between local eddy AHT and zonally integrated eddy AHT (Section 3.8).

3.2 *Methods*

We first develop a new method of calculating zonally integrated total AHT at any instant from three-dimensional atmospheric fields. Our method results in the same time-mean zonally integrated AHT that is calculated from monthly-mean fields and eddy covariances (e.g., Trenberth and Stepaniak, 2003a, Donohoe et al., 2020) and is shown to be closely connected to heating of the atmospheric column. We provide a detailed methodology section to illustrate how our calculation compares to that in previous work. Our AHT calculation is performed at each instant independently and makes no reference to the time-mean fields, which differs from Messori and Czaja (2013) who calculated the transient-eddy portion of the AHT from the product of the temporal anomalies, relative to the time-mean, in v and MSE at each grid point. It also differs from Lembo et al. (2019) who calculated AHT as a function of wavenumber at each instant. All heat-transport calculations are performed using ERA5 data from 1979-2018 at 0.5° horizontal resolution, with 37 vertical levels, and with 6-hourly temporal resolution (Hersbach et al., 2018b).

The relevant energetic quantity is the moist static energy (MSE) defined as:

$$\mathrm{MSE} = c_p T + L_v q + gZ, \tag{3.1}$$

where c_p is the specific heat of air, T is the atmospheric temperature, L_v is the latent heat of vaporization, q is the specific humidity, g is the acceleration due to gravity, and Z is the geopotential height.

In our formulation of AHT, we calculate the net transport of MSE across a latitude band relative to an unchanging atmospheric mass. Non-zero mass fluxes do not change our AHT calculation and, thus, AHT acts to change the mean MSE poleward of that latitude. In this framework, AHT can be thought of as depending on the MSE contrasts between poleward and equatorward moving air. Zonally integrated AHT at a given latitude can be accomplished by two distinct types of circulations: 1) at a given pressure level, zonal anomalies in meridional winds acting on zonal anomalies in MSE (hereafter eddies) and 2) zonal-mean meridional winds at different pressure levels acting on the vertical gradient in MSE (hereafter the MMC). Mathematically, these two contributions to instantaneous AHT at a given latitude (ϕ) are calculated as:

$$\text{Total AHT} = \frac{2\pi a\ cos(\phi)}{g} \int_0^{\overline{P_s}} \left(\underbrace{[v]^{\dagger}[\text{MSE}]^{\dagger}}_{\text{MMC AHT}} + \underbrace{[v^{*}\text{MSE}^{*}]}_{\text{Eddy AHT}} \right) dp, \tag{3.2}$$

where v is the meridional wind, p is pressure, P_s is the surface pressure, a is the radius of Earth, square brackets [ ] denote zonal averages, ($\overline{\ \ }$) denote time averages, asterisks (*) are departures from the zonal average, and swords (†) are departures from the vertical average. This formulation implicitly conserves mass prior to calculation of the MMC AHT by removing the vertical average v and MSE (Marshall et al., 2014), and requires no further barotropic wind adjustment (Trenberth and Stepaniak, 2003a). If the vertical averages are not removed, the magnitude and variance of the MMC AHT changes due to mass fluxes. The AHT due to the mass fluxes alone can be found by multiplying the zonal- and vertical-mean v with the zonal- and vertical-mean MSE. Mathematically, the AHT due to mass transport is:

$$\text{AHT Mass Transport} = \frac{2\pi a\ cos(\phi)}{g} \left([\hat{v}]\,[\widehat{\text{MSE}}] \right), \tag{3.3}$$

where ($\hat{\ }$) is a vertical-average and is defined as:

$$\hat{X} \equiv \frac{1}{\overline{P_s}} \int_0^{\overline{P_s}} (X)\ dp. \tag{3.4}$$

At individual instants the AHT due to the mass fluxes can be large. Figure 3.2 shows that the standard deviation of the AHT Mass Transport (Eqn. 3.3) is actually larger than the standard deviation of the Total AHT (Eqn. 3.2), showing the importance of accounting for such mass fluxes in the AHT calculation (Liang et al., 2018). We choose to remove the mass flux due to the the lack of mass conservation in reanalysis data (Mayer et al., 2021), lack of connection between mass fluxes and relevant climate variables such as heating of the atmospheric column or connections to ENSO (Liang et al., 2018), and difficulty physically interpreting the mass fluxes (Cardinale et al., 2021).

In order to relate our methodology to the climatological AHT and previous work on the temporal variability of AHT, it is instructive to decompose the eddy fields (v^* and MSE*) into time-mean stationary eddies ($\overline{v^*}$ and $\overline{\text{MSE}^*}$) and transient eddies (v^*’ and MSE*’), where (’) are departures from the time average. The eddy AHT at a given instant and latitude is then:

$$\text{Eddy AHT} = \frac{2\pi a\ cos(\phi)}{g} \int_0^{\overline{P_s}} \left(\underbrace{[\overline{v^*}\,\overline{\text{MSE}^*}]}_{\text{Stationary Eddy}} + \underbrace{[\overline{v^*}\text{MSE}^{*'}] + [v^{*'}\overline{\text{MSE}^*}]}_{\text{Mixed Terms}} + \underbrace{[v^{*'}\text{MSE}^{*'}]}_{\text{Transient Eddy}} \right) dp. \tag{3.5}$$

To calculate the climatological eddy AHT we take the time average of Eq. 3.5 which gives

$$\overline{\text{Eddy AHT}} = \frac{2\pi a\ cos(\phi)}{g} \int_0^{\overline{P_s}} \left(\underbrace{[\overline{v^*}\,\overline{\text{MSE}^*}]}_{\text{Stationary Eddy}} + \underbrace{[\overline{v^{*'}\text{MSE}^{*'}}]}_{\text{Transient Eddy}} \right) dp. \tag{3.6}$$

The time-mean of the Mixed Terms in Eq. 3.5 is zero because the time-mean terms ($\overline{v^*}$ and $\overline{\text{MSE}^*}$) can be pulled out of the time averaging operator and the time-mean of the transient terms (v^*’ and MSE*’) is zero by definition. Thus, in the time-mean climatology, stationary and transient eddies do not interact and the eddy AHT can be decomposed into contributions from the stationary eddies and the transient eddies, which results from temporal covariance between v and MSE in baroclinic eddies (Lorenz, 1953). Indeed, in the time-mean, the AHT calculated from Eq. 3.2 is nearly identical to the sum of transient eddy and stationary eddy AHT derived from more standard AHT calculations (Donohoe et al., 2020) based on monthly mean atmospheric fields and eddy covariances (Fig. 3.1).

However, at any instant the transient eddies in v and MSE (v^*’ and MSE*’) can interact with the stationary eddies in v and MSE ($\overline{v^*}$ and $\overline{\text{MSE}^*}$) to result in non-zero contribution to the instantaneous eddy AHT by the Mixed Terms. This contribution is associated with the time-mean circulation advecting temporal anomalies in MSE and the anomalous eddy mass transports advecting the time-mean eddy MSE field respectively. Some previous work on the temporal variability of AHT (Messori and Czaja, 2013, 2014, 2015) did not diagnose the impact of the Mixed Terms on AHT variability and instead focused solely on the transient eddies. We note that there is no *a priori* expectation on whether the Mixed Terms will enhance or diminish the temporal variability (or higher order moments) of the AHT distribution. However, if the climatological structures of MSE and v (which contribute to poleward AHT) were amplified (and diminished) in concert over time, we expect the AHT temporal variability to be enhanced by the mixed terms.

Temporal variations in the MMC AHT also depend on the interaction between the time-mean of the zonal-mean v and MSE ($\overline{[\mathrm{MSE}]^{\dagger}}$ and $\overline{[v]^{\dagger}}$) interacting with the temporal-anomalies of zonal-mean v and MSE ($[\mathrm{MSE}]^{\dagger\prime}$ and $[v]^{\dagger\prime}$):

$$\text{MMC AHT} = \frac{2\pi a\ cos(\phi)}{g}\int_0^{\overline{P_s}}\left(\underbrace{[\overline{v^{\dagger}}][\overline{\mathrm{MSE}^{\dagger}}]}_{\text{TMMC}} + \underbrace{[\overline{v^{\dagger}}][\mathrm{MSE}^{\dagger\prime}] + [v^{\dagger\prime}][\overline{\mathrm{MSE}^{\dagger}}]}_{\text{Mixed Terms}} + \underbrace{[v^{\dagger\prime}][\mathrm{MSE}^{\dagger\prime}]}_{\text{TOC}}\right) dp, \tag{3.7}$$

where TMMC is the time-mean meridional overturning circulation and TOC is the transient overturning circulation. Temporal anomalies in the mass overturning circulation of the atmosphere ($[v]^{\dagger\prime}$), such as intensifications of the Hadley and Ferrel cells, can transport energy poleward by way of the climatological gross moist stability (GMS) of the atmosphere ($\overline{\mathrm{MSE}}^{\dagger}$) even if there are no associated temporal anomalies in GMS. As a result, temporal anomalies in the MMC AHT are much larger than those in the TOC alone which requires a temporal co-variability of GMS and mass overturning circulations (Marshall et al., 2014).

The time-mean MMC is calculated from the time-mean of Eq. 3.7:

$$\overline{\text{MMC AHT}} = \frac{2\pi a\ cos(\phi)}{g}\int_0^{\overline{P_s}}\left(\underbrace{[\overline{v^{\dagger}}][\overline{\mathrm{MSE}^{\dagger}}]}_{\text{TMMC}} + \underbrace{\overline{[v^{\dagger\prime}][\mathrm{MSE}^{\dagger\prime}]}}_{\text{TOC}}\right) dp. \tag{3.8}$$

where, as in the eddy AHT, the mixed terms make no contribution to the climatological MMC AHT, but make a non-zero contribution to the instantaneous MMC AHT. The time-mean of our instantaneous MMC AHT calculation (Eq. 3.2) is nearly identical to that calculated from the (monthly) time-mean fields alone (Fig. 3.1) suggesting the TOC ($\overline{[v^{\dagger\prime}][\mathrm{MSE}^{\dagger\prime}]}$) makes a negligible contribution to MMC AHT.

Unless otherwise specified, future references to total AHT, eddy AHT, and MMC AHT refer to the zonally integrated quantity. Throughout this work we refer to skewness, the third standardized moment of a distribution and a measure of asymmetry in a distribution, and kurtosis, the fourth standardized moment of a distribution and a measure of narrowness of the distribution. The term disproportionate is used to refer to the importance of extreme events compared to a Gaussian distribution with the same mean and standard deviation. While previous work has shown that the impact of individual AHT events on Arctic climate can depend on their vertical structure rather than just their magnitude (Cardinale et al., 2021, Cardinale and Rose, 2022, Woods et al., 2013), we focus on vertically-integrated AHT given our focus on all latitudes.

3.3 *Connection between AHT and column heating*

Previous work by Liang et al. (2018) has suggested that removing the AHT associated with non-zero mass transport can improve connections between AHT and relevant variables such as ENSO and total atmospheric energy content. We use the zonal-mean column MSE tendency to evaluate how well our methodology, and previous methodologies, is connected to atmospheric energy changes. We calculate the zonal-mean column MSE tendency (hereafter MSE tendency) as:

$$\text{MSE tendency} = \frac{\partial}{\partial t}[\hat{\text{MSE}}]. \tag{3.9}$$

In Figure 3.3a we show that the meridional convergence of total AHT without the mass fluxes (as in Equation 3.2) correlates well with the MSE tendency. In much of the mid-latitudes the correlations for total AHT are near 0.8, showing that our AHT calculation methodology is accurately capturing the transport of heat within the atmosphere. Figure 3.3a also shows that the meridional convergence of total AHT with the mass fluxes removed correlates much better with the MSE tendency than when the mass fluxes are included, reinforcing the benefit of removing the AHT associated with mass fluxes. The AHT associated with the mass fluxes is weakly negatively correlated with the MSE tendency. We hypothesize that this is because instants of mass divergence are associated with instants when the column is warm under the presence of thermal lows.

We also compare our AHT methodology with that in previous work in Figure 3.3b. The meridional convergence of our eddy AHT calculations show stronger correlations with the column

MSE tendency than the meridional convergence of the TE AHT used in Messori and Czaja (2013, 2015) at all latitudes. This shows that, at least by one metric, our AHT calculation methodology presents an improvement over past efforts. The lower correlations for total AHT in the tropics may be related to known deficiencies in reanalysis' representation of precipitation and latent heating there (e.g., Chemke and Polvani, 2019, and 4.3.2). Altogether, this suggests that our AHT methodology improves over previous work and is closely connected to the MSE tendency.

3.4 *Seasonal distributions of total AHT*

We first examine distributions of total AHT broken down by season. In Figure 3.4 we show distributions of total AHT at 40°N and 60°N where the solid lines show Gaussian distributions with the same mean and standard deviation as the underlying distributions. Any one season of total AHT is visually nearly Gaussian (as seen in Fig. 3.4 by the close agreement between the bar distributions and the solid lines). The sum of these visually near-Gaussian distributions creates an annual distribution that is less Gaussian and has noticeable skewness (Fig. 3.4i,j), primarily because winter AHT has a larger mean and larger standard of deviation than other seasons. This is qualitatively similar to the results of Lembo et al. (2019) who calculated AHT as a function of wavenumber.

Another way to understand how seasonality introduces skewness into the distributions is to look at probability density functions (PDFs) of annual total AHT with the underlying seasonal cycle removed. The bottom two rows of Figure 3.4 show total AHT distributions both with and without a seasonal cycle. We deseasonalize the AHT timeseries (and distributions) by removing a smoothed seasonal cycle defined by a periodic spline with eight knots (points where the function defining the seasonal cycle change) per year fit to all years of data. When the seasonal cycle is removed, the total AHT distributions are nearly Gaussian, while with a seasonal cycle, there is a noticeable positive skewness. This is also reflected in summary statistics for annual total AHT distributions, with a skewness of 0.6 at 40°N and 0.7 at 60°N when the seasonal cycle is included and 0.3 at 40°N and 0.3 at 60°N when the seasonal cycle is removed. We show the effect of seasonality only for total AHT, but the same results apply for eddy and MMC AHT. Latitudes other than 40°N and

60°N have similar roles for seasonality. We focus on AHT data during DJF for the remainder of this chapter, but note that similar conclusions apply for other seasons.

3.5 *The importance of separating latitudes*

When evaluating AHT at the hemispheric scale, it can be tempting to examine PDFs of AHT for all latitudes in a hemisphere. Previous work found that, when aggregating transient eddy AHT distributions for all latitudes from 30° to 89°N, AHT is most often near zero, and extreme AHT events make a disproportionate contribution to the time-integrated AHT, indicating that distributions are not very Gaussian (Messori and Czaja, 2015, Messori et al., 2017). However, Lembo et al. (2019) aggregated total AHT distributions from 30° to 60°N and found that the aggregate distribution was approximately Gaussian. We use our new AHT calculation methodology to compare to these previous results and to investigate the extent that PDFs of total AHT within the Northern Hemisphere are representative of PDFs at any single latitude.

We examine PDFs of total AHT during DJF at 30°, 40°, 50°, 60°, 70°, and 80°N as well as the aggregation of these latitudes (Fig. 3.5). The solid lines show Gaussian distributions with the same mean and standard deviation as the underlying distributions. In the PDF of the combined latitudes (Fig. 3.5a) there is a two-peaked structure with one peak near 0 PW, and another near 5 PW. This is similar to the PDF of transient eddy AHT in Messori and Czaja (2015) (their Fig. 7a), although our PDF has a more noticeable two-peaked structure, likely due to the inclusion of other AHT components. However, the PDF for any one latitude closely approximates a Gaussian distribution. A quantitative comparison to Gaussian distributions is discussed in Section 3.6 and shown in Table 3.1.

The apparent skewness and the double-peaked structure of the hemispheric PDF is largely a result of aggregating nearly-Gaussian distributions from different latitudes that have different means and standard deviations. The PDFs at different latitudes have different mean and standard deviation values in part due to the latitudinal dependence on zonal circumference (e.g., the $cos(\theta)$ term in Eq. 3.2). The non-Gaussian nature of the hemispheric AHT PDF is not indicative of the physics of AHT, but is instead an artifact of aggregating PDFs of data from multiple latitudes. Combining all latitudes from 30° to 89°N produces a similar PDF (not shown), as does looking at eddy AHT instead of total AHT (not shown). Combining only latitudes from 30° to 60°N produces a much more Gaussian distribution (as in Lembo et al. (2019), their figure 1b), so much of the two-peaked structure comes from including latitudes poleward of 60°N, where the mean AHT tends toward zero. Using the AHT calculation methodology in Messori and Czaja (2013) produces similar results, indicating that the methodology of calculating AHT does not strongly impact this result. The nearly-Gaussian AHT distributions at each latitude suggest that understanding what sets the mean and variability of zonally-integrated AHT may be more important than understanding drivers of individual events.

3.6 *Distributions of individual AHT components*

In Figure 3.6 we show PDFs of the total AHT (panels a,c) and its two components, eddy AHT (panels a,c) and MMC AHT (panels b,d) at both 40°N and 60°N (results are similar for other mid- and high-latitude locations). As before, the solid lines show Gaussian distributions with the same mean and standard deviation as the underlying distributions.

Table 3.1 shows summary statistics for the total, eddy, and MMC AHT (as well as for the local eddy AHT discussed in Section 7) together, with comparisons to Gaussian distributions, which would have skewness and excess kurtosis of 0 (e.g., Ramsey et al., 2002). Comparing distributions to their Gaussian equivalents can help put into context the general shape of the distributions and the extent to which extreme events are important, as extreme values do not play a major role in Gaussian distributions. Despite many of our distributions appearing visually indistinguishable from a Gaussian distribution they all fail numerous tests for Gaussianity including the Kolmogorov-Smirnov, Shapiro-Wilk, and Anderson-Darling tests (e.g., Thode, 2002). This occurs because our distributions have very large numbers of data points (14,440 for zonally-integrated AHT distributions and 10,396,800 for local eddy AHT distributions), which makes small deviations from perfect Gaussian distributions statistically significant. To gain additional insight into the Gaussian-nature of our distributions we employ two different measures.

The first measure compares an entire distribution against a Gaussian distribution by standardizing the distribution and then comparing the quantile of each data point against the expected quantile if the distribution were perfectly Gaussian. We then calculate the root-mean-square error between the actual and Gaussian quantiles and refer to this value as the Q-Q RMSE (Table 3.1). A perfect Gaussian distribution would have a Q-Q RMSE of 0, while the bimodal distribution in Figure 3.5a has a Q-Q RMSE of 0.11 and the mean Q-Q RMSE of distributions in Figures 3.5b-g is 0.05. The second measure characterizes the importance of extreme events following Messori and Czaja (2013) by calculating what percentage of the positive portion of the PDFs come from the top 5% of events for each field (Table 3.1); we also list the equivalent values for the Gaussian distributions. For fields where the mean AHT is negative (MMC AHT, Figs. 3.6b,d), we find the percentage that the bottom 5% of events contribute to the negative portion of the distribution. Throughout this work we refer to many of the distributions as nearly-Gaussian, even if they fail tests for Gaussianity, since they appear Gaussian and their summary statistics are similar to Gaussian distributions.

Total AHT PDFs (darker colors and black lines, Figs. 3.6a,c) are visually nearly Gaussian. Notably, the role of extreme events is similar between total AHT PDFs and their Gaussian equivalents (8.2% versus 7.9% at 40°N and 10.0% versus 9.6% at 60°N, Table 3.1). Eddy AHT PDFs (blue colors and lines, Figs. 3.6a,c) are similar to total AHT PDFs at 40°N and 60°N, primarily because most AHT at these latitudes is accomplished by eddies. Eddy AHT PDFs are visually more Gaussian than the PDFs of eddy AHT in Lembo et al. (2019) (in their case wavenumber 1-5 and 6-10, their Fig. 2b,c) due to their combining of latitudes from 30°N to 60°N. Using our dataset and combining eddy AHT from 30°N to 60°N produces a PDF similar to theirs (not shown). The standard deviation in eddy AHT is larger than that for total AHT, particularly at 60°N (2.2 PW for eddy AHT versus 1.7 PW for total AHT, Table 3.1). Reasons for these differences in standard deviation will be further explored in Section 6.

The MMC AHT PDF at 40°N (Fig. 3.6b) is visually nearly Gaussian, while at 60°N (Fig. 3.6d) the MMC AHT PDF has a more noticeable negative skew. The role of extreme events for the MMC AHT is greater than for eddy or total AHT. However, extreme events have similar importance between the MMC AHT PDFs and their Gaussian equivalents (at 60°N 15.9% for the actual distribution and 15.0% for the Gaussian equivalent). This indicates that the MMC AHT has a larger role for extreme events than does eddy or total AHT primarily because the mean of the MMC AHT is closer to 0.

Overall, PDFs and summary statistics of various AHT fields indicate that, if distributions are separated by latitude and season, total AHT, and its components (eddies and the MMC), are visually nearly Gaussian. While all these distributions fail standard test for Gaussianity, for purposes relating to the importance of extreme events, these distributions are nearly Gaussian. We next focus on the temporal relationship between eddy and MMC AHT.

3.7 *Connections between eddy and MMC AHT*

Total AHT is the sum of eddy and MMC AHT, which do not operate independently of one another. In the time-mean, previous work has found connections between eddies and the MMC in both the mid-latitudes (e.g., Salustri and Stone, 1983) and sub-tropics (e.g., Walker and Schneider, 2006). Extensive theory about the transformed-Eulerian mean (TEM) provides expectation that eddy and MMC AHT will counteract eachother. However, it is not clear from TEM theory what one should expect on 6-hourly time scales, nor what the degree of compensation between eddy and MMC AHT components should be. Lembo et al. (2019) examined connections between eddies and the MMC at 6-hourly time scales during the largest magnitude total AHT events (rather than all AHT events) and found the MMC AHT plays a minor role in such AHT events.

We caution that at 6-hourly time scales, an increase in MMC AHT does not mean that a zonally-uniform change in MMC AHT is occurring as synoptic-scale storms drive regional variability. Despite this caveat, relationships between eddy and MMC AHT can provide useful context about the temporal variability of total AHT.

We investigate the relationship between 6-hourly eddy and MMC AHT by calculating linear regression slopes between eddy AHT and MMC AHT at each latitude during DJF. We use these regression slopes to find correlation coefficients at each latitude. Figure 3.7 shows the slopes and the squares of the correlation coefficients (r^2). The regression slopes are negative at all latitudes and the magnitude of the slopes and r^2 values peak in the mid- and high-latitudes. Negative slopes mean that increased poleward eddy AHT is associated with decreased poleward (or more equatorward)

AHT by the MMC. In the mid-latitudes this means that, on average, a six-hour period with a large amount of poleward eddy AHT is associated with a strengthened thermally-indirect Ferrell cell. All the slopes have a magnitude less than 1 meaning that, on average, the MMC AHT adjustment only partially compensates for the eddy AHT changes. Slopes peak around 0.4 in the Northern Hemisphere storm track between 50-70°N. A slope of 0.4 implies that total AHT events are about 60% as large as from eddy AHT alone. While partial adjustment is expected from TEM theory, this is to our knowledge the first demonstration and quantification of this AHT compensation on 6-hourly time-scales.

One result of this negative correlation is that in the mid- and high-latitudes, total AHT has a smaller standard deviation than eddy AHT (1.7 PW versus 2.2 PW at 60°N, Table 3.1). This effect becomes more noticeable at higher latitudes. If we only look at extreme total AHT events, as in Lembo et al. (2019), the negative correlation between eddy and MMC AHT is more difficult to discern due to eddy AHT doing the bulk of AHT during extreme total AHT events. Given the nearly-Gaussian nature of total AHT for any given season, we argue it is important to consider the full distribution of AHT events, not just the extremes.

3.8 *Connecting local eddy AHT and zonally integrated eddy AHT*

Thus far, we have focused on zonally integrated AHT. We now consider the temporal distribution of local eddy AHT defined at each latitude (ϕ) and longitude (θ) as:

$$\text{Local eddy AHT}(\phi, \theta) = \frac{2\pi a\; cos(\phi)}{g} \int_0^{P_s} \left(v(\phi, \theta)^* \; \text{MSE}(\phi, \theta)^*\right) \, dp. \tag{3.10}$$

To allow for more straightforward comparison between local eddy AHT and zonally integrated eddy AHT, we multiply local eddy AHT values by the circumference of their respective latitude band, so that the local eddy AHT values are what would be realized if the local values were occurring uniformly across all longitudes. The temporal distribution of local transient eddy AHT was previously considered by several papers including Messori and Czaja (2013, 2014, 2015) and Messori et al. (2017). Our calculation differs from these previous studies and instead defines eddies as zonal-anomalies at each time rather than temporal-anomalies at each grid point. As discussed in Section 3.2 and shown in Figure 3.3, our AHT calculation shows better correlations with the vertically-averaged MSE tendency, likely because our calculation includes transient eddies, stationary eddies, and cross-terms between the two. There is no physically relevant local MMC AHT quantity, since the MMC AHT is defined from zonal-mean fields.

The distributions of local eddy AHT for 40°N and 60°N aggregated across all longitudes are shown in Fig. 3.8a,d alongside the zonally integrated eddy AHT distributions. Local eddy AHT distributions are the least Gaussian of any of the fields analyzed, and feature narrow peaks near 0 PW and long tails (red PDFs and lines left-hand columns, Fig. 3.8). These traits are reflected by large excess-kurtosis values of 7.6 at 40°N and 6.6 at 60°N and Q-Q RMSE values that are roughly 4-5 times larger than the zonally-integrated eddy AHT values (Table 3.1). Additionally, extreme local eddy AHT events contribute a large fraction to the sum of local eddy AHT; the top 5% of local eddy AHT events contribute to 33.1 and 29.6 percent of the sum at 40°N and 60°N respectively (Table 3.1). This result is smaller than the findings of Messori and Czaja (2013), who analyzed transient eddies only and found that the top 5% of local events made up 39.3 percent of the sum at 45°N and 36.5 percent at 60°N. While it is tempting to conclude that the large positive skewness and excess kurtosis values are responsible for the large role of extreme events in local eddy AHT, the top 5% of Gaussian equivalent distributions of local eddy AHT at 40°N and 60°N contribute 19.7% and 20.1% of the sums respectively. Therefore, while extreme events do play a large role for local eddy AHT, much of this comes from their large standard-deviation values, rather than large skewness or excess kurtosis values.

We note that aggregating distributions across all longitudes can result in the appearance that local eddy AHT has more skewness or kurtosis than the underlying distributions at individual longitudes would suggest. This is similar to issues that can arise when not separating zonally integrated AHT by latitude or season. However, removing the mean local eddy AHT from each grid point before aggregating distributions results in a similar standard deviation to if the means are not removed (at 40°N, 17.3 PW with the full fields versus 17.2 PW with the means at each grid point removed), suggesting that aggregating distributions across longitudes is a not a major issue.

The discrepancies between local eddy AHT and zonally integrated eddy AHT distributions (local eddy AHT (red) and zonally integrated eddy AHT (black), Fig. 3.8a,d) lead to the question: how can we reconcile the nearly Gaussian zonally integrated eddy AHT distributions and the non-Gaussian local eddy AHT distributions?

We address this by attempting to recreate the zonally integrated eddy AHT distributions by randomly sampling the local eddy AHT distributions. This approach is dynamically naïve, in that we are assuming local eddy AHT is uncorrelated between longitudes. Specifically, we sample the local eddy AHT distribution N times, where N=14,440, which is the number of time steps in the dataset. For each sample, we select random times for each grid point in the local eddy AHT distribution. This ultimately creates a PDF of randomly sampled local eddy AHT (red colors, middle columns, Fig. 3.8). As the middle columns of Figure 3.8 show, this random sampling creates PDFs with a much smaller standard deviation than the zonally integrated eddy AHT distributions at both 40°N and 60°N, as is expected from the central limit theorem. This shows that, unsurprisingly, the eddy AHT distributions are not random assortments of local eddy AHT data, and instead temporal and spatial connections between local eddy AHT at different longitudes are important.

We then try to recreate the zonally integrated eddy AHT distributions from the local eddy AHT distributions by incorporating a zonal decorrelation length scale, L. We consider each latitude circle separately. At each grid point around this circle, we calculate the temporal autocorrelation coefficient of local eddy AHT as a function of longitude, and define the decorrelation length scale as that distance at which the autocorrelation coefficient falls to 1/e. We do this at every grid point, and the zonal average of these length scales is equivalent to 7.2° at 40°N and 11.5° at 60°N. Due to the variation of zonal-circumference with latitude, these length scales are equivalent to 614 km at 40°N and 640 km at 60°N, respectively, and are similar to that found in previous work that explored eddy length scales (e.g., Barnes and Hartmann, 2012). We now randomly sample points $2L$ apart at the same time step. We sample points $2L$ apart, as this is the distance between independent points (e.g., Bretherton et al., 1999) This results in each sample containing 24 points at 40°N and 15 points at 60°N. We again take N samples. The result is shown in the righthand columns of Figure 3.8, and shows better, but not perfect, agreement with the zonally integrated eddy AHT distribution. Overall this suggests that the zonally integrated eddy AHT can be approximated to first order as sporadic local eddy AHT events with a quantifiable spatial structure. Discrepancies between the distributions from this sampling method and the actual zonally integrated eddy AHT distributions likely come from non-zero correlations beyond L, including negative correlations between approximately $1.5L$ and $6L$ (not shown).

3.9 *Summary and Conclusions*

We developed a new method of calculating AHT on 6-hourly time-scales to separate zonally integrated total AHT into eddy and MMC components. This differs from most previous 6-hourly resolution AHT work that focused on transient eddy AHT generated by local temporal-anomalies (Messori and Czaja, 2013, 2014, 2015, Messori et al., 2017) or decomposed AHT by wavenumber (Lembo et al., 2019). Our novel definition of AHT is indifferent to the mass budget of the atmosphere and is more strongly connected to the heating of the atmospheric column than previous metrics. We have evaluated the resulting AHT PDFs with a particular focus on the extent to which distributions are Gaussian.

While much of the existing literature has focused on extreme AHT events, we find that extreme events do not play a disproportionate role in any of the zonally integrated AHT fields. For any given season and latitude, zonally integrated total AHT and its zonally integrated components (eddies and the MMC) are all nearly Gaussian. We find these two components are negatively correlated on 6-hourly time scales. Local eddy AHT distributions are less Gaussian, with a larger role for extreme events, although this role is smaller than that found in other work (Messori and Czaja, 2013, 2014, 2015). We've shown that we can partially recreate the zonally integrated eddy AHT distributions by resampling the local eddy AHT using a decorrelation length scale. This suggests that, to first-order, zonally integrated eddy AHT is made up of sporadically occurring local eddy AHT events with a quantifiable average spatial structure.

The focus in this chapter has been on PDFs of zonally integrated total AHT, which we chose motivated by implications for the zonal-mean energy budget. Given that extreme events do not play a disproportionate role in zonally integrated total AHT, focusing on the factors that control the

Table 3.1: Summary statistics for various AHT distributions. The 30-80°N row contains the combined distributions from 30, 40, 50, 60, 70, and 80°N. Skewness, the third moment of a distribution, is a measure of asymmetry in the distribution, and excess kurtosis, the fourth moment of a distribution, is a measure of the narrowness of a distribution. Skewness and excess kurtosis are both 0 for a Gaussian distribution. Skewness and excess kurtosis values that are statistically different from 0 are noted with a * or ‡ for the 95% confidence level and 99% confidence level, respectively. See Section 3.6 for details on the Q-Q RMSE and top 5% calculations and Section 3.8 for details about how the local AHT calculation is performed.

Latitude	Field	Mean (PW)	Std. Dev. (PW)	Skewness	Excess Kurtosis	Q-Q RMSE	Top 5% events	Top 5% Gaussian
30-80°N	Total AHT	3.9	2.6	$0.2^\ddagger$	$-0.8^\ddagger$	0.11	11.8	11.8
40°N	Total AHT	6.5	1.8	$0.3^\ddagger$	$0.3^\ddagger$	0.05	8.2	7.9
40°N	Eddy AHT	6.7	2.0	$0.3^\ddagger$	$0.1^\star$	0.06	8.3	8.1
40°N	Local Eddy	6.7	17	$1.9^\ddagger$	$7.6^\ddagger$	0.31	33.1	19.7
40°N	MMC AHT	-0.2	1.1	0.0	0.1	0.01	22.9	22.5
60°N	Total AHT	3.7	1.7	$0.3^\ddagger$	$0.2^\ddagger$	0.04	10.0	9.6
60°N	Eddy AHT	4.8	2.2	$0.4^\ddagger$	$0.2^\ddagger$	0.07	10.1	9.6
60°N	Local Eddy	4.8	14	$1.3^\ddagger$	$6.6^\ddagger$	0.22	29.6	20.1
60°N	MMC AHT	-1.2	1.3	$-0.3^\ddagger$	$0.1^\ddagger$	0.05	15.9	15.0

mean and variability of AHT may be more important for climate than understanding the drivers of the most extreme AHT events.

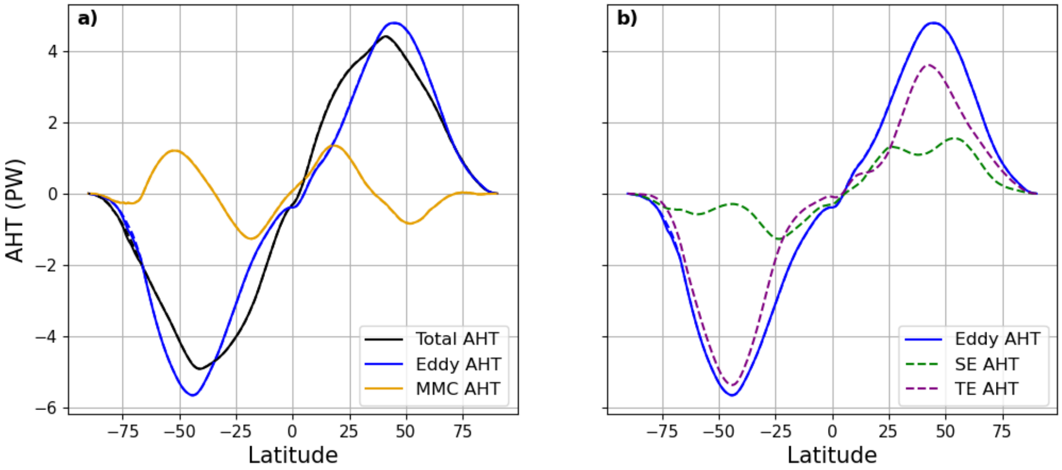

Figure 3.1: Annual time-mean northward AHT from the methodology in this chapter (solid lines) and that at monthly time scales as in Donohoe et al. (2020) (dashed lines). In a) AHT by eddies (blue), the MMC (yellow), and the total (black) and in b) the same AHT by eddies as in a) (blue), SEs (green), and TEs (purple). The lines are almost entirely overlapping, denoting excellent agreement. Note that the instantaneous AHT calculation does not separate TEs and SEs.

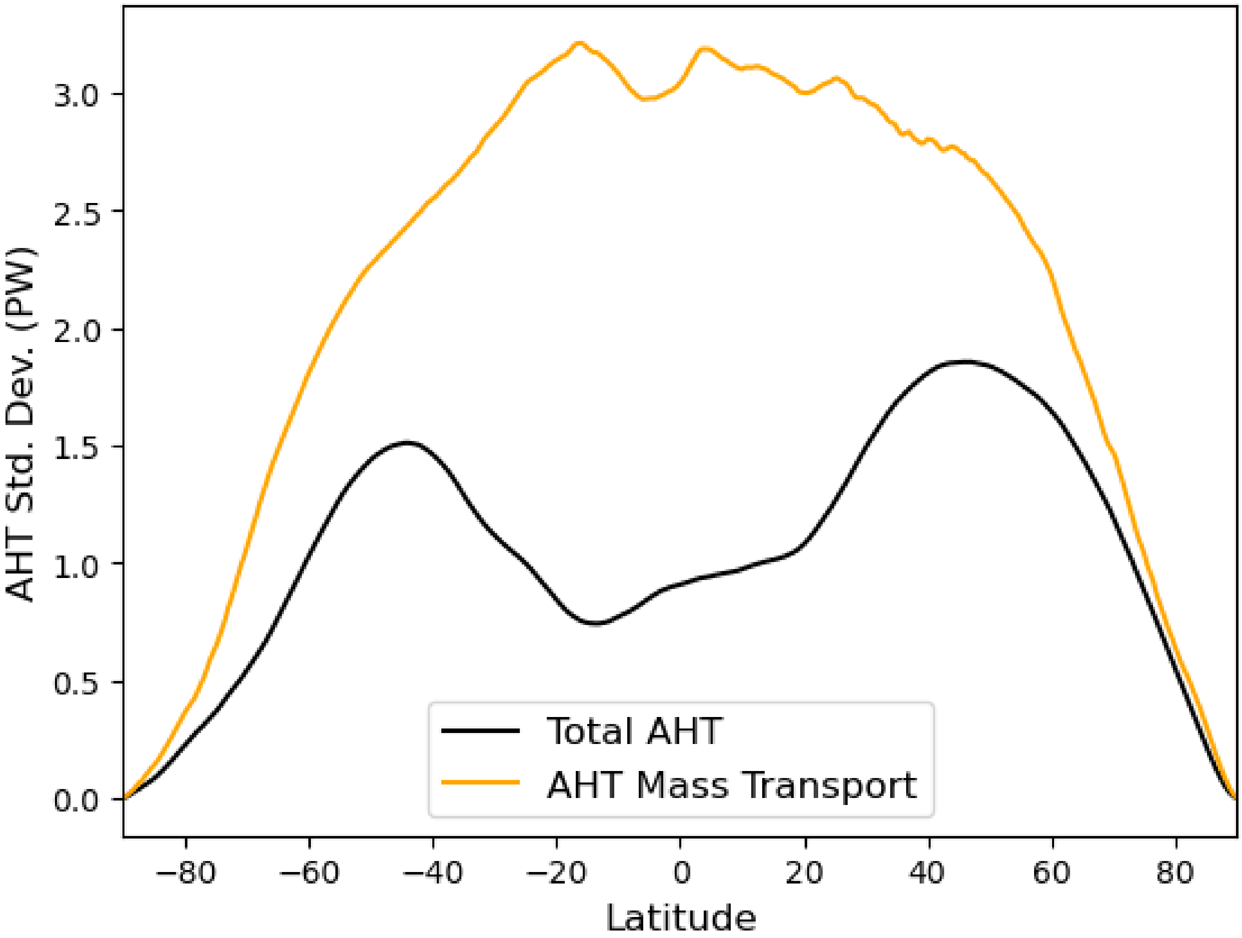

Figure 3.2: The temporal standard deviation for Total AHT (Eqn. 3.2) and the AHT Mass Transport (Eqn. 3.3). Only DJF data is included.

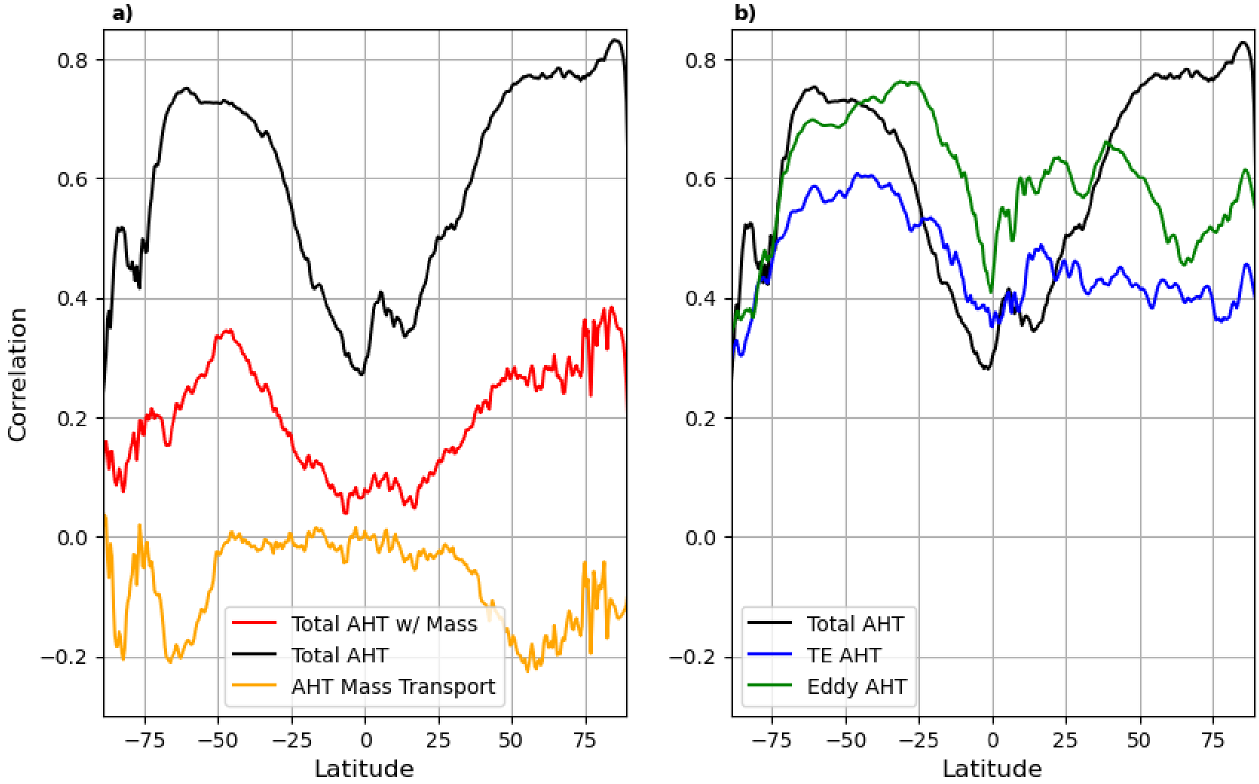

Figure 3.3: Temporal correlations between the meridional convergence of various AHT fields and the vertically-integrated MSE temporal-tendency (Eqn. 3.9). The TE AHT is calculated as in Messori and Czaja (2013, 2015). Only DJF data is included. The black lines in plots a) and b) are identical.

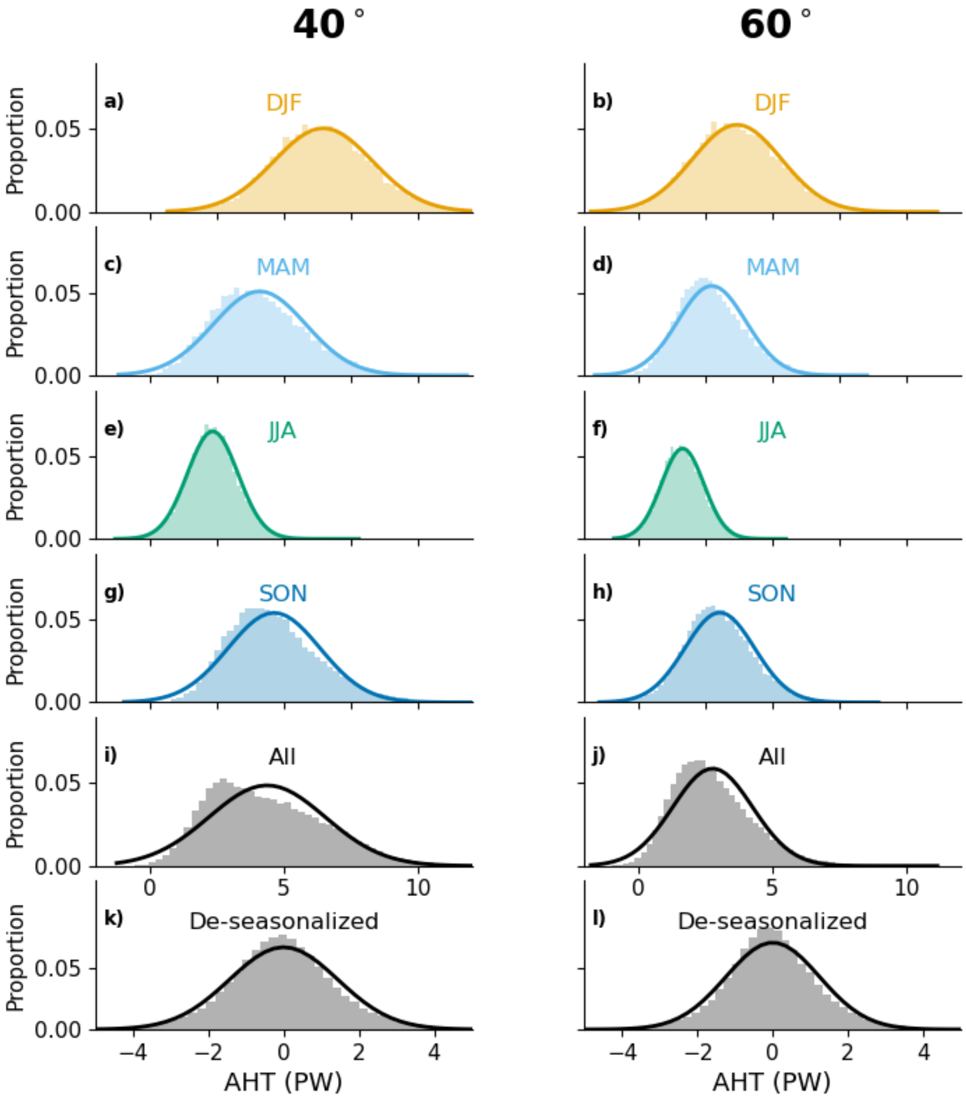

Figure 3.4: Probability density functions for total AHT broken down by season for 40°N (left column) and 60°N (right column). From top to bottom the rows correspond to total AHT PDFs for DJF, MAM, JJA, SON, all year, and all year de-seasonalized. Solid lines are Gaussian distributions with the same mean and standard of deviation as the underlying histogram. Plots a-j have the same x-axes.

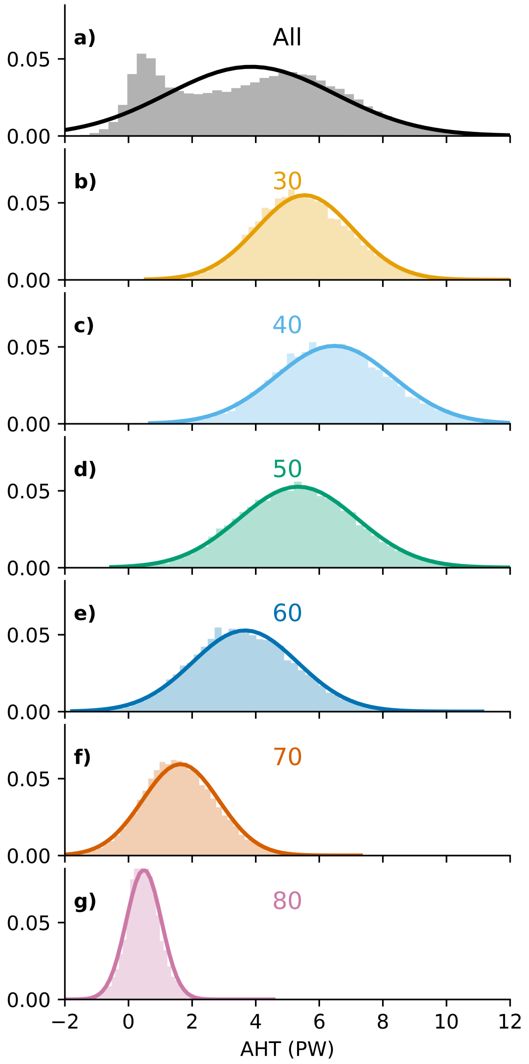

Figure 3.5: Probability density functions of total AHT during DJF for a) the aggregate of plots b) to g); b) 30°N; c) 40°N; d) 50°N; e) 60°N; f) 70°N; and g) 80°N. Solid lines are Gaussian distributions with the same mean and standard deviation as the underlying histogram.

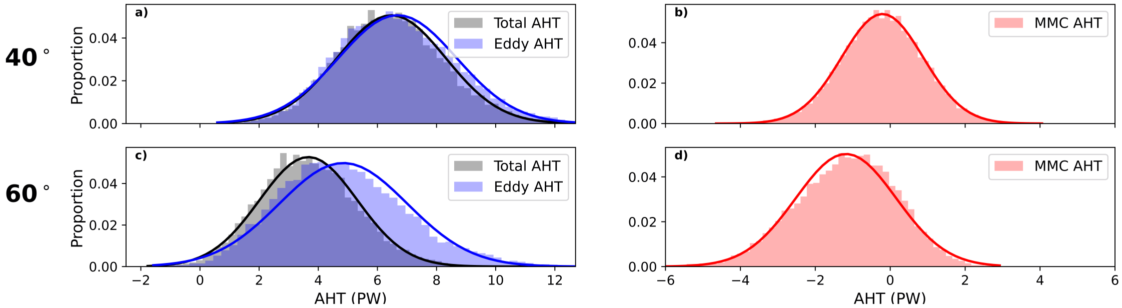

Figure 3.6: Probability density functions of: a) and c) total AHT and eddy AHT; and b) and d) MMC AHT. The top row is for 40°N and the bottom row is 60°N. Only DJF data is shown. Solid lines are Gaussian distributions with the same mean and standard deviation as the underlying histogram. Note that the distributions are nearly entirely overlapping in a) and mostly overlapping in c).

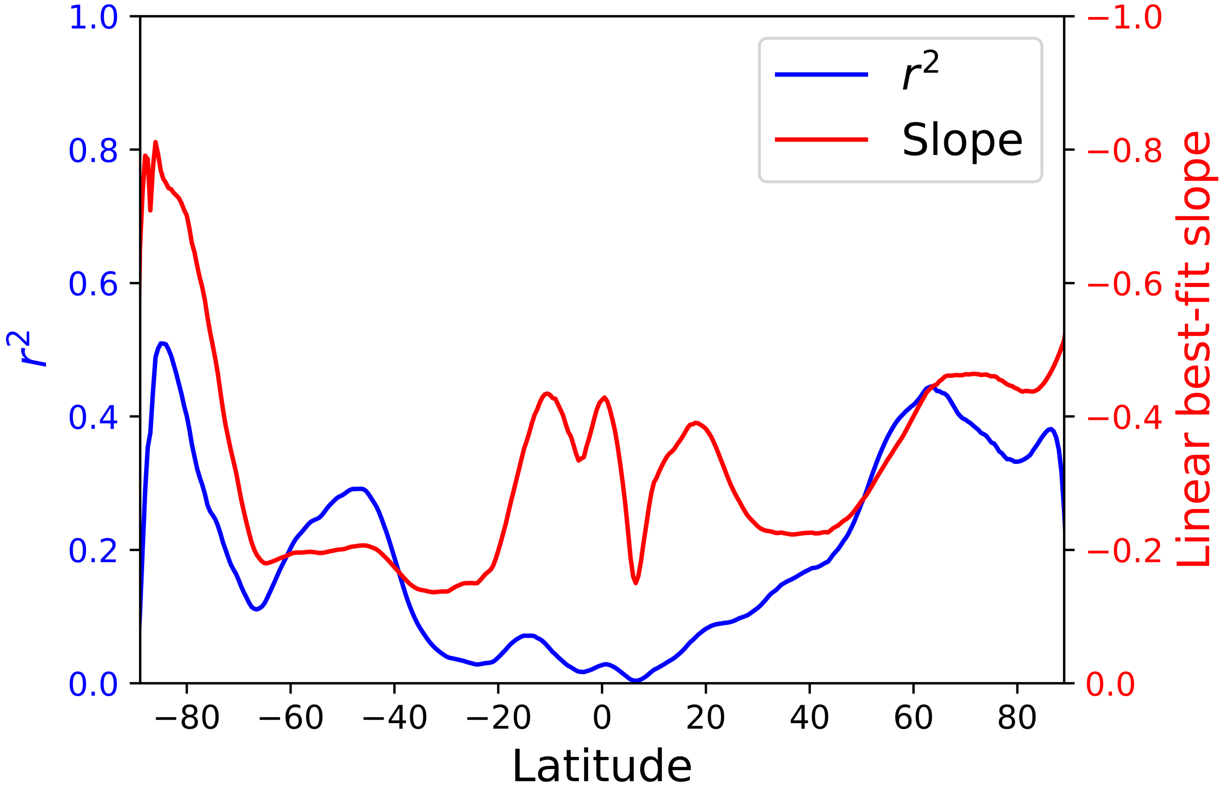

Figure 3.7: Correlations between AHT components. The red line shows the slope of the linear regression between MMC and eddy AHT and the blue line shows the r^2 values based on those slopes. Note that the y-axis for the regression slopes is flipped, so larger magnitude negative values are higher on the graph.

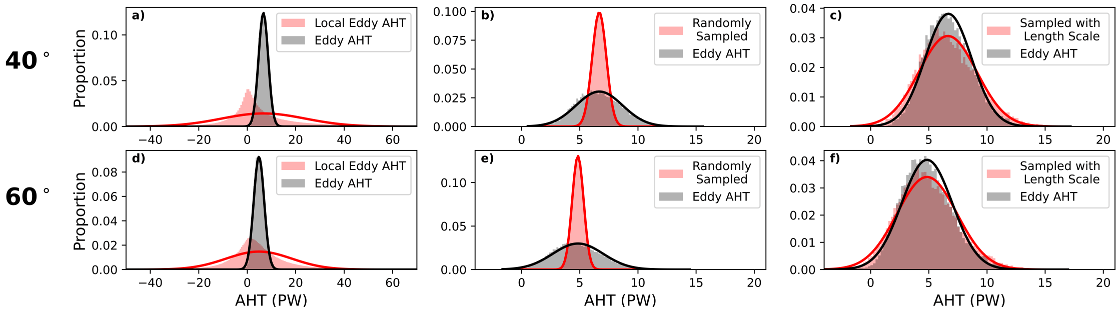

Figure 3.8: Probability density functions for fields during DJF of: a) and d) local eddy AHT and zonally integrated eddy AHT; b) and e) randomly sampled local eddy AHT and zonally integrated eddy AHT; and c) and f) randomly sampled local eddy AHT with a decorrelation length scale and zonally integrated eddy AHT. The top row is for 40°N and the bottom row is 60°N. Solid lines are Gaussian distributions with the same mean and standard deviation as the underlying histogram. Note, that in a) and d) the local eddy AHT PDFs (in red) have long narrow tails that are difficult to see.

Chapter 4

TRENDS IN ATMOSPHERIC HEAT TRANSPORT SINCE 1980

4.1 *Introduction*

Poleward atmospheric heat transport (AHT) plays a fundamental role in moderating the equator-to-pole temperature gradient and its changes under external forcing. AHT is also tightly coupled to the hydrologic cycle (e.g., Held and Soden, 2006, Pierrehumbert, 2010, Siler et al., 2018). Previous work has pointed out that AHT plays an important role in many observed climate changes including Arctic warming (e.g., Alexeev and Jackson, 2013, Hahn et al., 2021) and sea-ice loss (e.g., Woods et al., 2013, Woods and Caballero, 2016, Kapsch et al., 2013). Given the importance of AHT for Earth's climate, understanding how AHT has changed over the past several decades is an important endeavor.

Existing research has explored how specific aspects of AHT have changed over the satellite-era (since about 1980) using reanalysis datasets, coupled climate models driven by historical forcing, and atmosphere-only models driven by observed sea-surface temperatures. This previous work has used a range of methods to calculate AHT or has relied on AHT-adjacent metrics including eddy kinetic energy and mass transports (e.g., Hu et al., 2018, Chemke and Polvani, 2019, Zaplotnik et al., 2022, Chemke and Polvani, 2020). While these metrics are dynamically meaningful, our focus in this work is on the total vertically and zonally integrated AHT, which is closely connected to Earth's energy budget. We maintain a definition of AHT that can be related to the energy budget of the atmosphere while decomposing AHT into three dynamic components (e.g., Holton, 1973) to gain insight into compensation between the changes in each component. The three components contributing to AHT are conceptually summarized here:

- i) mean-meridional circulation AHT (MMC) which represents the time- and zonal-mean mass overturning circulation of the atmosphere that transports energy poleward in the tropical

Hadley cells and equatorward in the extratropical Ferrel cells.

- ii) stationary eddy AHT (SE) which represents the zonally varying time-mean circulations associated with active storm-track regions.
- iii) transient eddy AHT (TE) which represents the net heat transport by synoptic storms.

We refer to the eddy component as the sum of TE and SE and provide a more thorough mathematical breakdown of these components in Section 4.2.

There is evidence that, on a hemispheric scale and in the annual-mean, eddy heat fluxes, which are part of eddy AHT, have strengthened in the Southern Hemisphere and weakened in the Northern Hemisphere since 1980 (Chemke and Polvani, 2020). This is likely due in part to a strengthening meridional sea-surface temperature (SST) gradient in the Southern Hemisphere and a weakening SST gradient in the Northern Hemisphere (Chemke and Polvani, 2020). Both coupled and atmosphere-only models are able to capture the eddy heat flux trend in the Northern Hemisphere, while only atmosphere-only models capture the trend in the Southern Hemisphere (Chemke and Polvani, 2020). The inability of coupled models to reproduce the Southern Hemisphere eddy heat fluxes is tied to their inability to accurately capture the observed SST patterns (Liu et al., 2022, Chung et al., 2022, Dong et al., 2021). However, atmosphere-only models also fail to capture the wintertime eddy AHT trends due to inaccuracies in simulating the zonal-mean circulation (Chemke et al., 2022). This provides us with a useful starting place for exploring AHT trends, but leaves open the question of how the full-fields of TE, SE, or the MMC have changed in the annual-mean. There may also be latitudinal variations in AHT trends that averaging at the hemispheric scale, as these previous studies have done, obscures.

AHT trends in the Northern Hemisphere for each individual month have also been studied in Park and Lee (2022). This work has shown that SE trends in individual months may be driven more by changes in tropical heating, while TE trends may be driven more by meridional SST gradients. Additionally, Park and Lee (2022) show that compensation between SE and TE trends can be important in some months. However, this work primarily uses bandpass filtering to identify the TE and SE components and has focused on broad swaths of each hemisphere.

While tropical AHT has not been the primary focus of any previous work, there has been research into tropical mass-transport trends (Hu et al., 2018, Chemke and Polvani, 2019, Zaplotnik et al., 2022). This previous work found that reanalysis and models do not agree on Hadley-cell mass transport trends because of errors in the way reanalyses represents latent heating and precipitation (Hu et al., 2018, Chemke and Polvani, 2019, Zaplotnik et al., 2022). While some of the trends in Hadley-cell mass transports in reanalysis may be real, the authors of previous work recommend caution when using reanalysis in the tropics. In Section 4.3.2 of this work we investigate if these same errors impact AHT trends.

This previous work leaves open several questions. Most of the previous work (with the exception of parts of Park and Lee (2022)) focuses on individual AHT components, primarily TE. Given the extensive literature about connections between AHT components (Walker and Schneider, 2006, Branstator, 1995, Chang et al., 2002, Donohoe et al., 2020, Cox et al., 2022, Chapter 2, and Chapter 3), as well as the smoothly-varying nature of AHT with latitude (Trenberth and Stepaniak, 2003b), it seems important to consider all AHT components simultaneously, which would afford a more complete picture of how AHT has been changing. The interconnected nature of AHT components also means that assigning cause and effect can prove challenging; a change in one component will cause a change in another component. Additionally, much of this previous work has averaged AHT trends over large swaths in the mid-latitudes. While this is convenient, we find interesting AHT trend variations with latitude that this sort of averaging analysis would miss.

In this work we aim to provide a comprehensive evaluation of AHT trends in CMIP6 models and three different reanalysis datasets since the beginning of the satellite era (1980). We focus on evaluating all AHT components, and compensations between them. This provides us with a more complete picture of how AHT has changed. We also document regions where we have greater or lesser confidence in the trends based on agreement among datasets. In most regions, the trends are small compared to the climatological values.

We organize the chapter as follows. In Section 4.2 we describe the datasets used in this AHT analysis and explain our calculation methodology for AHT and the rationale behind it. In Section

4.3.1 we revisit the Southern Hemisphere mid-latitude eddy trends initially explored in Chemke and Polvani (2020) and Chemke et al. (2022) and find that there is general agreement between all three reanalysis datasets on a strengthening of the climatological TE and MMC, giving us confidence in these trends. We find that atmosphere-only models are generally able to capture the TE trends better than coupled models, and all TE trends are strongly compensated by MMC trends, such that total AHT does not change much. In Section 4.3.2 we examine tropical AHT trends and find unrealistic MMC trends in reanalysis datasets in both Northern and Southern Hemispheres. Moreover, the spread in MMC trends among reanalysis and an ensemble of models is well-explained by the trends in precipitation, allowing us to propose a constraint on MMC trends based on observed precipitation trends. In Section 4.3.3 we examine Northern Hemisphere mid-latitude AHT trends, which are generally smaller and in less agreement among datasets than trends in the Southern Hemisphere mid-latitudes leading to lower confidence in the trends. We find increases in TE around 50°N, which we link to SST changes, and mismatches between reanalysis and models north of 60°N, which we link to the varying abilities of models to accurately capture Arctic amplification. In Section 4.3.4, we examine compensation between trends in different AHT components, which generally results in smaller trends in total AHT than in individual components. We explain discrepancies between models and reanalysis, and provide explanations for the largest trends. We also direct most of our focus to annual-mean AHT trends.

4.2 *Methodology and Datasets*

One of our aims in this work is to present an analysis of AHT trends using the most state-of-the-art datasets available. We rely on reanalysis datasets as our best-estimate of AHT trends over the historical period, but note that reanalysis is imperfect. We calculate AHT for the ERA5 (Hersbach et al., 2020), JRA-55 (Kobayashi et al., 2015), and MERRA2 (Gelaro et al., 2017) reanalysis datasets as these are all regularly updated through the present-day.

We use a variety of simulations to assess how well climate models have predicted AHT trends over the satellite era. We use historical forcing simulations of 31 fully coupled climate models participating in the Coupled Model Intercomparison Project phase 6 (CMIP6; Eyring et al., 2016).

We also use 28 atmosphere-only simulations (AMIP) driven by SSTs and sea-ice concentrations prescribed to match the historical record performed as part CMIP6 (Eyring et al., 2016). The list of models and experiment names used in this work can be found in Table 4.1. We use the 'r1i1p1f1' ensemble member for all models.

We present results from 1980 through 2014 as this is the period of time in which all data sources have data available (AMIP simulations end in 2014). Using data through 2022 for sources where it is available (reanalysis and coupled models) does not substantially impact the linear trends.

In addition to 31 coupled models and 28 AMIP models, we also calculate AHT trends for three CESM2 ensembles. The first ensemble is the 100-member CESM2-LENS2 ensemble (Rodgers et al., 2021). The other two ensembles are the 10-member CESM2-GOGA ensemble, which is a global-AMIP simulation, and the 10-member CESM2-TOGA ensemble, which is a tropical-only AMIP simulation. Extratropical SSTs are set to climatology in the CESM2-TOGA simulations.

We calculate AHT for each month using the methodology described in Donohoe et al. (2020) and briefly described below. AHT is defined at each latitude (ϕ) as:

$$\mathrm{AHT}(\phi) = \frac{2\pi a\ cos(\phi)}{g} \int_0^{\overline{P_s}} \left(\underbrace{[\overline{v}]^{\dagger} [\overline{\mathrm{MSE}}]^{\dagger}}_{\text{MMC}} + \underbrace{[\overline{v^*}\ \overline{\mathrm{MSE}^*}]}_{\text{SE}} + \underbrace{\overline{[v^{*\prime}\ \mathrm{MSE}^{*\prime}]} + \overline{[v]'\ [\mathrm{MSE}]'}}_{\text{Transients}} \right) dp, \tag{4.1}$$

where v is the meridional wind, MSE is the moist-static energy, p is pressure, $\overline{P_s}$ is the climatological surface pressure, a is the radius of Earth, square brackets [ ] denote zonal averages, overbars ($\overline{\ }$) denote monthly time averages, asterisks (*) are departures from the zonal average, primes (') are departures from the monthly time average, and swords (†) are departures from the vertical average. We remove the vertical averages from both terms in the MMC to account for possible lack of mass conservation.

The MMC and SE portions of the AHT can be computed from monthly-mean data. However, the Transients portion of the AHT requires the covariance of v and MSE at 6-hourly time-scales. This presents difficulties as not all CMIP6 models make the needed 6-hourly data easily available, and even if it were available it would involve hundreds of terabytes of data. Donohoe et al. (2020)

provide a novel workaround for this problem by calculating the total AHT in each month using surface and TOA fluxes, and then backing out the Transients piece as a residual term. This avoids needing to use 6-hourly data to calculate the Transients component, but it does require trust in the surface flux data and a closed atmospheric energy budget. In models, this trust is justified, as the surface fluxes, energy budget, and atmospheric dynamics are internally consistent. However, in reanalysis the energy budget and surface flux data is less trustworthy (Chaudhuri et al., 2013, Trenberth et al., 2009, Wild et al., 2013, 2015). As a result, in reanalysis we calculate the Transients component directly using 6-hourly data. Donohoe et al. (2020) find excellent agreement between these two calculation methodologies when tested within a climate model where 6-hourly fields were available.

The Transients AHT component includes contributions from both transient eddies (first term in the Transients), and the transient overturning circulation (second term in the Transients, termed the TOC in Marshall et al. (2014)). The TOC term is generally two orders of magnitude smaller than the transient eddy term (e.g., Marshall et al., 2014, Donohoe et al., 2020). Therefore, we will refer to the Transients term as the TE, even though it does include contributions from both the TE and TOC.

All trends are calculated as the slope of the linear regression of the annual-mean AHT against time and are expressed as the trend per 40 years. While there are indications of interesting non-linear changes in AHT since 1980, exploring all of these non-linear AHT changes is beyond the scope of this work. We calculate the standard error of the linear regression coefficients to find the uncertainty in the trends, and use a two-sided Student t-test to assess if trends are significantly different from zero.

4.3 *Results*

In Figure 4.1 we show the mean AHT trends across all three reanalysis datasets, the 28 AMIP models, and the 31 coupled models. There are large MMC and TE trends over the Southern Ocean (roughly 65 to 30°S) with broad agreement between datasets. In Section 4.3.1 we explore the drivers of these Southern Ocean AHT trends. The largest magnitude AHT trends of any reanalysis dataset are found in the tropics (Fig. 4.1a,b). However, the large discrepancy between models and reanalysis in this region casts doubt on the validity of the reanalysis trends, a topic we explore in Section 4.3.2. The AHT trends in the Northern Hemisphere in Figure 4.1 show less agreement between reanalysis datasets and models than the Southern Ocean trends, leading to less confidence in trends in this region. However, we do find some common drivers of the trends across all reanalysis datasets and models in the Northern Hemisphere, which we explore in Section 4.3.3.

4.3.1 Southern Ocean AHT Trends

In the Southern Ocean, total AHT trends (Fig. 4.1a) are generally under 0.2 PW per 40 years in the ensemble means, and agree well between reanalysis datasets and models. A change in total AHT of 0.2 PW at 40°S corresponds to roughly 5% of the climatology there. The Southern Ocean trends in TE and MMC are larger in magnitude (Fig. 4.1b,c), but with differing signs between the different AHT components. The differing signs indicate compensation between AHT components, which tends to limit trends in total AHT. Specific compensation mechanisms will be elaborated on in Section 4.3.4.

The AHT components with the largest trends in the Southern Ocean are the TE (Fig. 4.1c) and the MMC (Fig. 4.1b). SE trends (Fig. 4.1d) are smaller. The mean trends in TE and MMC are the same sign among reanalysis datasets, coupled models, and AMIP models and are indicative of a strengthening of climatology, with more poleward TE associated with strengthened storms and more equatorward MMC associated with a strengthened Ferrel cell. The AMIP multi-model mean shows similar TE trends to those in reanalysis, while the coupled multi-model mean predicts smaller TE trends.

In Figure 4.2 we assess the spread in the Southern Ocean AHT trends, averaged from 40-60°S, among models and reanalysis. Overall, there is considerable intermodel spread in Southern Ocean AHT trends. Figure 4.2c shows that reanalysis has excellent agreement in TE trends between ERA5 and JRA55, with MERRA2 being an outlier showing little TE trend. AMIP models tend to estimate TE trends that are close to ERA5 and JRA55, while coupled models produce smaller magnitude TE trends. Coupled models may fail to simulate the observed TE trends because they fail to properly simulate SST trends in the Southern Ocean (Liu et al., 2022, Chung et al., 2022, Dong et al., 2021, Wills et al., 2022). Connections between meridional SST gradients and TE have a wealth of support in the literature (e.g., Held, 1999). In Figure 4.3 we plot the difference in SST trends (x-axis, the mean from 30-50°S minus the mean from 50 to 65°S) versus trends of TE (y-axis, the mean from 40 to 60°S) for all three reanalysis datasets, the coupled models, and the CESM2-LENS2. Vertical and horizontal lines show the observed SST trends (from ERSSTv5) and reanalysis estimates of the TE trends, respectively. The coupled models fail to simulate the SST trend, and therefore it is not surprising that they fail to simulate the TE trend. This is also consistent with the work of Chemke and Polvani (2020) that found AMIP models did better than coupled models at reproducing the eddy heat flux trends (rather than AHT trends as in this work) in reanalysis. We note that even among the AMIP models, which are forced by the observed SST patterns, there is still a range in TE trends (Fig. 4.3 grey violin plot).

Some AMIP models produce larger magnitude TE trends than in reanalysis, likely due to differences between reanalysis and AMIP models in SE trends. Due to compensation between SE and TE trends (explored in more detail in Section 4.3.4) a SE trend can induce an opposite-signed TE trend, separate from that caused by SST changes. In the Southern Ocean, SE trends in reanalysis are negative, while in AMIP models they are generally positive. Thus, some AMIP models may produce larger magnitude negative TE trends than reanalysis because of the combination of SST trends and TE trends. Figure 4.4 shows the relationship between trends of SE and TE in this region, confirming this possibility (i.e. an AMIP model may simulate the TE response to SST trends correctly, but then also simulates a positive SE anomaly, which leads to an additional TE response).

SE trends are smaller than TE trends, and disagree on sign between reanalysis and models (Figure 4.1d). Figure 4.2d shows that SE trends in reanalysis are outside the range of most, but not all, AMIP and coupled models and agree well among the three reanalyses. While the SE trends in this region are small compared to the TE and MMC trends, we propose two possible SE-trend sources in this region: ozone-hole induced changes and tropical-SST induced changes. Ozone depletion has led to stratospheric cooling and shifts in the stratospheric and tropospheric winds in October and November (e.g., Ramaswamy et al., 1996, Randel and Wu, 1999, Thompson and

Solomon, 2002). The ozone hole is not centered over the South Pole and is instead offset towards the Atlantic Ocean during October and November (e.g., Grytsai et al., 2007). This asymmetry induces zonally-asymmetric changes, which have led to a strengthening of the climatological eddy heat flux that makes up one part of the eddy AHT (e.g., Ivanciu et al., 2021). Differences in how models simulate stratospheric chemistry has been shown to have an impact on eddy heat fluxes in the Southern Hemisphere, with interactive chemistry models simulating changes more in-line with reanalysis and observations (Ivanciu et al., 2021). Our work finds similar results, with models that have interactive stratospheric chemistry capturing the SE trends in reanalysis during October and November better than those without interactive chemistry (Fig. 4.5). This suggests that some of the reanalysis and model SE trend discrepancy may come from some models inaccurately simulating the ozone hole and ozone-hole induced trends. While this may explain some of the reanalysis and model SE trend discrepancy, it does not explain the existence of SE trends throughout the whole year.

The second source of SE trends are likely due to tropical SST trends. This is supported by observational and theoretical work (Park and Lee, 2019, 2022, Baggett and Lee, 2017) that finds tropical heating is linked to SE in the mid- and high-latitudes. We use the ten-member CESM TOGA simulations (tropical only AMIP) and compare them against the ten-member CESM GOGA simulations (global AMIP) to assess the role of tropical SST trends in driving Southern Ocean SE trends. We find that the Southern Ocean SE trends are similar in both the CESM TOGA and CESM GOGA simulations (Fig. 4.6). The TOGA simulations use climatological SSTs in the extratropics, which suggests the tropical SST trends must be more important than extratropical SST trends for driving the Southern Ocean SE trends. It is not clear if mismatches in tropical SST trends are an additional source of the Southern Ocean SE trend mismatch between reanalysis datasets and models.

We now turn our attention to the MMC trends. Figure 4.2b shows that on average the MMC trends in the Southern Ocean are slightly larger in AMIP than in coupled models, mirroring slightly larger eddy trends (TE trends plus SE trends) in AMIP than in coupled models. Reanalysis MMC trends are mostly beyond the intermodel range for coupled models and near the edge of the range for AMIP models. We further explore compensatory changes between eddies and the MMC in Section 4.3.4.

4.3.2 Tropical AHT Trends

Previous work on tropical Hadley cell trends has cast doubt on the validity of reanalysis in this region (Hu et al., 2018, Chemke and Polvani, 2019, Zaplotnik et al., 2022). While this previous work has focused on mass transports in the tropics (rather than AHT), we present this section with the caveat that reanalysis should be interpreted with care and not treated blindly as the 'truth' for tropical AHT trends. In Figure 4.1a we can see that the largest total AHT trends in reanalysis come in the tropics, while AMIP and coupled models do not suggest large trends have occurred. Figure 4.1b shows that these trends have been primarily driven by MMC trends, which in the tropics means Hadley cell trends. Trends in the TE and SE components are much smaller.

Figure 4.7 shows the spread in MMC trends in the Southern Hemisphere (Fig. 4.7a) and Northern Hemisphere (Fig. 4.7b). In the Southern Hemisphere there is relatively good agreement among reanalyses, and all three reanalyses have MMC trends that are outside of the range of AMIP and coupled models. In the Northern Hemisphere, we see a similar picture, except that ERA5 reanalysis suggests an MMC trend near zero, which is in line with those of AMIP and coupled models.

The mismatch between models and reanalysis is also evident in the Hadley cell mass transports. In Figure 4.8 we show the mass streamfunction climatology in the black contours (averaged in time and across each group of model or reanalysis) and show the streamfunction trends in the colored shading (averaged across each group of model or reanalysis). Black stippling indicates regions where there is not strong agreement among the different models or reanalysis (for reanalysis, regions where not all reanalyses agree on the sign of the trend are stippled, while for AMIP and coupled models, regions where less than 90% of models agree on the sign of the trend are stippled). Reanalysis shows strong agreement in a strengthening of the climatological Hadley cell streamfunctions, AMIP shows a weakening of the Southern Hemisphere Hadley cell and ambiguity in the Northern Hemisphere, and coupled models show good agreement on a minor Northern Hemisphere weakening and some additional minor trends near the equator. The disconnect between reanalysis and models is still evident, just as it was for the MMC trends.

The mismatch in Hadley cell mass transports between models and reanalysis has been investigated before and the discrepancies were found to primarily come from errors that reanalysis has in its representation of latent heating and precipitation (Hu et al., 2018, Chemke and Polvani, 2019, Zaplotnik et al., 2022). As this chapter is primarily focused on AHT, rather than mass transports, we have not done a thorough Hadley-cell trend examination using the Kuo-Eliassen equation (e.g., Chemke and Polvani, 2019). However, we do briefly investigate if the spread in tropical precipitation trends can explain the trends in the MMC. In Figure 4.9 we plot the tropical precipitation trends (averaged from 10°S to 25°N) against the Southern Hemisphere MMC trends (evaluated at 15°S). While these quantities are not necessarily linearly related, we fit a linear best-fit line to the all the data points in Figure 4.9 and find an r^2 value of 0.56.

Importantly, the increase in tropical precipitation in all three sets of reanalysis is larger in magnitude than that in any climate model simulation, and is larger than that found in the more observationally constrained precipitation product GPCP (Adler et al., 2003). Furthermore, the linear relationship between tropical precipitation trends and MMC trends suggests that if models and reanalysis had similar precipitation (and latent heating) trends, they would likely have similar MMC trends.

Altogether, the combination of previous work and this work shows that tropical AHT trends should not be trusted in reanalysis. In Figure 4.9 the GPCP (Adler et al., 2003) tropical precipitation trend estimate is approximately halfway between the AMIP and coupled model means. Using our best-fit line and the GPCP precipitation estimate, we can estimate that the actual Southern Hemisphere MMC trend is approximately -0.04 PW / 40yrs. In other words, the actual tropical AHT trends since 1980 are most likely similar to the models and small in magnitude.

4.3.3 Northern Hemisphere AHT Trends

While the trends in the Southern Hemisphere mid- to high-latitudes showed one clear signal, peaking at roughly 55°S, the trends in the Northern Hemisphere mid- to high-latitudes have more latitudinal variation and less agreement between datasets. The TE and MMC trends are also smaller in magnitude than in the Southern Hemisphere (Figure 4.1). Part of this discrepancy between hemispheres is likely due to the equatorward extent of other climate trends since 1980. While Arctic amplification has been observed as a significant climate trend, it has been primarily localized north of 60°N (e.g., Gu et al., 2016). Meanwhile, the Southern Ocean SST trends have extended more equatorward, to roughly 40°S (Figure 4.10). We hypothesize that this mismatch in the equatorward extent of polar temperature changes is partially responsible for the lack of a clear hemispheric-scale trend in the Northern Hemisphere AHT, and the existence of a clear hemispheric-scale trend in the Southern Hemisphere AHT. Despite the lack of a hemispheric-scale signal in the Northern Hemisphere, there are still some interesting features, with explainable causes, in the Northern Hemisphere.

The reanalysis AHT trends in the Northern hemisphere mid- and high-latitudes with the largest magnitude are TE trends north of 60°N. Figure 4.1 shows a mismatch between reanalysis and models in the mean SE and TE trends in this region. Specifically, reanalysis has a larger decrease in TE than coupled simulations, while AMIP models show positive TE trends (Fig 4.1c). These discrepancies are likely tied to Arctic warming. Coupled models actually capture Arctic warming better than AMIP models due to a lack of change in sea-ice thickness in AMIP models (Hahn et al., 2022), but coupled CMIP6 models still generally underestimate the amount of Arctic warming since 1980 (Chylek et al., 2022). A larger amount of Arctic warming (relative to tropical warming) decreases the meridional temperature gradient, and leads to less TE. This explains why reanalysis has a larger decrease in TE trend than coupled simulations, while AMIP models actually show positive TE trends (Fig 4.1c).

Figure 4.11 shows that the TE trends in reanalysis at 65°N are outside of the interquartile range of the TE trends in AMIP and coupled models. There is considerable overlap in the TE trends of AMIP and coupled models (Fig. 4.11). However, the major theme of larger magnitude decreases in TE in reanalysis than coupled and AMIP models remains. The SE trends are in better agreement between reanalysis and models.

A second interesting feature in the Northern Hemisphere AHT trends occurs around 50°N where there is a noticeable positive TE trend and negative SE trend in reanalysis, AMIP models, and coupled models (Fig. 4.1c,d). However, Figure 4.12 shows the considerable uncertainty surrounding these trends. Two of the three reanalyses show TE trends at 50°N that are slightly greater than 0.1 PW per 40 years and near or beyond the edge of the interquartile ranges of the models, but MERRA2 shows a negative trend and AMIP and coupled models show mean trends near zero with large intermodel-spread. There is generally good agreement between reanalysis and models on the SE trend, albeit with considerable ensemble spread (Fig. 4.12b).

As discussed earlier, TE is closely connected to SSTs. Observed zonal-mean SST trends show a dip in SSTs around 50°N (Fig. 4.10). To try and diagnose if the AHT and SST trends near 50°N are related we look at trends of SSTs and TE near 50°N in the coupled models. Figure 4.13 shows the difference in SST trends between 40°N and 50°N on the x-axis against the TE trends at 50°N on the y-axis for all the coupled simulations. We also plot horizontal lines indicating the TE trends in reanalysis, a vertical line for the observed SST trend difference using ERSSTv5 data (Huang et al., 2017), and a violin plot of the AMIP TE trends at 50°N. The r^2 value of 0.41 between the SST trends and the TE trends shows a moderately strong relationship between the two fields, indicating that the increase in TE at 50°N in ERA5 and JRA55 is likely linked to SST trends. However, the TE trends are small, and the grey violin plot of AMIP TE trends in Figure 4.13 shows that even when given the observed SST pattern, models can still simulate a range of TE trends. While a thorough exploration of seasonal trends is beyond the scope of this work, we note that the TE trends at 50°N show substantial seasonal variation (Figure 4.14a,c,d) with positive trends in winter and negative trends in summer. We also find that the SE trends and SST are not well correlated (not shown), supporting previous work that found TE trends were more driven by SST changes (Park and Lee, 2022).

4.3.4 Compensation between AHT components

Trends in individual AHT components do not happen independently; a change in one AHT component can cause changes in another AHT component. As a result, it is useful to think about the AHT system holistically and consider how changes in one AHT component are connected to another.

The first major compensation occurs between eddies and the MMC. In the mid-latitudes, the eddy and MMC compensation is driven by compensation between eddies and the Ferrel cell. An intensification in eddies leads to an intensification of the MMC (via Ferrel cell intensification) (e.g., Salustri and Stone, 1983, Sasamori and Melgarejo, 1978). The MMC and eddy climatologies in the mid-latitudes are of opposite signs, so an intensification of both results in opposite signed changes. In the Southern Ocean the trends in eddies and the MMC are opposite-signed in the ensemble-means (Fig. 4.2) and show a strong negative correlation when all individual models and datasets are examined (Fig. 4.15). This same negative correlation can also be seen in the Northern Hemisphere mid-latitudes (Fig. 4.17). In both the ensemble means and in individual models the compensation is not complete. The best-fit line in Figure 4.15 shows that an eddy trend is typically compensated by an MMC trend with roughly half the magnitude. The opposite-signed changes are not only visible in the trends since 1980, but also in the interannual-variability of the eddy and MMC. In Figure 4.18 we show time-series plots of both eddies and the MMC with their trends removed. We can see that for any given year the eddy and MMC anomalies are typically opposite-signed. This demonstrates that this compensation is taking place over a range of time scales.

The second major compensation occurs between SE and TE. This compensation has theoretical justification, as SE can modify the baroclincity that TE relies on while TE and the heating associated with it can help drive SE (Branstator, 1995, Chang et al., 2002, Held et al., 2002, Inatsu et al., 2002, Kaspi and Schneider, 2013), and has been found in trends of AHT in individual months (Park and Lee, 2022). We find examples of this compensation in the Northern Hemisphere mid-latitude trends of TE and SE (Fig. 4.16). This compensation is less evident in the Southern Hemisphere, where SE plays a smaller role. Similarly to the eddy and MMC compensation, the compensation between SE and TE is not complete. The best-fit line in Figure 4.16 shows that a TE trend is, on average, compensated by an SE trend with roughly half the magnitude. In Figure 4.19 we show time-series plots of both TE and SE with their trends removed. Just as for the eddies and MMC, there are often compensating anomalies for SE and TE in any given year. The SE and TE compensation is more noticeable in the Northern Hemisphere where SE plays a larger role.

Altogether, both of these forms of compensation result in smaller trends in total AHT than in individual components in the mid- and high-latitudes. If individual AHT components are examined independently, this compensation can be missed.

4.4 *Summary and Conclusions*

This chapter analyzed AHT trends from 1980 through 2014 in three different reanalyses, 28 AMIP models, and 31 coupled models. We found strong agreement among datasets on a strengthening of the climatological TE and MMC in the Southern Ocean. The magnitude of the reanalysis TE trends in the Southern Ocean are better captured by AMIP than coupled models due to the difficulty coupled models have of correctly simulating SST trends in that region. These TE trends in the Southern Ocean are well compensated by opposite-signed MMC trends, resulting in smaller magnitude total AHT trends than might be suggested from TE trends alone. In the tropics, reanalysis shows large MMC trends that we find are unreliable and related to unreasonable precipitation trends, in agreement with previous work that investigated Hadley cell mass transports (Hu et al., 2018, Chemke and Polvani, 2019, Zaplotnik et al., 2022). In the Northern Hemisphere, we find trends that are less uniform, with disagreements on the sign of trends between reanalysis and models at many latitudes.

While trends differed region-to-region, a few overarching principles emerged. The first is that compensation between dynamic AHT components is important to consider when thinking about AHT trends. No AHT component will change independently, with a change in one often creating a change in another. A second principle is the difficulty in identifying robust trends over such a short time period. In many regions the trends have yet to rise above natural variability, and even in regions where they do there is often disagreement between models and reanalysis, or even disagreement among reanalyses. This disagreement among reanalyses is a difficult problem to resolve. In the tropics we were able to build upon previous work (Hu et al., 2018, Chemke and Polvani, 2019, Zaplotnik et al., 2022) and use precipitation trends as a way to evaluate reanalysis AHT trends in that region. However, validating each reanalysis product in every region of interest is beyond the scope of this work. Thus, we are left assuming that, outside of the tropics, each reanalysis is an

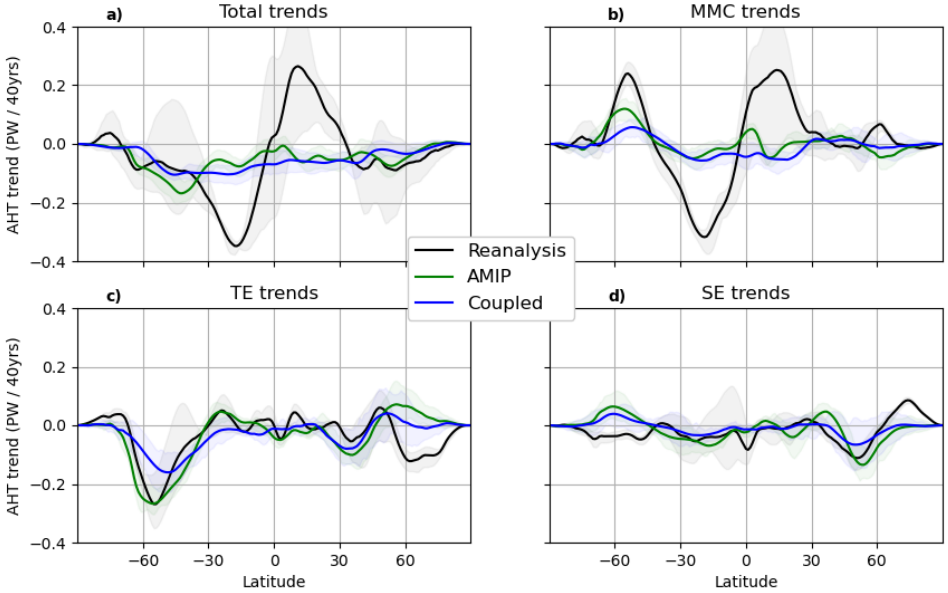

Figure 4.1: Mean AHT trends for the three reanalyses, 28 AMIP models, and 31 coupled models for the a) total AHT trends, b) MMC trends, c) TE trends, and d) SE trends. The shading around the AMIP and coupled lines shows the interquartile range, while the shading around the reanalysis lines shows the range across the three reanalyses.

equally likely representation of the climate since 1980. A third major principle is one of caution to not take reanalysis at face value. The tropics are a region where we find that reanalysis fails to simulate reasonable AHT trends. While we don't find any other regions where reanalysis is clearly inaccurate, it is worth keeping in mind that biases in reanalysis can influence fields in ways that may not immediately be obvious. Given the close connections that AHT has to the hydrologic cycle and to meridional temperature gradients, it is important to monitor AHT trends over the coming decades.

Model Name	Coupled Model	AMIP Model	Interactive Chemistry

AWI-CM-1-1-MR	Y	N	N
AWI-ESM-1-1-LR	Y	N	N
BCC-CSM2-MR	Y	Y	N
BCC-ESM1	Y	Y	N
CAS-ESM2-0	Y	Y	N
CESM2-WACCM	N	Y	Y
CESM2-WACCM-FV2	Y	Y	Y
CMCC-CM2-HR4	Y	Y	N
CMCC-CM2-SR5	Y	Y	N
CMCC-ESM2	Y	N	N
CanESM5	Y	Y	N
CanESM5-1	Y	N	N
E3SM-1-0	Y	Y	Y
EC-Earth3	N	Y	N
EC-Earth3-AerChem	N	Y	N
EC-Earth3-CC	Y	Y	N
EC-Earth3-Veg	Y	Y	N
FGOALS-f3-L	Y	Y	N
FIO-ESM-2-0	Y	N	N
GISS-E2-1-G	Y	Y	Y
GISS-E2-1-H	Y	N	Y
GISS-E2-2-G	Y	N	Y
IITM-ESM	Y	Y	N
INM-CM4-8	Y	Y	N
INM-CM5-0	Y	Y	N
IPSL-CM6A-LR	Y	Y	N

IPSL-CM6A-LR-INCA	Y	N	N
MIROC6	Y	N	N
MPI-ESM-1-2-HAM	Y	Y	N
MPI-ESM1-2-HR	Y	Y	N
MPI-ESM1-2-LR	Y	Y	N
MRI-ESM2-0	N	Y	Y
NESM3	Y	Y	N
NorCPM1	N	Y	N
NorESM2-LM	Y	Y	N
NorESM2-MM	Y	N	N
TaiESM1	N	Y	N

Table 4.1: AMIP and coupled models used in this chapter. Y denotes the model is used or that it has interactive stratospheric chemistry, and N denotes the model was not used or does not have interactive stratospheric chemistry.

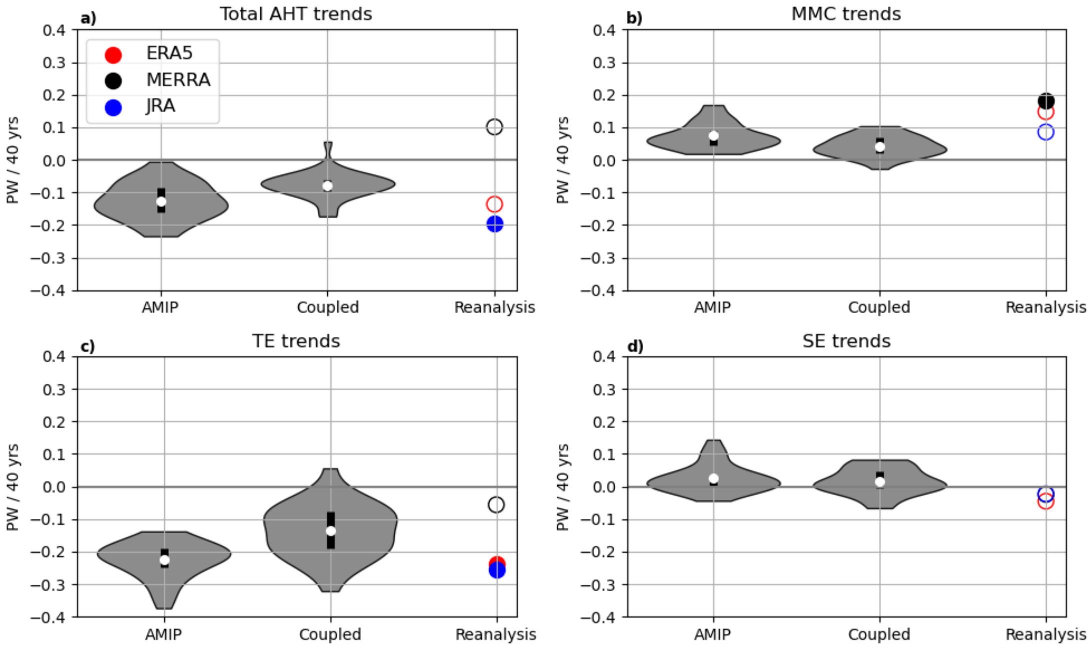

Figure 4.2: Trends averaged from 40-60°S for a) total AHT trends, b) MMC trends, c) TE trends, and d) SE trends. For AMIP and coupled models the violin plots show the ensemble distributions, where the width of the shading indicates probability density, the thick black lines indicate the interquartile range, and the white dots indicate the mean value. For reanalysis, filled circles denote trends that are statistically different from zero at the 95% confidence level, while open circles denote trends that are not.

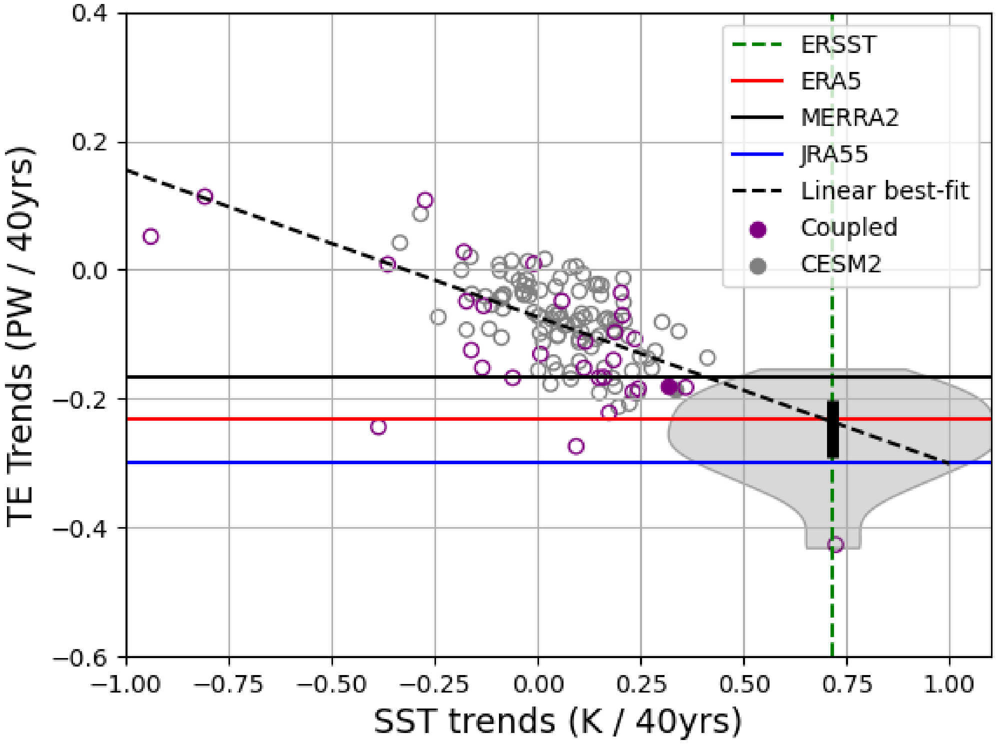

Figure 4.3: Trends of SST differences (x-axis, the mean from 30-50°S minus the mean from 50 to 65°S) versus trends of TE (y-axis, the mean from 40 to 60°S) for all three reanalyses, the coupled models, and the CESM2-LENS2. The dashed green vertical line is the ERSSTv5 SST trend estimate, the horizontal colored lines are the TE trend estimates from each reanalysis, and the dashed diagonal line is the linear best-fit line. Filled circles denote trends that are statistically different from zero at the 95% confidence level, while open circles denote trends that are not. The grey shading of the violin plot shows the AMIP ensemble TE trend values, where the width of the shading indicates probability density and the thick black line indicates the interquartile range.

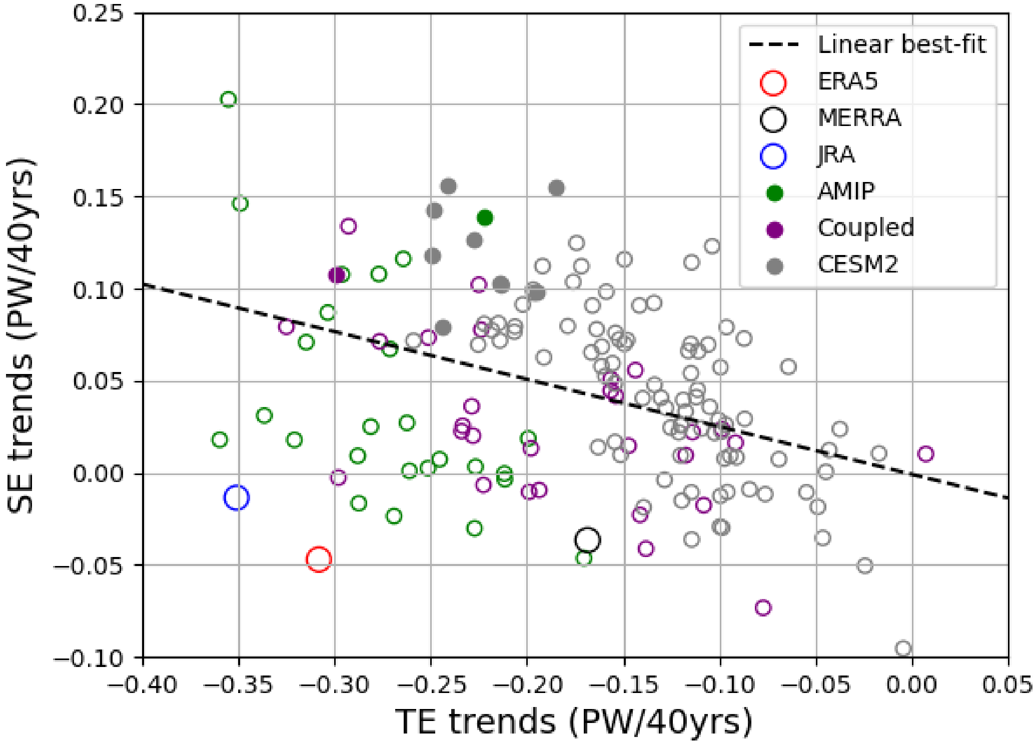

Figure 4.4: Trends of TE (x-axis) versus trends of SE (y-axis) for the three reanalyses, all the AMIP and coupled models, and for the CESM2-LENS2 ensemble. The latitudes for each point are found by finding the latitude within the 40-60°S range with the minimum TE trend. The SE trend value is selected at that same latitude. Filled circles denote models that have both TE and SE trends that are statistically different from zero at the 95% confidence level, while open circles denote models that do not.

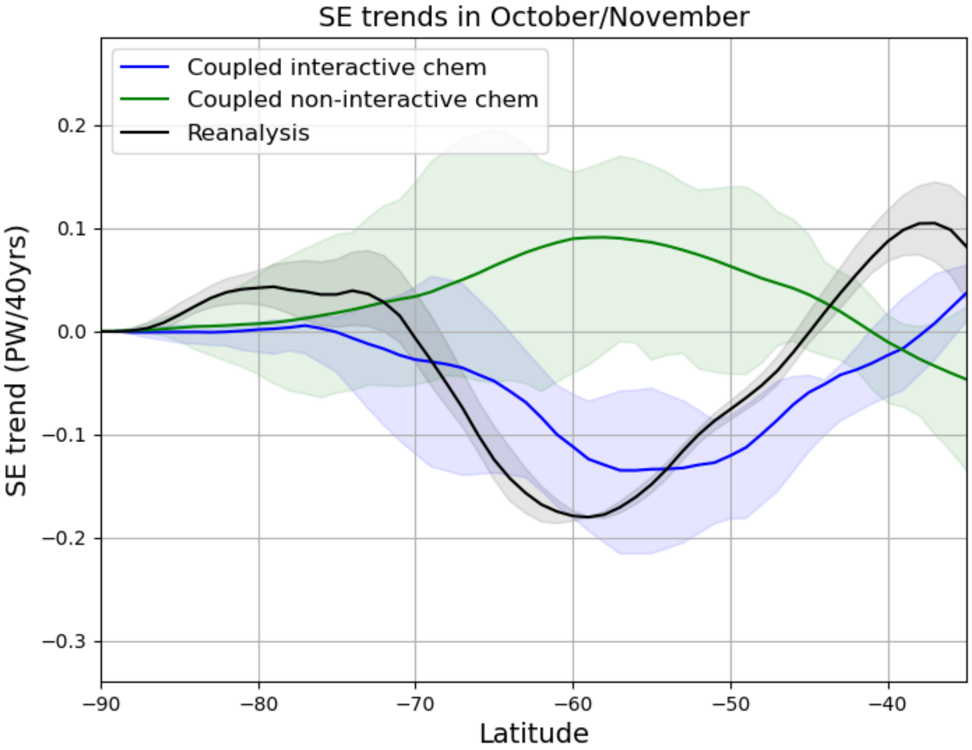

Figure 4.5: SE trends in October and November for the mean of the reanalyses, the coupled models with interactive stratospheric chemistry, and the coupled models without the interactive stratospheric chemistry. See Table 4.1 for a list of models with interactive stratospheric chemistry. The shading around the model lines shows the interquartile range, while the shading around the reanalysis lines shows the range across the three reanalyses.

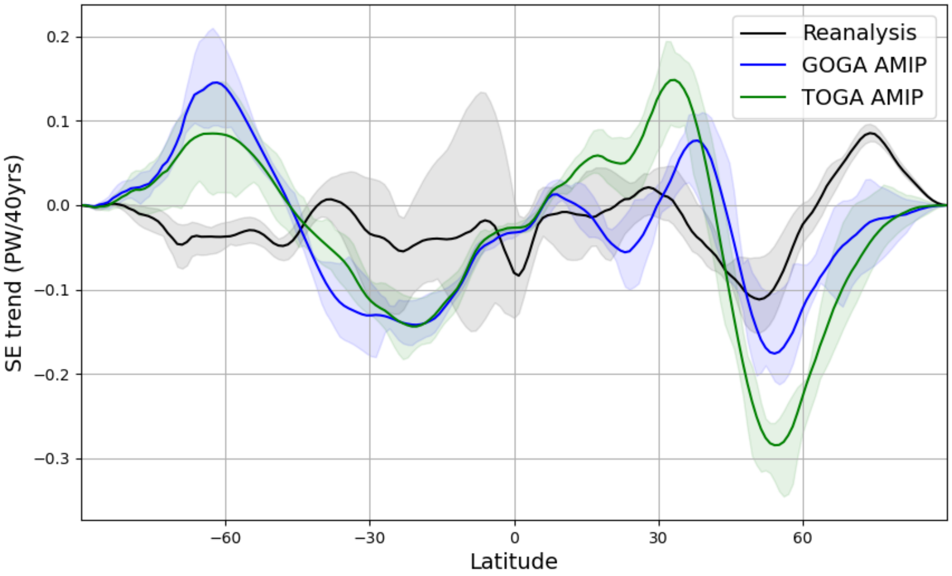

Figure 4.6: Annual-mean SE trends for the mean of the reanalyses, the 10-member CESM TOGA ensemble, and the 10-member CESM GOGA ensemble. The shading around the model lines shows the interquartile range, while the shading around the reanalysis lines shows the range across the three reanalyses.

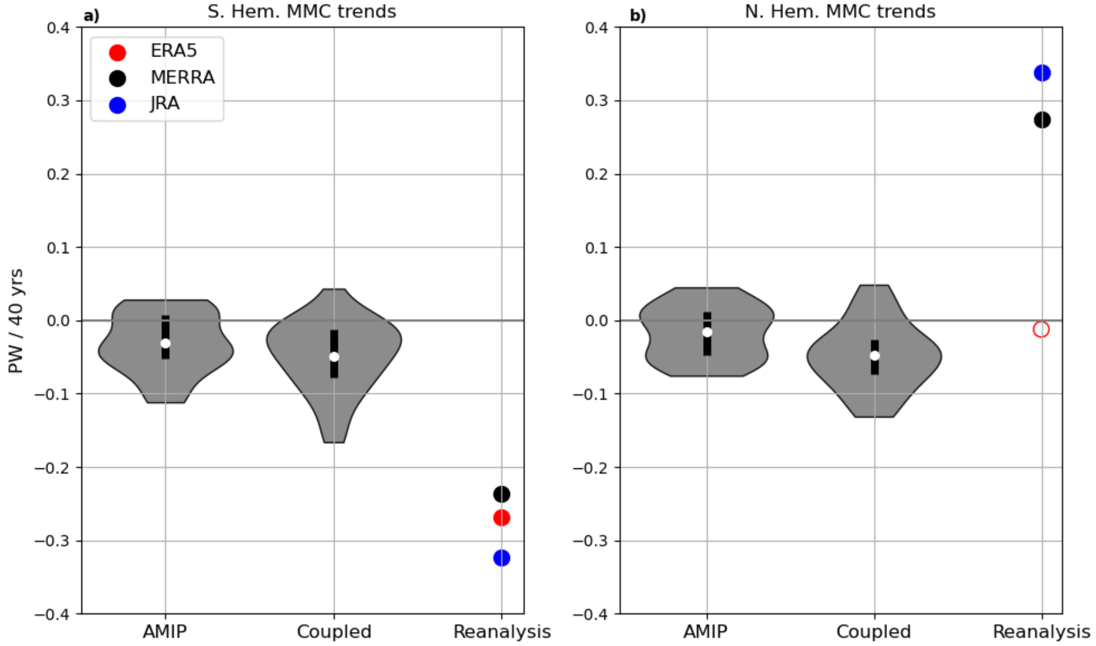

Figure 4.7: MMC trends in the a) Southern Hemisphere tropics averaged from 20-25 °S and b) in the Northern Hemisphere tropics averaged from 10-25 °N. For AMIP and coupled models the violin plots show the ensemble distributions, where the width of the shading indicates probability density, the thick black lines indicate the interquartile range, and the white dots indicate the mean value. For reanalysis, filled circles denote trends that are statistically different from zero at the 95% confidence level, while open circles denote trends that are not.

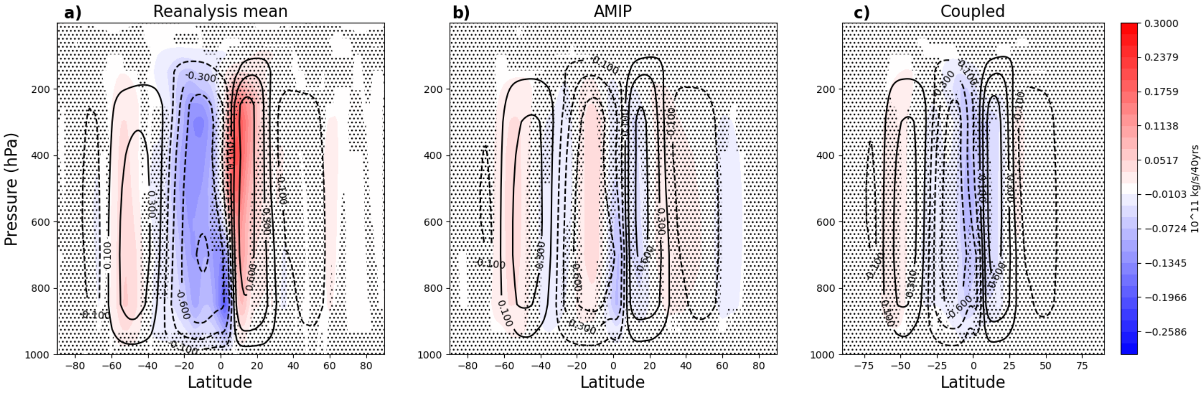

Figure 4.8: Mass overturning stramfunctions for a) the reanalyses mean, b) the AMIP model mean, and c) the coupled model mean. Black contours are the climatological values (contour intervals are labeled and are in units of 10^{11} kg s^{-1}) and the colored shading shows the 40 year linear trend. Stippling indicates regions where the three reanalyses do not agree on the sign of the trend or, for the AMIP and coupled models, regions where less than 90% of the models agree on the sign of the trend.

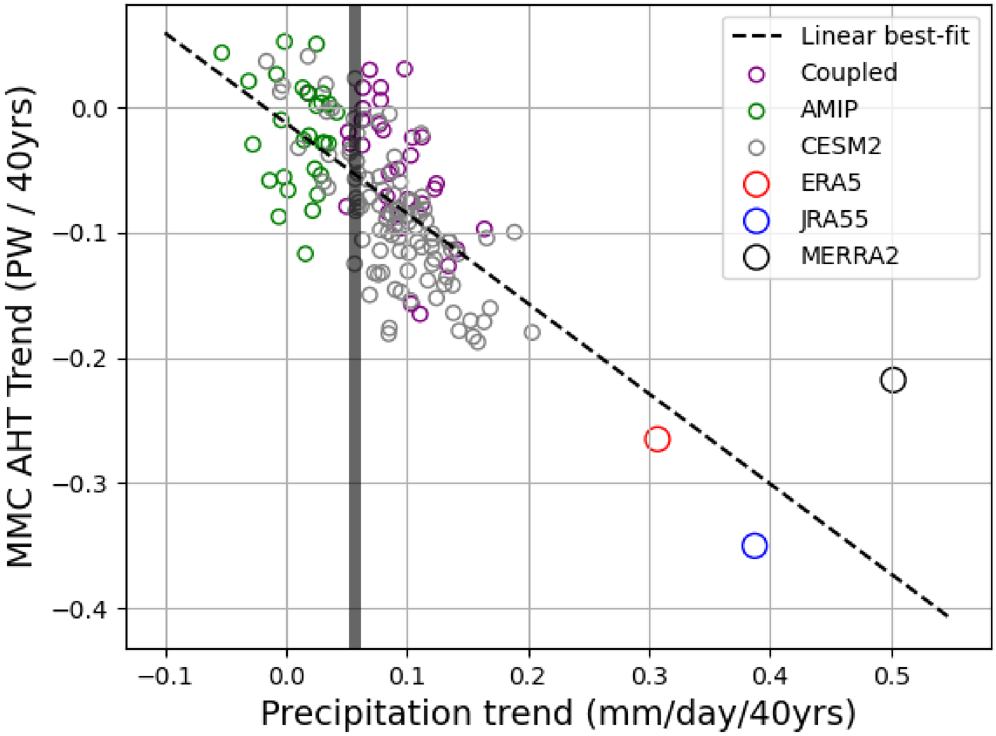

Figure 4.9: Tropical precipitation trends (x-axis, averaged from 10°S to 25°N) and the Southern Hemisphere tropics MMC trends (y-axis, evaluated at 15°S). The vertical black line is the GPCP precipitation trend (Adler et al., 2003).

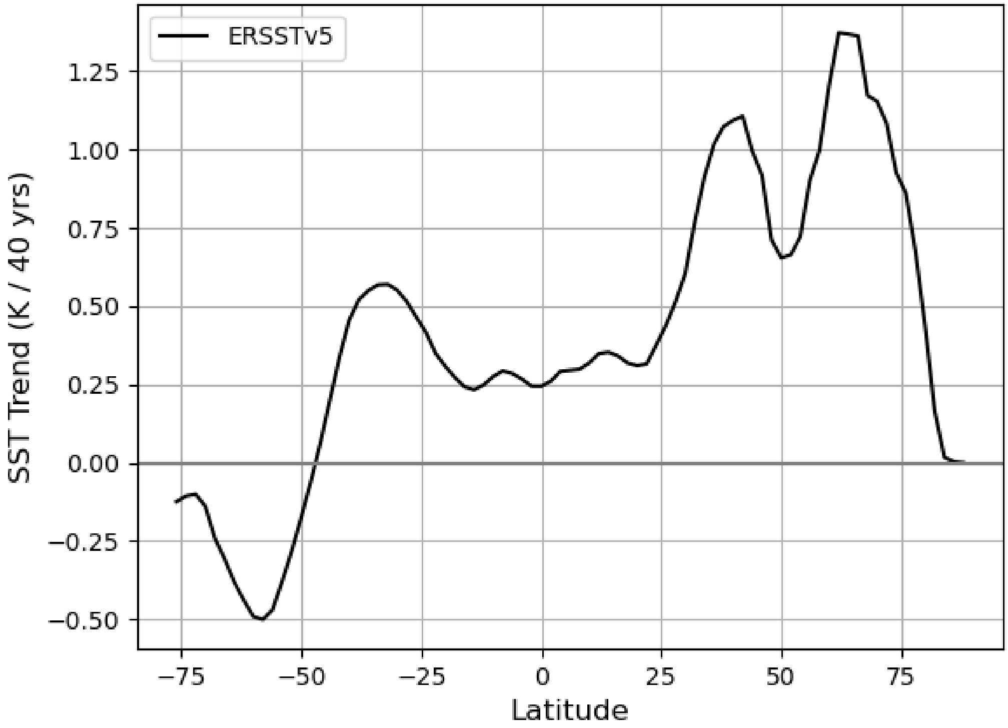

Figure 4.10: Zonal-mean SST trends from ERSSTv5 (Huang et al., 2017).

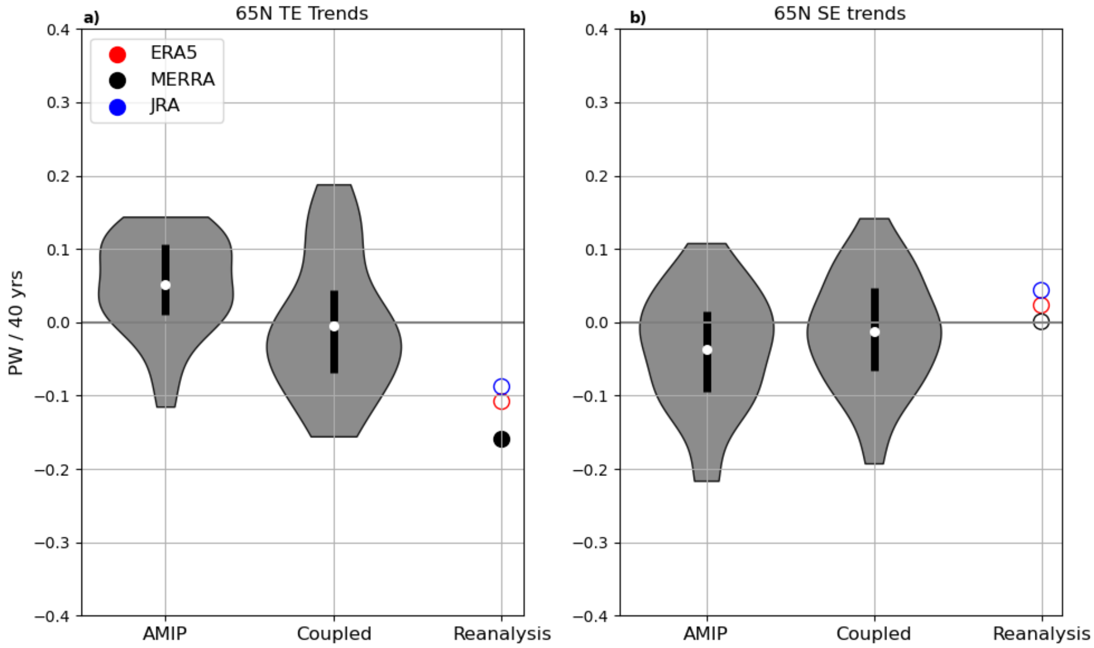

Figure 4.11: Trends at 65°N for a) TE trends, and b) SE trends for the AMIP models, coupled models, and reanalyses. For AMIP and coupled models the violin plots show the ensemble distributions, where the width of the shading indicates probability density, the thick black lines indicate the interquartile range, and the white dots indicate the mean value. For reanalysis, filled circles denote trends that are statistically different from zero at the 95% confidence level, while open circles denote trends that are not.

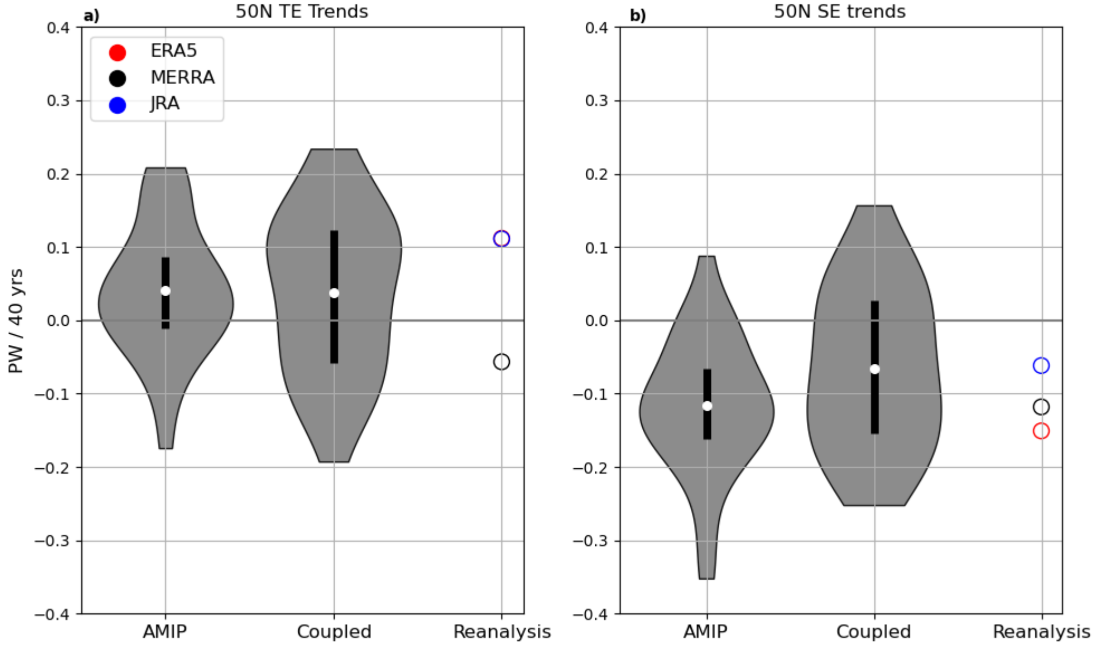

Figure 4.12: Trends at 50°N for a) TE trends, and b) SE trends for the AMIP models, coupled models, and reanalyses. For AMIP and coupled models the violin plots show the ensemble distributions, where the width of the shading indicates probability density, the thick black lines indicate the interquartile range, and the white dots indicate the mean value. For reanalysis, filled circles denote trends that are statistically different from zero at the 95% confidence level, while open circles denote trends that are not. Note that the ERA5 and JRA55 reanalyses are almost identical in a).

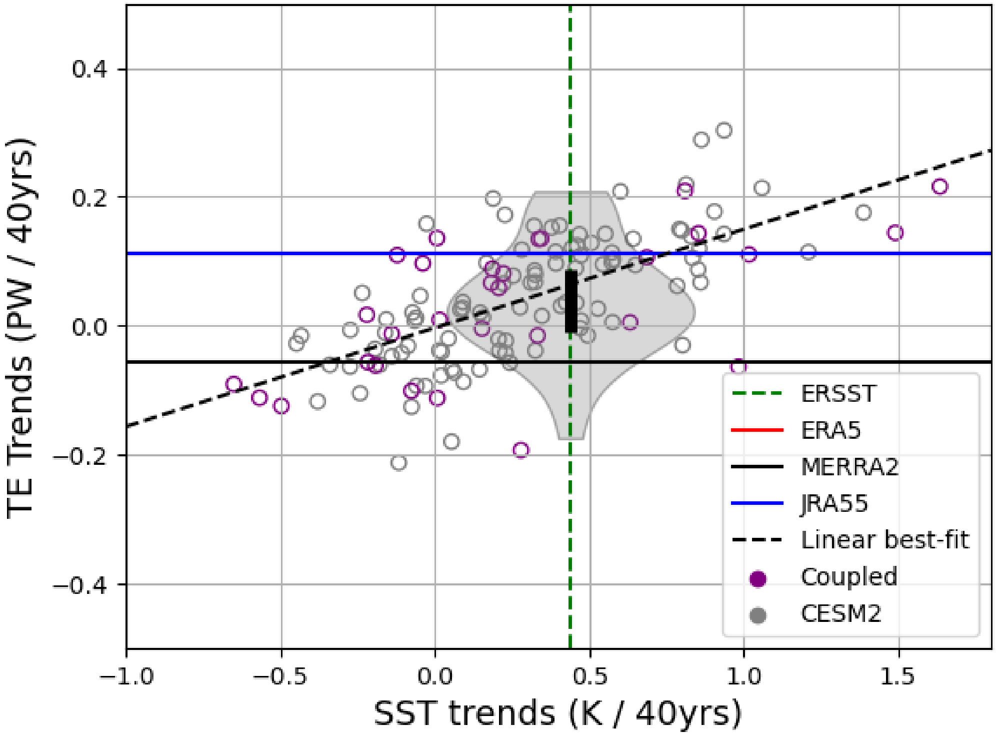

Figure 4.13: Differences in SST trends between 40°N and 50°N (x-axis) and the TE trends at 50°N (y-axis). The vertical dashed green line is the ERSSTv5 (Huang et al., 2017) estimate of the SST trends difference and the horizontal lines are the TE trends from reanalysis. Note that the ERA5 and JRA55 lines are mostly overlapping. Open circles denote models that have one or both of SST and TE trends that are not statistically different from zero at the 95% confidence level. The grey shading of the violin plot shows the AMIP ensemble TE trend values, where the width of the shading indicates probability density and the thick black lines indicate the interquartile range.

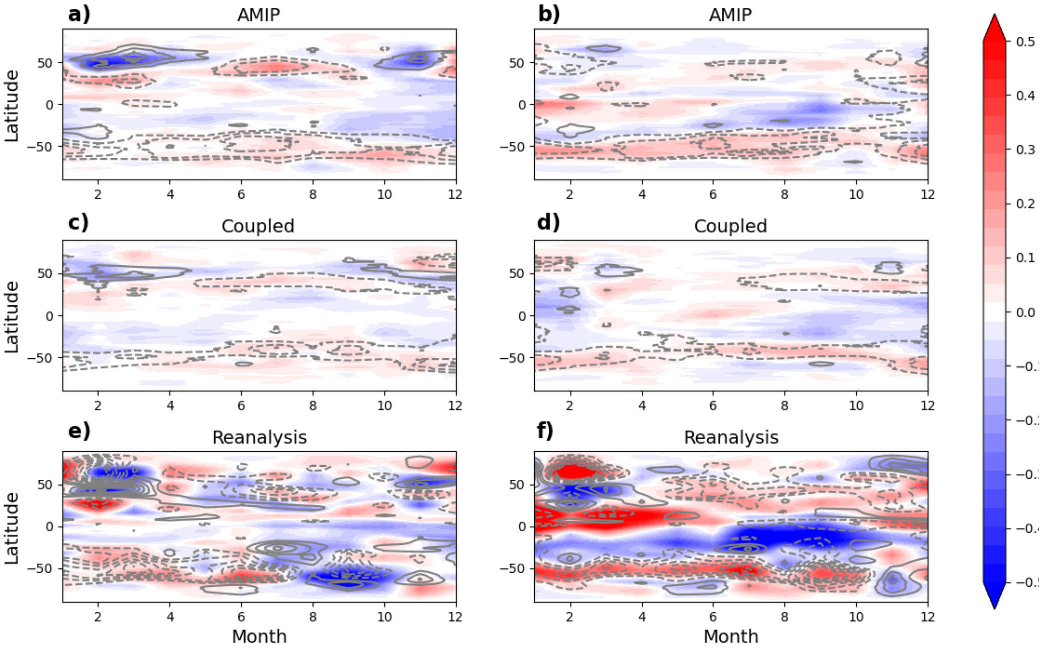

Figure 4.14: Trends for AHT components in each month averaged across the AMIP models (top row, plots a and b) , the coupled models (middle row, plots c and d) and the reanalyses (bottom row, plots e and f). The lefthand column (plots a, c, and e) show TE trends in the black contours and SE trends in the colored shading, while the righthand column (plots b, d, and f) show the eddy trends in the black contours, and the MMC trends in the colored shading. The black contour contour interval is 0.1 PW / 40yrs.

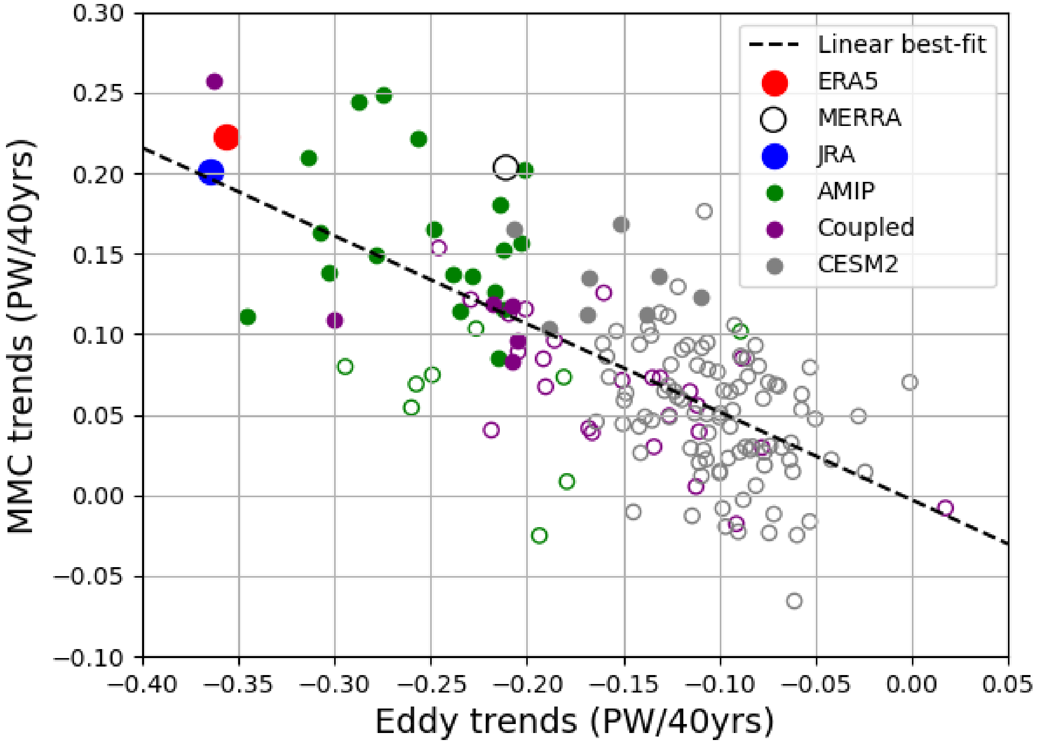

Figure 4.15: Trends of eddies (x-axis) versus trends of the MMC (y-axis) for the three reanalyses, all the AMIP and coupled models, and for the CESM2-LENS2 ensemble. The latitudes for each point are found by finding the latitude within the 40-60°S range with the minimum eddy trend. The MMC trend value is selected at that same latitude. Filled circles denote models that have both eddy and MMC trends that are statistically different from zero at the 95% confidence level, while open circles denote models that do not.

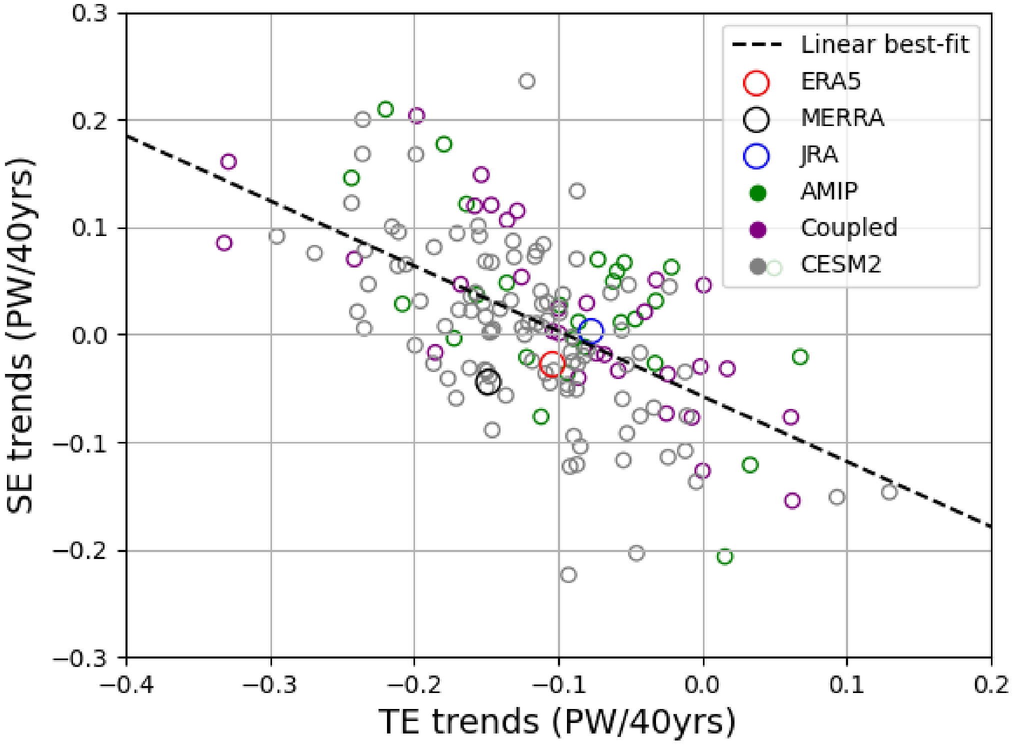

Figure 4.16: Trends of TE (x-axis) and SE (y-axis) for all 3 reanalyses, all the AMIP and coupled models, and for the CESM2-LENS2 ensemble. The latitudes for each point are found by finding the latitude within the 40-60°N range with the minimum TE trend. The SE trend value is selected as the value at that same latitude. Filled circles denote models that have both TE and SE trends that are statistically different from zero at the 95% confidence level, while open circles denote trends that are not.

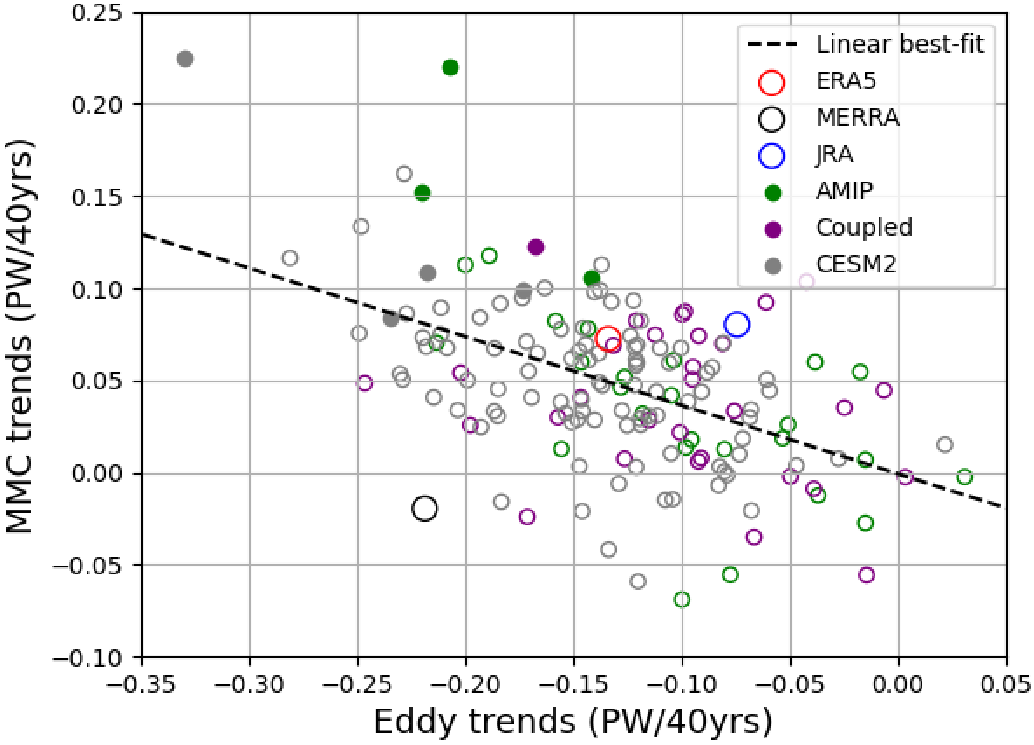

Figure 4.17: Trends of eddy (x-axis) and MMC (y-axis) for all reanalyses, all the AMIP and coupled models, and for the CESM2-LENS2 ensemble. The latitudes for each point are found by finding the latitude within the 40-60°N range with the minimum eddy trend. The MMC trend value is selected at that same latitude. Filled circles denote models that have both eddy and MMC trends that are statistically different from zero at the 95% confidence level, while open circles denote trends that are not.

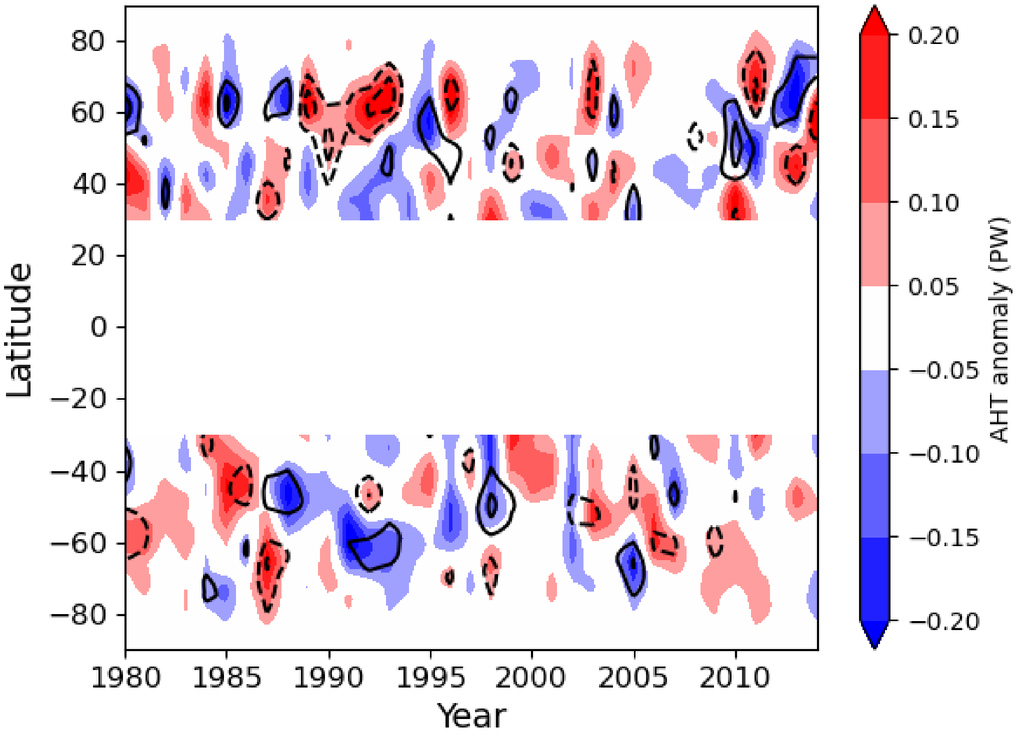

Figure 4.18: Time-anomalies in annual-mean eddy (colors) and MMC (black contours). The black contour interval is 0.1 PW. The linear temporal trend is removed from each latitude before finding the anomalies. The area between 30°S and 30°N is masked.

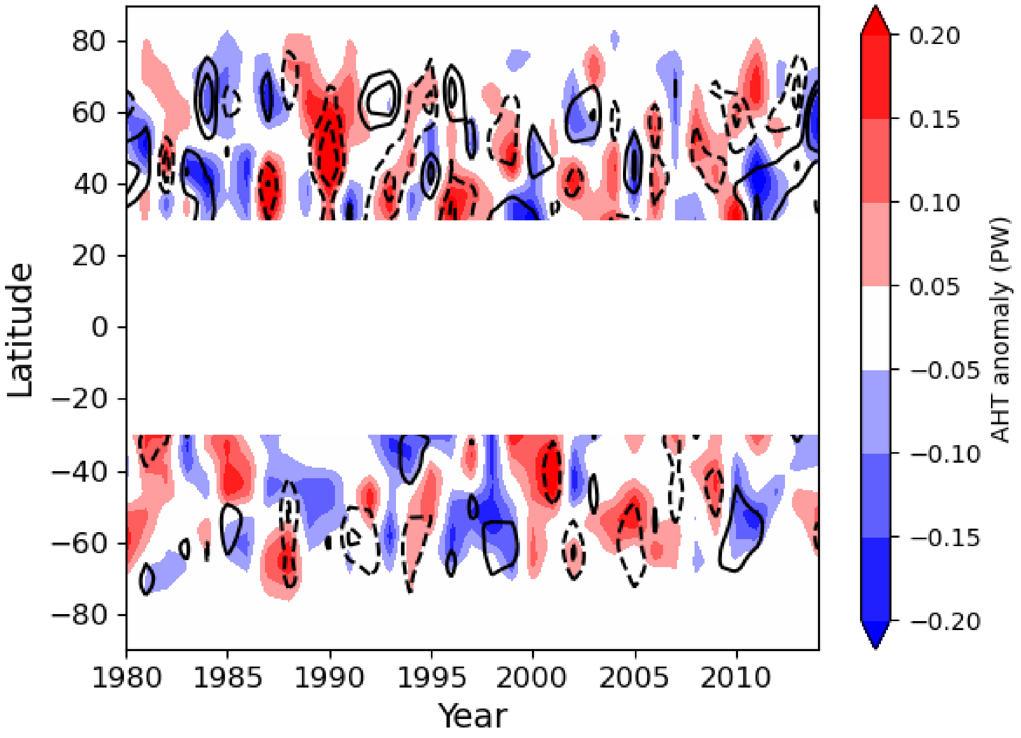

Figure 4.19: Time-anomalies in annual-mean TE (colors) and SE (black contours). The black contour interval is 0.1 PW. The linear temporal trend is removed from each latitude before finding the anomalies. The area between 30°S and 30°N is masked.

Chapter 5

CONCLUSIONS

This dissertation has presented research I've done on AHT over the past several years. In Chapter 1, I introduced the concept of AHT, discussed what AHT is, why it's an important part of Earth's climate to understand, and framed some considerations about the variability of total AHT.

In Chapter 2, I explored the role of orography in AHT. Using an idealized modeling setup I introduced large mountain ranges into the mid-latitudes of both hemispheres. Despite large disruptions in mid-latitude circulation, total AHT was largely invariant. The invariant AHT occurred because of strong compensation. While the specific mechanisms of compensation varied depending on the model configuration and perspective on AHT that was used, this work showed the flexible nature of AHT to adjust to a wide array of conditions, while maintaining a similar total AHT. This helps provide context about why total AHT is similar between the Northern and Southern Hemispheres in our current climate, and is nearly invariant when comparing simulations of the Last Glacial Maximum with today's climate.

Chapter 3 shifts focus away from the idealized modeling world and to our present day climate. I explored the temporal variability of AHT by calculating AHT in ERA5 reanalysis at 6-hourly temporal resolution. In contrast to some previous work, I found that AHT is nearly Gaussian in its temporal distribution, with a limited role for extreme events. This provides support for the idea that understanding the mean and variability of AHT is likely more important than understanding the unique drivers of extreme events. I also found that the eddy and MMC AHT components are negatively correlated on 6-hourly time scales.

Given what I learned in Chapter 3, that understanding what sets the mean of AHT may be more important than understanding what controls individual AHT events, in Chapter 4 I calculated linear-trends in annual-mean AHT since 1980. I calculated AHT trends in three different reanalyses, 31 coupled CMIP6 models, 28 AMIP models, and three different CESM2 ensembles. One major takeaway is that in many parts of the globe 40 years is too short a time period to see clear signals emerge due to natural variability. I also found strong compensation in trends between different dynamic components, much in the same way compensation showed up when orography was introduced in Chapter 2.

As alluded to in Chapter 1, compensation emerges as a common principle in a wide-range of time scales. At 6-hourly time scales eddy and MMC AHT are negatively correlated, such that the variance in total AHT is smaller than that of eddy or MMC AHT alone. Trends in AHT since 1980 show similar compensation between eddy and MMC AHT as well as between TE and SE AHT. While these different examples of compensation occur over very different time scales, they appear to share similar dynamical mechanisms for how the compensation occurs (see Section 2.1 for a detailed overview of different compensation mechanisms). While the mechanisms for compensation may be similar, the effectiveness of the compensation does vary with time scale. Effectiveness is referring to the degree of compensation. A 100% compensation would be components changing in a perfect one-to-one ratio, albeit with opposite signs. A 50% compensation would mean that a change in one component was countered by a change in another component with half the magnitue of the original change. At longer time scales (multi-decadal trends) the compensation can in some cases be close to one-to-one for individual models and is often above 70%. Similarly effective compensation is seen in the climatological anomalies when orography is added, with compensation at many latitudes being nearly one-to-one. On the other hand, at 6-hourly time scales the compensation peaks near 40%. This range in the effectiveness of compensation is likely due to AHT at shorter time scales being partially used to heat or cool the atmospheric column. As shown in Chapter 3, correlations between meridional AHT convergence and column energy tendency are high, near 0.8 in the mid-latitudes. Thus, at shorter time scales compensation between AHT components is less effective because much of what AHT is doing is heating of the atmospheric column, rather than creating a compensatory effect in a different AHT component. Over longer time scales, the heating of the atmospheric column is negligible, and the compensation efficiency is closer to 100%. Radiative fluxes and surface fluxes may also play a role at shorter time scales.

In Chapter 1 I introduced three perspectives on AHT: *radiative*, *dynamic*, and *diffusive*. Both the *radiative* and *diffusive* perspectives offer straightforward ways to understand why total AHT is smoothly varying with latitude (see Chapter 1). The strong tendency towards compensation that I've found in this work helps to provide and understanding for why total AHT varies smoothly with latitude under the *dynamic* perspective.

Looking towards the future, there are several research pathways to improve our understanding of AHT, and specifically the role of compensation in AHT. It is worth examining additional details about how the compensation occurs over different time scales and if the mechanisms of compensation are consistent across those time scales, as initial results suggest. This could be done using all three of the AHT perspectives, dynamic, energetic, and diffusive. At least initially, it may be easiest to explore compensation on different time scales in a model, where the atmospheric energy budget should be closer to being closed than in reanalysis. A concept closely related to AHT compensation is the smoothness with which AHT varies with latitude. The limits of this smoothness could be explored by adding small spatial elements with large magnitude into an idealized modeling setup. These elements could include very large mountains or large atmosphere-ocean heat fluxes. The hope is that by making such elements very large in magnitude, it will be possible to probe the limits of AHT smoothness. More broadly, it will be beneficial if all future work on AHT looks at AHT holistically, and accounts for possible compensation between components. This will help provide a richer understanding of how AHT varies, or does not vary, in different scenarios.

BIBLIOGRAPHY

Adler, R. F., and Coauthors, 2003: The version-2 global precipitation climatology project (gpcp) monthly precipitation analysis (1979–present). *Journal of hydrometeorology*, **4 (6)**, 1147–1167.

Alexeev, V. A., and C. H. Jackson, 2013: Polar amplification: is atmospheric heat transport important? *Climate dynamics*, **41**, 533–547.

Armour, K. C., N. Siler, A. Donohoe, and G. H. Roe, 2019: Meridional atmospheric heat transport constrained by energetics and mediated by large-scale diffusion. *Journal of Climate*, **32 (12)**, 3655–3680.

Baggett, C., and S. Lee, 2017: An identification of the mechanisms that lead to arctic warming during planetary-scale and synoptic-scale wave life cycles. *Journal of the Atmospheric Sciences*, **74 (6)**, 1859–1877.

Barnes, E. A., and D. L. Hartmann, 2012: The global distribution of atmospheric eddy length scales. *Journal of climate*, **25 (9)**, 3409–3416.

Barsugli, J. J., and D. S. Battisti, 1998: The basic effects of atmosphere–ocean thermal coupling on midlatitude variability. *Journal of the Atmospheric Sciences*, **55 (4)**, 477–493.

Bonan, D., K. Armour, G. Roe, N. Siler, and N. Feldl, 2018: Sources of uncertainty in the meridional pattern of climate change. *Geophysical Research Letters*, **45 (17)**, 9131–9140.

Branstator, G., 1995: Organization of storm track anomalies by recurring low-frequency circulation anomalies. *Journal of the atmospheric sciences*, **52 (2)**, 207–226.

Brayshaw, D. J., B. Hoskins, and M. Blackburn, 2009: The basic ingredients of the north atlantic storm track. part i: Land–sea contrast and orography. *Journal of the Atmospheric Sciences*, **66 (9)**, 2539–2558.

Bretherton, C. S., M. Widmann, V. P. Dymnikov, J. M. Wallace, and I. Bladé, 1999: The effective number of spatial degrees of freedom of a time-varying field. *Journal of climate*, **12 (7)**, 1990–2009.

Broccoli, A. J., and S. Manabe, 1992: The effects of orography on midlatitude northern hemisphere dry climates. *Journal of Climate*, **5 (11)**, 1181–1201.

Burls, N. J., R. C. Blamey, B. A. Cash, E. T. Swenson, A. a. Fahad, M.-J. M. Bopape, D. M. Straus, and C. J. Reason, 2019: The cape town "day zero" drought and hadley cell expansion. *Npj Climate and Atmospheric Science*, **2 (1)**, 27.

Cardinale, C. J., and B. E. Rose, 2022: The arctic surface heating efficiency of tropospheric energy flux events. *Journal of Climate*, 1–39.

Cardinale, C. J., B. E. Rose, A. L. Lang, and A. Donohoe, 2021: Stratospheric and tropospheric flux contributions to the polar cap energy budgets. *Journal of Climate*, **34 (11)**, 4261–4278.

Cash, B. A., P. J. Kushner, and G. K. Vallis, 2005: Zonal asymmetries, teleconnections, and annular patterns in a gcm. *Journal of the atmospheric sciences*, **62 (1)**, 207–219.

Chang, E. K., S. Lee, and K. L. Swanson, 2002: Storm track dynamics. *Journal of climate*, **15 (16)**, 2163–2183.

Chaudhuri, A. H., R. M. Ponte, G. Forget, and P. Heimbach, 2013: A comparison of atmospheric reanalysis surface products over the ocean and implications for uncertainties in air–sea boundary forcing. *Journal of Climate*, **26 (1)**, 153–170.

Chemke, R., Y. Ming, and J. Yuval, 2022: The intensification of winter mid-latitude storm tracks in the southern hemisphere. *Nature climate change*, **12 (6)**, 553–557.

Chemke, R., and L. M. Polvani, 2019: Opposite tropical circulation trends in climate models and in reanalyses. *Nature Geoscience*, **12 (7)**, 528–532.

Chemke, R., and L. M. Polvani, 2020: Linking midlatitudes eddy heat flux trends and polar amplification. *npj Climate and Atmospheric Science*, **3 (1)**, 8.

Chung, E.-S., and Coauthors, 2022: Antarctic sea-ice expansion and southern ocean cooling linked to tropical variability. *Nature Climate Change*, **12 (5)**, 461–468.

Chylek, P., C. Folland, J. D. Klett, M. Wang, N. Hengartner, G. Lesins, and M. K. Dubey, 2022: Annual mean arctic amplification 1970–2020: observed and simulated by cmip6 climate models. *Geophysical Research Letters*, **49 (13)**, e2022GL099 371.

Cook, K. H., and I. M. Held, 1988: Stationary waves of the ice age climate. *Journal of climate*, **1 (8)**, 807–819.

Cox, T., K. C. Armour, G. H. Roe, A. Donohoe, and D. M. Frierson, 2021: Radiative and dynamic controls on atmospheric heat transport over different planetary rotation rates. *Journal of Climate*, **34 (9)**, 3543–3554.

Cox, T., A. Donohoe, G. H. Roe, K. C. Armour, and D. M. Frierson, 2022: Near invariance of poleward atmospheric heat transport in response to midlatitude orography. *Journal of Climate*, **35 (13)**, 4099–4113.

Dawson, A., 2016: Windspharm: A high-level library for global wind field computations using spherical harmonics. *Journal of Open Research Software*, **4 (1)**.

Dong, Y., and Coauthors, 2021: Biased estimates of equilibrium climate sensitivity and transient climate response derived from historical cmip6 simulations. *Geophysical Research Letters*, **48 (24)**, e2021GL095 778.

Donohoe, A., K. C. Armour, G. H. Roe, D. S. Battisti, and L. Hahn, 2020: The partitioning of meridional heat transport from the last glacial maximum to co2 quadrupling in coupled climate models. *Journal of Climate*, **33 (10)**, 4141–4165.

Donohoe, A., and D. S. Battisti, 2012: What determines meridional heat transport in climate models? *Journal of Climate*, **25 (11)**, 3832–3850.

Donohoe, A., D. M. Frierson, and D. S. Battisti, 2014: The effect of ocean mixed layer depth on climate in slab ocean aquaplanet experiments. *Climate dynamics*, **43 (3-4)**, 1041–1055.

Doyle, J., G. Lesins, C. Thackray, C. Perro, G. Nott, T. Duck, R. Damoah, and J. Drummond, 2011: Water vapor intrusions into the high arctic during winter. *Geophysical research letters*, **38 (12)**.

Eyring, V., S. Bony, G. A. Meehl, C. A. Senior, B. Stevens, R. J. Stouffer, and K. E. Taylor, 2016: Overview of the coupled model intercomparison project phase 6 (cmip6) experimental design and organization. *Geoscientific Model Development*, **9 (5)**, 1937–1958.

Farneti, R., and G. K. Vallis, 2013: Meridional energy transport in the coupled atmosphere–ocean system: Compensation and partitioning. *Journal of climate*, **26 (18)**, 7151–7166.

Flannery, B. P., 1984: Energy balance models incorporating transport of thermal and latent energy. *Journal of Atmospheric Sciences*, **41 (3)**, 414–421.

Frierson, D. M., 2007: The dynamics of idealized convection schemes and their effect on the zonally averaged tropical circulation. *Journal of the atmospheric sciences*, **64 (6)**, 1959–1976.

Frierson, D. M., I. M. Held, and P. Zurita-Gotor, 2006: A gray-radiation aquaplanet moist gcm. part i: Static stability and eddy scale. *Journal of the atmospheric sciences*, **63 (10)**, 2548–2566.

Gelaro, R., and Coauthors, 2017: The modern-era retrospective analysis for research and applications, version 2 (merra-2). *Journal of climate*, **30 (14)**, 5419–5454.

GFDL Global Atmospheric Model Development Team, 2004: The new gfdl global atmosphere and land model am2–lm2: Evaluation with prescribed sst simulations. *Journal of Climate*, **17 (24)**, 4641–4673.

Grytsai, A., O. Evtushevsky, O. Agapitov, A. Klekociuk, and G. Milinevsky, 2007: Structure and long-term change in the zonal asymmetry in antarctic total ozone during spring. *Annales Geophysicae*, Copernicus Publications Göttingen, Germany, Vol. 25, 361–374.

Gu, G., R. F. Adler, and G. J. Huffman, 2016: Long-term changes/trends in surface temperature and precipitation during the satellite era (1979–2012). *Climate Dynamics*, **46**, 1091–1105.

Hahn, L. C., K. C. Armour, D. S. Battisti, I. Eisenman, and C. M. Bitz, 2022: Seasonality in arctic warming driven by sea ice effective heat capacity. *Journal of Climate*, **35 (5)**, 1629–1642.

Hahn, L. C., K. C. Armour, M. D. Zelinka, C. M. Bitz, and A. Donohoe, 2021: Contributions to polar amplification in cmip5 and cmip6 models. *Frontiers in Earth Science*, **9**, 710 036.

Held, I. M., 1999: The macroturbulence of the troposphere. *Tellus A*, **51 (1)**, 59–70.

Held, I. M., and B. J. Soden, 2006: Robust responses of the hydrological cycle to global warming. *Journal of climate*, **19 (21)**, 5686–5699.

Held, I. M., M. Ting, and H. Wang, 2002: Northern winter stationary waves: Theory and modeling. *Journal of climate*, **15 (16)**, 2125–2144.

Hersbach, H., and Coauthors, 2018a: Era5 hourly data on single levels from 1979 to present, copernicus climate change service (c3s) climate data store (cds). *ECMWF*, **147**, 5–6.

Hersbach, H., and Coauthors, 2018b: Era5 hourly data on single levels from 1979 to present. copernicus climate change service (c3s) climate data store (cds). ECMWF, doi: 10.24381/cds.adbb2d47.

Hersbach, H., and Coauthors, 2020: The era5 global reanalysis. *Quarterly Journal of the Royal Meteorological Society*, **146 (730)**, 1999–2049.

Holton, J. R., 1973: An introduction to dynamic meteorology. *American Journal of Physics*, **41 (5)**, 752–754.

Holton, J. R., and G. J. Hakim, 2013: *An Introduction to Dynamic Meteorology*, Vol. 88. Academic Press.

Hoskins, B. J., and D. J. Karoly, 1981: The steady linear response of a spherical atmosphere to thermal and orographic forcing. *Journal of Atmospheric Sciences*, **38 (6)**, 1179–1196.

Hoskins, B. J., and P. J. Valdes, 1990: On the existence of storm-tracks. *Journal of the Atmospheric Sciences*, **47 (15)**, 1854–1864.

Hu, Y., H. Huang, and C. Zhou, 2018: Widening and weakening of the hadley circulation under global warming. *Science Bulletin*, **63 (10)**, 640–644.

Huang, B., and Coauthors, 2017: Noaa extended reconstructed sea surface temperature (ersst), version 5. *NOAA National Centers for Environmental Information*, **30 (8179-8205)**, 25.

Hwang, Y.-T., D. M. Frierson, and J. E. Kay, 2011: Coupling between arctic feedbacks and changes in poleward energy transport. *Geophysical Research Letters*, **38 (17)**.

Inatsu, M., H. Mukougawa, and S.-P. Xie, 2002: Stationary eddy response to surface boundary forcing: Idealized gcm experiments. *Journal of the atmospheric sciences*, **59 (11)**, 1898–1915.

Inatsu, M., H. Mukougawa, and S.-P. Xie, 2003: Atmospheric response to zonal variations in midlatitude sst: Transient and stationary eddies and their feedback. *Journal of climate*, **16 (20)**, 3314–3329.

Ivanciu, I., K. Matthes, S. Wahl, J. Harlaß, and A. Biastoch, 2021: Effects of prescribed cmip6 ozone on simulating the southern hemisphere atmospheric circulation response to ozone depletion. *Atmospheric Chemistry and Physics*, **21 (8)**, 5777–5806.

Kapsch, M.-L., R. G. Graversen, and M. Tjernström, 2013: Springtime atmospheric energy transport and the control of arctic summer sea-ice extent. *Nature Climate Change*, **3 (8)**, 744–748.

Kaspi, Y., and T. Schneider, 2013: The role of stationary eddies in shaping midlatitude storm tracks. *Journal of the atmospheric sciences*, **70 (8)**, 2596–2613.

Kiehl, J., 1994: On the observed near cancellation between longwave and shortwave cloud forcing in tropical regions. *Journal of Climate*, 559–565.

Kobayashi, S., and Coauthors, 2015: The jra-55 reanalysis: General specifications and basic characteristics. *Journal of the Meteorological Society of Japan. Ser. II*, **93 (1)**, 5–48.

Laliberté, F., and P. J. Kushner, 2014: Midlatitude moisture contribution to recent arctic tropospheric summertime variability. *Journal of climate*, **27 (15)**, 5693–5707.

Lembo, V., G. Messori, R. Graversen, and V. Lucarini, 2019: Spectral decomposition and extremes of atmospheric meridional energy transport in the northern hemisphere midlatitudes. *Geophysical Research Letters*, **46 (13)**, 7602–7613.

Li, C., and D. S. Battisti, 2008: Reduced atlantic storminess during last glacial maximum: Evidence from a coupled climate model. *Journal of Climate*, **21 (14)**, 3561–3579.

Liang, M., A. Czaja, R. Graversen, and R. Tailleux, 2018: Poleward energy transport: is the standard definition physically relevant at all time scales? *Climate dynamics*, **50 (5)**, 1785–1797.

Liu, C., and E. A. Barnes, 2015: Extreme moisture transport into the arctic linked to rossby wave breaking. *Journal of Geophysical Research: Atmospheres*, **120 (9)**, 3774–3788.

Liu, H., Z. Song, X. Wang, and V. Misra, 2022: An ocean perspective on cmip6 climate model evaluations. Elsevier, 105120 pp.

Liu, X., D. S. Battisti, and G. H. Roe, 2017: The effect of cloud cover on the meridional heat transport: Lessons from variable rotation experiments. *Journal of Climate*, **30 (18)**, 7465–7479.

Lorenz, E., 1953: A multiple index notation for describing atmospheric transport processes. *AFCRL Report*, 35–53.

Manabe, S., and T. B. Terpstra, 1974: The effects of mountains on the general circulation of the atmosphere as identified by numerical experiments. *Journal of Atmospheric Sciences*, **31 (1)**, 3–42.

Marshall, J., A. Donohoe, D. Ferreira, and D. McGee, 2014: The ocean's role in setting the mean position of the inter-tropical convergence zone. *Climate Dynamics*, **42**, 1967–1979.

Mayer, J., M. Mayer, and L. Haimberger, 2021: Consistency and homogeneity of atmospheric energy, moisture, and mass budgets in era5. *Journal of Climate*, **34 (10)**, 3955–3974.

Merlis, T. M., and M. Henry, 2018: Simple estimates of polar amplification in moist diffusive energy balance models. *Journal of Climate*, **31 (15)**, 5811–5824.

Messori, G., and A. Czaja, 2013: On the sporadic nature of meridional heat transport by transient eddies. *Quarterly Journal of the Royal Meteorological Society*, **139 (673)**, 999–1008.

Messori, G., and A. Czaja, 2014: Some considerations on the spectral features of meridional heat transport by transient eddies. *Quarterly Journal of the Royal Meteorological Society*, **140 (681)**, 1377–1386.

Messori, G., and A. Czaja, 2015: On local and zonal pulses of atmospheric heat transport in reanalysis data. *Quarterly Journal of the Royal Meteorological Society*, **141 (691)**, 2376–2389.

Messori, G., R. Geen, and A. Czaja, 2017: On the spatial and temporal variability of atmospheric heat transport in a hierarchy of models. *Journal of the Atmospheric Sciences*, **74 (7)**, 2163–2189.

Messori, G., C. Woods, and R. Caballero, 2018: On the drivers of wintertime temperature extremes in the high arctic. *Journal of Climate*, **31 (4)**, 1597–1618.

Mortin, J., G. Svensson, R. G. Graversen, M.-L. Kapsch, J. C. Stroeve, and L. N. Boisvert, 2016: Melt onset over arctic sea ice controlled by atmospheric moisture transport. *Geophysical Research Letters*, **43 (12)**, 6636–6642.

NASA/LARC/SD/ASDC, 2019: Ceres energy balanced and filled (ebaf) toa and surface monthly means data in netcdf edition 4.1.

Park, M., and S. Lee, 2019: Relationship between tropical and extratropical diabatic heating and their impact on stationary–transient wave interference. *Journal of the Atmospheric Sciences*, **76 (9)**, 2617–2633.

Park, M., and S. Lee, 2022: On the causes of synoptic-scale eddy heat flux decline. *Geophysical Research Letters*, **49 (24)**, e2022GL100 963.

Pierrehumbert, R. T., 2010: *Principles of planetary climate*. Cambridge University Press.

Ramaswamy, V., M. Schwarzkopf, and W. Randel, 1996: Fingerprint of ozone depletion in the spatial and temporal pattern of recent lower-stratospheric cooling. *Nature*, **382**, 616–618.

Ramsey, J. B., H. J. Newton, and J. L. Harvill, 2002: *The elements of statistics: With applications to economics and the social sciences*. Duxbury/Thomson Learning.

Randel, W. J., and F. Wu, 1999: Cooling of the arctic and antarctic polar stratospheres due to ozone depletion. *Journal of Climate*, **12 (5)**, 1467–1479.

Ringler, T. D., and K. H. Cook, 1997: Factors controlling nonlinearity in mechanically forced stationary waves over orography. *Journal of the atmospheric sciences*, **54 (22)**, 2612–2629.

Rodgers, K. B., and Coauthors, 2021: Ubiquity of human-induced changes in climate variability. *Earth System Dynamics*, **12 (4)**, 1393–1411.

Rodwell, M. J., and B. J. Hoskins, 1996: Monsoons and the dynamics of deserts. *Quarterly Journal of the Royal Meteorological Society*, **122 (534)**, 1385–1404.

Rodwell, M. J., and B. J. Hoskins, 2001: Subtropical anticyclones and summer monsoons. *Journal of Climate*, **14 (15)**, 3192–3211.

Roe, G. H., N. Feldl, K. C. Armour, Y.-T. Hwang, and D. M. Frierson, 2015: The remote impacts of climate feedbacks on regional climate predictability. *Nature Geoscience*, **8 (2)**, 135–139.

Salustri, G., and P. H. Stone, 1983: A diagnostic study of the forcing of the ferrel cell by eddies, with latent heat effects included. *Journal of the atmospheric sciences*, **40 (5)**, 1101–1109.

Sasamori, T., and J. W. Melgarejo, 1978: A parameterization of large-scale heat transport in mid-latitudes. part i. transient eddies. *Tellus*, **30 (4)**, 289–299.

Siler, N., G. H. Roe, and K. C. Armour, 2018: Insights into the zonal-mean response of the hydrologic cycle to global warming from a diffusive energy balance model. *Journal of Climate*, **31 (18)**, 7481–7493.

Stone, P. H., 1978: Constraints on dynamical transports of energy on a spherical planet. *Dynamics of atmospheres and oceans*, **2 (2)**, 123–139.

Takahashi, K., and D. S. Battisti, 2007a: Processes controlling the mean tropical pacific precipitation pattern. part i: The andes and the eastern pacific itcz. *Journal of Climate*, **20 (14)**, 3434–3451.

Takahashi, K., and D. S. Battisti, 2007b: Processes controlling the mean tropical pacific precipitation pattern. part ii: The spcz and the southeast pacific dry zone. *Journal of Climate*, **20 (23)**, 5696–5706.

Thode, H. C., 2002: *Testing for normality*. CRC press.

Thompson, D. W., and S. Solomon, 2002: Interpretation of recent southern hemisphere climate change. *Science*, **296 (5569)**, 895–899.

Trenberth, K. E., and S.-C. Chen, 1988: Planetary waves kinematically forced by himalayan orography. *Journal of the atmospheric sciences*, **45 (20)**, 2934–2948.

Trenberth, K. E., J. T. Fasullo, and J. Kiehl, 2009: Earth's global energy budget. *Bulletin of the American Meteorological Society*, **90 (3)**, 311–324.

Trenberth, K. E., and D. P. Stepaniak, 2003a: Co-variability of components of poleward atmospheric energy transports on seasonal and interannual timescales. *Journal of Climate*, **16**, 3691–3705.

Trenberth, K. E., and D. P. Stepaniak, 2003b: Seamless poleward atmospheric energy transports and implications for the hadley circulation. *Journal of Climate*, **16 (22)**, 3706–3722.

Valdes, P. J., and B. J. Hoskins, 1991: Nonlinear orographically forced planetary waves. *Journal of Atmospheric Sciences*, **48 (18)**, 2089–2106.

Walker, C. C., and T. Schneider, 2006: Eddy influences on hadley circulations: Simulations with an idealized gcm. *Journal of the atmospheric sciences*, **63 (12)**, 3333–3350.

White, R. H., J. M. Wallace, and D. Battisti, 2021: Revisiting the role of mountains in the northern hemisphere winter atmospheric circulation. *Journal of the Atmospheric Sciences*, **78 (7)**, 2221–2235.

Wild, M., D. Folini, C. Schär, N. Loeb, E. G. Dutton, and G. König-Langlo, 2013: The global energy balance from a surface perspective. *Climate dynamics*, **40**, 3107–3134.

Wild, M., and Coauthors, 2015: The energy balance over land and oceans: an assessment based on direct observations and cmip5 climate models. *Climate Dynamics*, **44**, 3393–3429.

Wills, R. C., Y. Dong, C. Proistosecu, K. C. Armour, and D. S. Battisti, 2022: Systematic climate model biases in the large-scale patterns of recent sea-surface temperature and sea-level pressure change. *Geophysical Research Letters*, **49 (17)**, e2022GL100 011.

Wills, R. C., and T. Schneider, 2016: How stationary eddies shape changes in the hydrological cycle: Zonally asymmetric experiments in an idealized gcm. *Journal of Climate*, **29 (9)**, 3161–3179.

Woods, C., and R. Caballero, 2016: The role of moist intrusions in winter arctic warming and sea ice decline. *Journal of Climate*, **29 (12)**, 4473–4485.

Woods, C., R. Caballero, and G. Svensson, 2013: Large-scale circulation associated with moisture intrusions into the arctic during winter. *Geophysical Research Letters*, **40 (17)**, 4717–4721.

Zaplotnik, Ž., M. Pikovnik, and L. Boljka, 2022: Recent hadley circulation strengthening: a trend or multidecadal variability? *Journal of Climate*, **35 (13)**, 4157–4176.